The Pennsylvania State University

The Graduate School

Department of Geosciences

NUMERICAL MODELS OF THE DYNAMICS OF LITHOSPHERIC DEFORMATION AT COMPLEX PLATE BOUNDARIES

A Thesis in

Geosciences

by

Rocco Malservisi

Submitted in Partial Fulfillment
of the Requirements
for the Degree of

Doctor of Philosophy

December 2002

Abstract

Plate boundaries are the sites where deformation induced by the relative motion of lithospheric blocks occurs. Observation of surface deformation, relative velocity of regions of the crust, and seismicity, all provide information on this process. In this thesis, I study lithospheric deformation at several complex plate boundaries. Lithospheric rheology and the earthquake cycle can have large effects on the observed surface velocity field. The Eastern California Shear Zone, an area likely characterized by a contrast in viscosity in the lower crust/upper mantle, provides a plate boundary segment to analyze those effects. I find that the contrast in the rheology of the lower layers (lower crust/upper mantle) can induce an asymmetric strain accumulation. This opens up the possibility of asymmetric coseismic displacement during an earthquake. Strike-slip creeping faults and their interaction with the surrounding lithosphere affect the patterns of strain accumulation and earthquake potential. In particular, I analyze the effect of fault geometry and of locked patches of the fault on the surface creep rate, and the possibility to apply observed patterns of micro-seismicity as a further constraint to map the distribution of fault creep. This allows me to further assess the seismic risk on the Hayward Fault. The main result of this aspect of the thesis, is that the interaction of the creeping fault with the surrounding lithosphere creates a smooth transition from locked patches to regions free to creep. This reduces the creep rate in the regions surrounding locked patches with “creepable” areas that in reality creep very slowly. I find that the transition creates regions of higher stress that may generate the micro-seismicity. Comparing the results of my model with the micro-seismicity, the non-recurrent earthquakes mainly cluster in the transition zones while the repeating earthquakes occur

principally in the fully creeping areas. Another aspect of plate boundary deformation analyzed in this thesis is the accommodation of the transpressional regime in the region of Fiordland, South Island, New Zealand. That region is characterized by high elevation and high positive gravity anomalies, suggesting that the elevation is not in isostatic equilibrium and needs a dynamic support. I find that the bending of the Australian plate, which is subducting beneath Fiordland, can provide that needed support. Furthermore, I find that in order to provide the correct dynamic support it is necessary to mechanically decouple the subducting sliver of Australian plate from the main plate. This suggest the presence of a tear or a weak zone within the Australian plate.

Table of Contents

List of Figures

List of Tables

Preface

All of the chapters in this thesis have been submitted to or published in scientific journals. In all these works, Malservisi was the main researcher but other scientists collaborated with discussions and exchanges of ideas and data. Chapter 2 reports research results from a collaborative project between the Pennsylvania State University and of the University of Miami (PIs K.P. Furlong and T.H. Dixon). Chapters 3 and 4 are the continuation and expansion of work initiated as the undergraduate senior thesis of Christine Gans. Malservisi served as co-advisor on that project and extended the work significantly in the chapters presented here. Chapter 5 results from a collaborative project between the Pennsylvania State University and the Ministry of Research and Science and Technology of New Zealand (PIs K.P. Furlong and H. Anderson).

Many of the figures of this thesis have been made using Generic Mapping Tools [Wessel, P., W.H.F. Smith, New version of the Generic Mapping Tools released, *EOS Trans. Amer. Geophys. U.*, 76,329, 1995].

The researches of Malservisi has been supported by the following NSF grants awarded to K.P. Furlong:
NSF-EAR 97-25187: Lithospheric Tectonics of a Transpressional Plate Boundary, Fiordland, New Zealand;
NSF-EAR 99-2937: Tectonically Driven Landform Response to the Mendocino Crustal Conveyor, Northern Coast Range, California;
NSF-EAR 00-3740: Geodynamics of the Eastern California Shear Zone.

Acknowledgements

At the end of my study at Penn State I need to thank those who made possible and pleasant this experience. Kevin Furlong (my current advisor), Roberto Sabadini (Università di Milano, Italy), and Rob Govers (Utrecht University, The Netherlands) organized my application to this school. Giorgio Spada (Università di Urbino) and Clemente Pallotti (Università di Bologna) played an important role in convincing me of the importance to accept this offer.

The smooth transition from my Italian University to Penn State and the lack of "cultural shock" is mainly due to the help and friendship of students and staff in the Department of Geosciences. In particular, I appreciated the help of the housemates and officemates of my first year: Dan Pope, Brandon Dugan, Mike Brandon and Todd Dupont, and among the staff of the department, Anne Cavanaugh Stover and Linda Altamura.

A particular thanks to the swimmers, coaches and parents at Penn State Aquatics (Big Cat and NLAC), in particular to Jon Larson. Giving me the possibility to coach the age-group, they gave me a necessary distraction from the student life, good times, and the possibility to keep a link with a sport I love, swimming.

I have particular gratitude to the Research West crew. Chris Guzofski, Jane Lock, and Jaime Whitlock. They provide a very nice working environment, good discussions, and encouraging comments. Chris especially, helped me to overcome one of the most critical times during my studies.

The research presented in this thesis have been enhanced by discussions with many different people. In particular, I want to thanks all the coauthors of the different papers: Tim Dixon, Helen Anderson, Christine Gans, and Kevin Furlong.

I have to thank Rob Govers not only for the connection between my former and current advisors but also because he introduced me to the world of TECTON and to the finite element modeling. Thanks also to the Tectonophysics Group of the Faculty of Earth Science at the University of Utrecht, who always offered me hospitality, discussion time and good suggestions the many times I traveled to The Netherlands to work with Rob.

I have also to thank all my thesis committee, Chuck Ammon, Renata Engel, Don Fisher, and Andy Nyblade for the invaluable suggestions and help not only during the formal meeting but also throughout all my study at Penn State.

To finish I want to thank my advisor Kevin Furlong for his guidance, support and encouragement throughout the entire experience of my doctoral study.

“*The men of experiment are like the ant, they only collect and use; the reasoners resemble spiders, who make cobwebs out of their own substance. But the bee takes a middle course: it gathers its material from the flowers of the garden and of the field, but transforms and digests it by a power of its own. Not unlike this is the true business of philosophy; for it neither relies solely or chiefly on the powers of the mind, nor does it take the matter which it gathers from natural history and mechanical experiments and lay it up in the memory whole, as it finds it, but lays it up in the understanding altered and digested.*”

F. Bacon Novum Organum, Aphorism XCV, 1652.

CHAPTER 1

INTRODUCTION

In 1953, Sir E. Hillary and N. Tenzing reached the peak of Mount Everest, the highest mountain on the earth. A few years later, in 1960, J. Piccard and D. Walsh descended down to Deep Challenger, the deepest point in the oceans. At about the same time, a series of articles [Hess, 1962; Irving, 1956; Wilson, 1965; Vine and Matthews, 1963; McKenzie and Parker, 1967; Isacks et al, 1968; Morgan, 1968] presented a new view of geologic processes. A theory that could explain the depths reached by Piccard and Walsh and the heights reached by Hillary and Tenzing. The theory is called plate tectonics.

The main postulate of plate tectonics was that the outer layer of our planet is a rigid shell called "lithosphere". This rigid layer is broken into different blocks, the "plates", which are in relative motion. These plates were initially thought to be internally rigid and it was supposed that they could transmit stresses for long distances, meaning that nearly all deformation occurs in a narrow region at the boundaries. Three types of boundaries are defined in plate tectonics: divergent boundaries, where new lithosphere is created (ocean ridges); transform faults, where two plates are sliding past one another; and convergent margins, where the lithosphere is consumed by sinking into the mantle (subduction) or is thickened in mountain belt. Convergent margins are responsible for the features explored by Hillary, Tenzing, Piccard, and Walsh.

As the theory of plate tectonics has developed, scientists have recognized that plate boundaries are more complex than initially thought and that the deformation, rather than restricted to a narrow zone, can be accommodated by a network of structures over large regions [e.g. Molnar and Tapponnier, 1981]. This complexity can appear in many different forms: mountain chains far away from collision zone (e.g. Tien Shan); fragmentation of plates and diffuse deformation (e.g. the Mediterranean Sea); broad regions accommodating deformation (e.g. Western US); and different mechanisms accommodating a similar plate kinematics including the reversal of subduction polarity along a boundary (e.g. New Zealand).

Understanding the mechanisms and the physical processes driving deformation along such margins is key to reconciling the dynamics of plate boundaries and the origin of their complexity. Although the partial differential equations dealing with the physical processes at plate boundaries are relatively simple, material properties, geometrical complexities, heterogeneity and realistic boundary conditions, do not always allow analytical solutions. For this reason, in order to make quantitative statements on Earth processes, we often need to employ numerical techniques. In this thesis, I use finite element modeling (FEM) as a tool to investigate the behavior of plate boundaries and the influence of plate boundary characteristics such as geometry, rheology, and the earthquake cycle on the dynamics of complex plate boundaries. Of the available numerical techniques, FEM have the specific advantage of being flexible in allowing high resolution discretization where required and coarser discretization away from the region of interest. Finite elements techniques are well founded in mathematical literature. Throughout the entire thesis, I used the FEM code TECTON [Melosh and Raefsky, 1980]. TECTON is a finite element code specifically developed to solve tectonic problems. The code is different from many other FEM packages used in geologic studies since it also incorporates elasticity in the solution of the Stokes equations using a Lagrangian approach. The code allows us to easily simulate the presence of faults, both creeping and locked [Mellosh and Williams, 1989; Mellosh and Raefsky, 1981] and to implement time dependent rheologies. It has been developed over many years by different authors and in this thesis, I use the 3-D version developed by Govers [1993; Govers et al 2000; Govers and Meijer, 2001].

In this thesis, I focus on two plate boundaries, the North America/Pacific plate boundary (the Eastern California Shear Zone and the Hayward Fault) and the Pacific/Australia plate boundary through South Island, New Zealand. The North America/Pacific plate boundary is a complex boundary with relative motion distributed across a broad zone. Although the majority of the deformation occurs near and along the San Andreas fault system [e.g. Prescott et al., 2001], almost 20% of the relative plate motion is accommodated along the Walker Lane – Eastern California Shear Zone fault system [Dokka and Travis, 1990; Sauber et al., 1994; Savage et al., 1990; Dixon et al. 1995, 2000; Gan et al., 2000; Miller et al., 2001; Malservisi et al. 2001]. Any remaining fraction of plate boundary displacement appears to be accommodated within the broad area of the Basin and Range [Thatcher et al., 1999; Wernicke et al., 2000].

In chapter 2, I analyze the roles that the earthquake cycle and lithospheric rheology play in the dynamics of the Eastern California Shear Zone. Geodetic and kinematic data are a principal tool often used to constrain the regional dynamics. The results depend on the hypothesis used when modeling the data. In this chapter I address the role that rheologies, in particular lateral changes in viscosity, play in kinematic observations and the effects of inclusion of the earthquake cycle in this modeling.

Even within the San Andreas Fault system, considered the “main” plate boundary, similar kinematic regimes are accommodated in different ways: some areas of the fault are locked and generate large earthquakes [e.g. 1906 San Francisco earthquake, 1989 Loma Prieta, or the Parkfield region), while some sections constantly creep (e.g. sections of the Hayward Fault [Lienkaemper et al., 1991], Calaveras Fault [Evans et al. 1981], and the San Andreas fault in central California [e.g. Burford and Hars, 1980]). Chapters 3, and 4 focus on aspects of the rheology of the San Andreas fault system and the causes and consequences of locked and creeping fault segments.

In chapter 3 I analyze the dynamics of a creeping faults. In particular, I investigate the effects of fault zone geometries and physical characteristics such as frictionless or locked patches on the observed surface creep rate. The model is driven by far-field plate motion, incorporating a linear vicsoelastic rheology to study the effect of the surrounding lithosphere on the fault creep.

An application of the modeling results of chapter 3 to the specific earthquake hazard issues for the Hayward fault is the focus of chapter 4. Here, I compare the results from chapter 3 with the micro-seismicity associated with creeping faults to refine the model of creep on the Hayward fault. The results are used to evaluate the seismic risk in the San Francisco Bay area.

Unlike the western US, deformation along the Pacific-Australian plate boundary through New Zealand is accommodated in a relatively narrow zone. However, this plate boundary is far from simple. Although the plate boundary kinematics do not significantly change along the boundary, deformation is accommodated by quite different mechanisms in different places. In North Island, the convergence between the two plates results in subduction of the Pacific plate beneath the Australian plate. South Island is characterized by a transcurrent plate boundary where the Australian plate slides past the Pacific. A mismatch between the direction of translation and the orientation of the plate boundary generates a component of compression that produces a kinematic regime commonly termed “transpressional”. In the central part of South Island, the compressional component of the relative plate motion is accommodated through thickening of the lithosphere and the creation of the Southern Alps [e.g. Stern et al., 2000; Molnar et al., 1999; Shi and Allis, 1995]. In spite of virtually identical kinematics to those in the central part of the South Island, the southwest corner of the South Island, Fiordland, reacts in a completely different way. This region produces a geophysical signature that is remarkably different from the Southern Alps. Rather than lithospheric thickening and the development of isostatically compensated mountains, deep earthquakes and plate reconstructions indicate that the convergence causes a corner of Australian plate to bend and subduct beneath the Pacific plate [Sutherland, 1995; Sutherland and Melhuish, 2000; Reyners et al., 2001]. Furthermore, the significantly different gravity signature of this region implies that the high elevation of Fiordland is not in isostatic equilibrium as is the case for the Southern Alps but rather requires a dynamic support.

In Chapter 5, I investigate the Australian/Pacific plate boundary in the region of Fiordland. In particular, I explore the possibility that the subduction and the bending of the Australian plate can provide the required support for the local topography. The results of the modeling indicate that to fit the observed local plate geometry there is a need to include a weak area in the lithosphere that mechanically decouples the subducting sliver of the Australian plate from the main plate. Additionally the modeling results allow us to speculate about the linkage between the lithospheric root developing beneath the Southern Alps and the inception of the subduction beneath Fiordland.

I also include an appendix that compares the results of numerical modeling with analytical solution for the case of the fault-parallel surface velocity and an appendix that analyze the effect of the boundary conditions on the modeling results of chapter 3.

REFERENCES

Burford, R.O., P.W. Harsh, Slip on the San Andreas fault in Central California from alinement array survey, *Bull. Seismol. Soc. Am.*, 70, 1233-1261, 1980.

Dixon, T.H., S. Robaudo, J. Lee and M.C. Reheis, Constraints on present-day Basin and Range deformation from space geodesy, *Tectonics*, 14(4), 755-772, 1995.

Dixon, T.H., M. Miller, F. Farina, H. Wang and D. Johnson, Present-day motion of the Sierra Nevada block and some tectonic implications for the Basin and Range Province, North America Cordillera, *Tectonics*, 19(1), 1-24, 2000.

Dokka, R.K., Travis, C.J., Role of the Eastern California Shear Zone in accomodating Pacific-North America plate motion, *Geophys. Res. Lett.*, 17(9), 1323-1326, 1990.

Evans, K.F., R.O. Burford, G.C.P. King, Propagating episodic creep and aseismic slip behavior of the Calveras fault north of Hollister, California, *J. Geophys. Res.*, 86, 3721-3725, 1981.

Gan, W., J.L. Svarc, J.C. Savage and W.H. Prescott, Strain accumulation across the Eastern California Shear Zone at latitude 36 30'N, *J. Geophys. Res.*, 105, 16229-16236, 2000.

Govers, R., Dynamics of Lithospheric Extension: A Modeling Study. Ph.D. Thesis, University of Utrecht, *Geologica Ultraiectina* 105, 1-240, 1993.

Govers R., M.J.R. Wortel, S.J.H. Buiter, Surface expression of slab breack-off, results from 3D numerical models, *Geophysical Research Abstract*, EGS 25th general assembly, Nice, France, 2000,

Govers R., P.T. Meijer, On the dynamics of the Juan de Fuca Plate, *Earth and Plan. Scie. Lett.,* **189**, 115-131, 2001.

Hess, H.H., History of ocean basins, in Petrological Studies: A volume in honor of A.F. Buddington, ed by A.E.J. Engel, H.L. James, and B.F. Leonard, 599-620, Geological Society of America, 1962.

Irving, E., Paleomagnetic and paleoclimatological aspects of polar wandering, *Pure Appl. Geophys.*, 33, 23-41, 1956.

Isack, B., J. Oliver, L.R. Sykes, Seismology and the new global tectonics, *J. Geophys. Res.*, 73, 5855-5899, 1968.

Lienkaemper, J.J., G. Borchardt, M. Lisowski, Historic creep rate and potential for seismic slip along the Hayward fault, California, *J. Geophys. Res.*, 96, 18261-18283, 1991.

Malservisi, R., K.P. Furlong, T.H. Dixon, Influence of the earthquake cycle and lithospheric rheology on the dynamics of the Eastern California Shear Zone, *Geophys. Res. Lett.*, 28, 2731-2734, 2001.

Melosh, H. J., and A. Raefsky, The dynamical origin of subduction zone topography, *Geophys. J. R. Soc.* 60, 333-354, 1980.

Melosh, H. J., and A. Raefsky, A simple and efficient method for introducing faults into finite element computations, *Bull. Seismol. Soc. Am.*, 71(5), 1391-1400, 1981.

Melosh, H. J., and C. A. Williams, Jr., Mechanics of graben formation in crustal rocks: a finite element analysis, *J. Geophys. Res.,* 94, 13961-13973, 1989.

McKenzie, D.P., R.L. Parker, The north Pacific: an example of tectonics on a sphere, *Nature*, 216, 1276-1280, 1967.

Miller, M. M., D.J. Johnson, T.H. Dixon, R.K. Dokka, Refined kinematics of the Eastern California Shear Zone from GPS observations 1993-1998, *J. Geophys. Res.*, 106, 2245-2263, 2001.

Molnar, P., P. Tapponnier, A possible dependence of tectonic strength on the age of crust in Asia, *Earth and Planetary Science Letters*, 52, 107-114, 1981.

Molnar, P., H.J. Anderson, E. Audoine, D. Eberhart-Phillips, K.R. Gledhil, E.R., Klosko, T. McEvilly, T.V. McEvilly, D. Okaya, M.K. savage, T. Stern, F.T. Wu, Continuous deformation versus faulting through the continental lithosphere of New Zeland, *Science*, 286, 516-519, 1999.

Morgan, W.J., Rises, trenches, great faults and crustal blocks, *J. Geophys. Res.*, 73, 1959-1982, 1968.

Prescott, W.H., J.C. Savage, J.L. Svarc, D. Manaker, Deformation across the Pacific-North America plate boundary near San Francisco, California, *J. Geophys. Res.*, 106, 6673-6682, 2001.

Reyners, M., R. Robinson, A. Pancha, P. McGint, Stress and strain in a twisted subduction zone, Fiordland, New Zealand, *Geophys. J. Int.*, 148, 637-648, 2002.

Sauber, J., W. Thatcher, S. Solomon and M. Lisowski, Geodetic slip rate for the Eastern

California shear zone and the recurrence time of Mojave Desert earthquake, *Nature*, 367, 264-266, 1994.

Savage, J. C., M. Lisowski, W. Prescott, An apparent shear zone trending north-northwest across the Mojave Desert into Owens Valley, *Geophys. Res. Lett.*,17, 2113-2116, 1990.

Shi, Y., R.G. Allis, New insight to temperature and pressure beneath the central Southern Alps, New Zealand, *New Zealand J. of Geology and Geophys.*, 38, 585-592, 1995.

Stern, T., P. Molnar, D. Okaya, D. Eberhart-Phillips, Teleseismic P wave delays and modes of shorthening the mantle lithosphere beneath South Island, New Zealand, *J. Geophys. Res.*, 105, 21615-21631, 2000.

Sutherland, R., The Australian-Pacific boundary and Cenozoic plate motions in Southwest Pacific: some constraint from GEOSAT data, *Tectonics*, 14, 819-831, 1995.

Sutherland, R., A. Melhuish, Formation and evolution of the Solander Basin, southwestern South Island, New Zealand, controlled by a major fault in continental crust and upper mantle, *Tectonics*, 19, 44-61, 2000.

Thatcher, W., G.R. Foulger, B.R. Julian, J. Svarc, E. Quilty, G.W. Bawden, Present-day deformation across the Basin and Range province, western United States, *Science*, 283, 1714-1718, 1999.

Vine, F.J., D.H. Matthews, Magnetic anomalies over ocean ridges, *Nature*, 199, 947-949, 1963.

Wernicke, B., A.M. Friedrich, N.A Nathan, R.A. Bennett, J.L. Davis, Dynamics of plate boundary fault systems from Basin and Range Geodetic Network (BARGEN) and geological data, *GSA Today*, 10, 1-7, 2000.

Wilson, J.T., A new class of faults and their bearing on continental drift, *Nature*, 207, 343-347, 1965.

CHAPTER 2

INFLUENCE OF THE EARTHQUAKE CYCLE AND LITHOSPHERIC RHEOLOGY ON THE DYNAMICS OF THE EASTERN CALIFORNIA SHEAR ZONE[†]

ABSTRACT

The Eastern California Shear Zone is bounded by the high heat flow region of the Basin and Range province and the low heat flow region of the Sierra Nevada block. This difference in thermal state influences the rheology of the lower crust/upper mantle, resulting in a viscosity contrast between the two regions. We analyze the effect of such a contrast on the kinematics and dynamics of the shear zone with numerical models. This viscosity contrast drives asymmetric strain accumulation in the upper crust, producing an asymmetric surface velocity field. An additional consequence of this strain pattern is the potential for asymmetric co-seismic displacement during an earthquake.

2.1 INTRODUCTION

Models of surface deformation associated with faulting typically assume either a simple elastic half space rheology, or a layered rheology, with an elastic layer overlying one or

---

[†] The content of this chapter has been published as: Malservisi, R., K.P. Furlong, T.H. Dixon, Influence of the Earthquake cycle and lithospheric rheology on the dynamics of the Eastern California shear zone, Geophys. Res. Lett., 28, 2731-2734, 2001.

more viscous or viscoelastic layers. Most such models assume symmetric rheology for strike slip faults, i.e., the crust and upper mantle on either side of the fault are the same. Here we evaluate a region where this assumption may not be valid, using data from the Eastern California shear zone (ECSZ), part of the Pacific-North America plate boundary. The ECSZ accommodates a significant amount (~20%) of the relative motion between the Pacific and North America plates in California [Dokka and Travis, 1990; Sauber et al., 1994; Savage et al., 1990; Dixon et al., 1995, 2000; Gan et al., 2000; Miller et al. 2001]. The 1872 Owens Valley earthquake (estimated magnitude ~8; [Beanland and Clark, 1995]), is also consistent with the idea that significant plate motion is accommodated by the ECSZ. The ECSZ is bounded by the Basin and Range province to the east and the Sierra Nevada/Great Valley block to the west. Heat flow measurements [Blackwell et al. 1998] indicate a relatively sharp transition across the ECSZ with low heat flow on the western side and high heat flow on the eastern side (Figure 2.1). Dixon et al. [2000] showed that this transition coincides with a strong gradient in surface deformation. Assuming thermal equilibrium, the implied variation in lithosphere thermal structure influences the rheology of the lithosphere and produces a viscosity contrast across the shear zone at depth. A high viscosity lower crust/upper mantle will be associated with the cold Sierra Nevada side, with corresponding lower viscosity on the Basin and Range side.

Figure 2.1: Fault-parallel velocity and average heat flow (http://www.smu.edu/~geothermal [Blackwell et al., 1998]) along an ECSZ transect across Owens Valley (dark line). GPS data from Dixon et al. (2000) (dark triangles) and Gan et al. (1999) (light triangles). Data are projected from up to 50 km away onto the profile. Data uncertainties are slightly larger than symbols. OVF and FLF are Owens Valley and Fish Lake Valley fault zones. Star indicates epicenter of the 1872 Owens Valley earthquake.

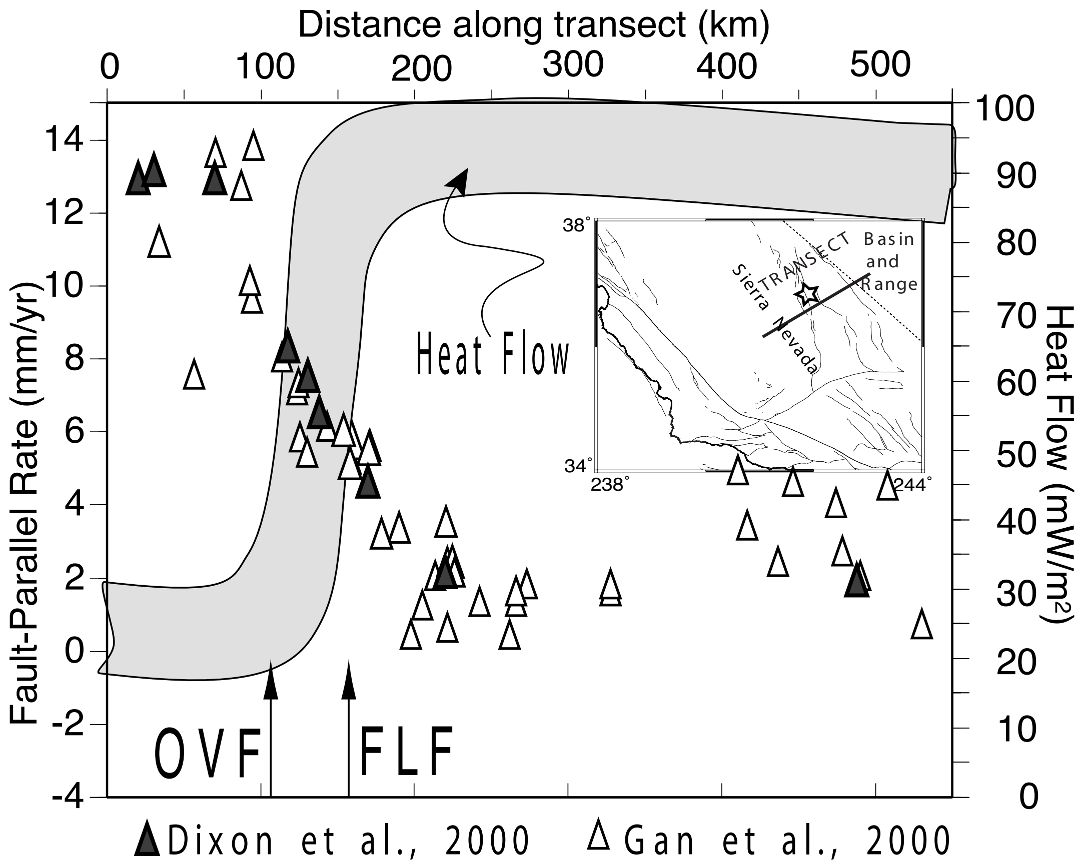

2.2 THE MODEL

From surface deformation data alone, it is not possible to constrain uniquely the rheology at depth. To model the asymmetric velocity field across the ECSZ, Dixon et al., [2000] used faults in different stages of their earthquake cycle, but assumed essentially symmetric lower crustal rheology (Maxwell viscosity 10^{20} Pa s). However, the heat flow data provide an important additional constraint, and imply an asymmetric viscosity distribution. To analyze the deformation field produced by shear strain in association with a viscosity contrast in the lower crust-upper mantle on either side of the ECSZ, we use the finite element model TECTON [Melosh and Raefsky, 1980; Govers, 1983]. We treat the lithosphere as an elastic layer (seismogenic upper crust) overlying a viscoelastic lower crust and lithospheric mantle. The model domain is 500 km wide (x direction, ~E-W), 150 km long (y direction, ~N-S) and 70 km thick (z direction). The elastic layer is 15 km thick and overlies a 55 km thick viscoelastic layer with Maxwell (linear) rheology. The far field boundary conditions are a relative velocity of 12 mm/yr (consistent with GPS observations) applied along the sides of the model in a direction parallel to the fault. The top and the bottom surfaces of the model (z=0 and z=70 km) have an imposed boundary condition of no vertical displacement. Slippery nodes [Melosh and Williams, 1989] are used to simulate a fault oriented along the y direction in the elastic layer. The fault passes through the center of the model and can be locked to different depths. Although the Eastern California shear zone comprises a complex network of faults [Reheis and Sawyer, 1997], the resolution of our mesh does not allow us to study the effects of fault interactions, thus we aproximate this complex fault system as a single master fault.

We consider two model rheologies. In the first, there is no contrast in the viscosity of the viscoelastic layer across the ECSZ (the viscosity of both the Sierra Nevada and Basin and Range regions is set to 10^{19} Pa s). In the second, the viscoelastic layer is divided into two regions with different viscosities. The boundary separating the two regions passes through the center of the model along the plane defined by the fault. The east side simulates the Basin and Range with a low viscosity (10^{19} Pa s) while the west side represents the Sierra block with a higher viscosity (10^{21} Pa s). These viscosities are compatible with the Lachenbruch and Sass [1978] thermal profiles and dislocation creep of olivine [Rutter and Brodie, 1988]. The effect of the 1872 Owens Valley earthquake is simulated by an applied displacement on the two sides of the locked fault (split node method, [Melosh and Raefsky, 1981]) during one time step in the model. In this way, we can produce and monitor post-seismic strain transients consistent with the macro-scale behavior of the earthquake.

2.3 STEADY STATE BEHAVIOR

Steady state deformation models are used to explore the effects of the viscosity structure on the background deformation behavior. We analyze the two end member behaviors of locked/free creeping faults. The shear strain resulting from the model with no viscosity contrast across the ECSZ (homogeneous model) is symmetric with respect to the fault

Figure 2.2: a) Predicted fault-parallel velocity field without a viscosity contrast. Curves show different times after the 1872 earthquake. "Steady state" corresponds to the velocity field immediately before the event. **b)** History of surface displacement with respect to the initial positions of the 7 points at the surface of the model as indicated in figure 2a (Inset). Time 0 corresponds to time of simulated earthquake. Labels on curves show distance from fault. 250 km curves represent motion of points on model boundary and have imposed velocity of (6 mm/yr).

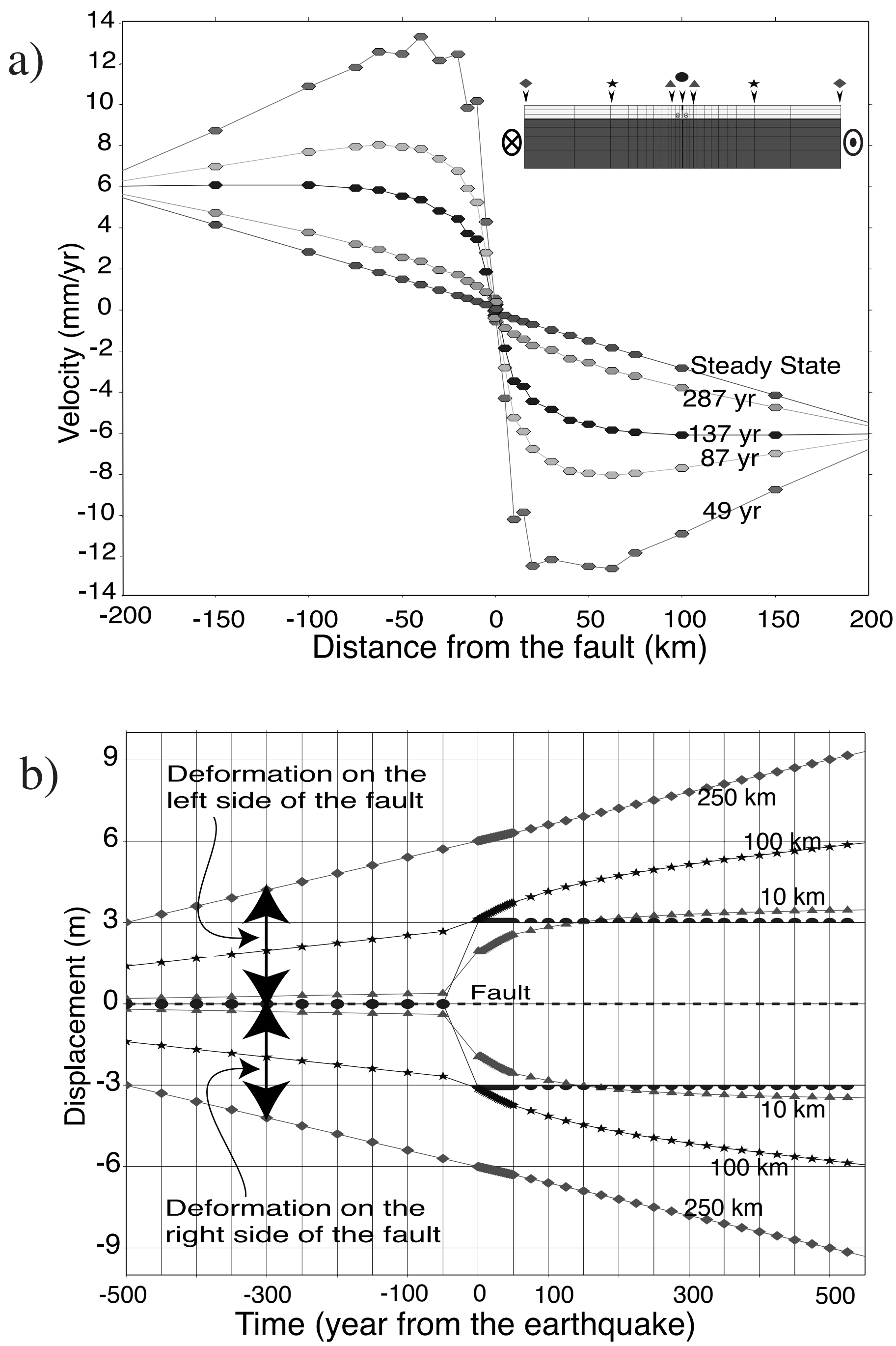

plane. The shear strain is diffuse in the case of a locked fault and more concentrated below the creeping area for a freely creeping fault, consistent with previous analysis (e.g., [Verdonck and Furlong, 1992]). This strain pattern produces a symmetric surface velocity field (Figure 2.2). When we introduce a contrast of viscosity in the viscous layer (the contrast model), a significant difference in strain and velocity is seen. In both cases (free fault and locked fault), the shear strain is concentrated in the "weak" material representing the Basin and Range. Coupling of the viscoelastic layer to the elastic layer will lead to an asymmetric deformation at the surface: the largest gradient in the surface velocity field is shifted to the Basin and Range side as compared to the non-contrast model (Figure 2.3).

2.4 POST-EARTHQUAKE TRANSIENT

The 1872 strike-slip Owens Valley earthquake (with an estimated magnitude ~8) had an average surface slip of 6m over a 100km long rupture [Beanland and Clarck, 1995] (star in Figure 2.1). To simulate this event and to study the post-seismic transient behavior we locked the nodes on the fault plane to a depth of 5 km for 1000 yr and then imposed a differential slip of 6m on the fault during one time step (1 yr). Figure 2.2a shows the fault-parallel velocity field for the homogenous model (along a transect perpendicular to the fault) at a set of times after the simulated earthquake. As expected, the post-seismic transient shows a symmetric pattern decaying with the time and essentially reaching steady state after ~400 yr. Figure 2.2b shows the history of displacement with respect to the initial position of 7 points at the surface on a transect passing through the center of

Figure 2.3: Model results for viscosity contrast in the vicoelastic layer. The figure uses the same notation as figure 2. **a)** Fault-parallel velocity field at different time steps. **b)** History of displacement with respect to initial position of 7 points at the surface of the model indicated on the inset. Note asymmetric surface deformation field at steady state.

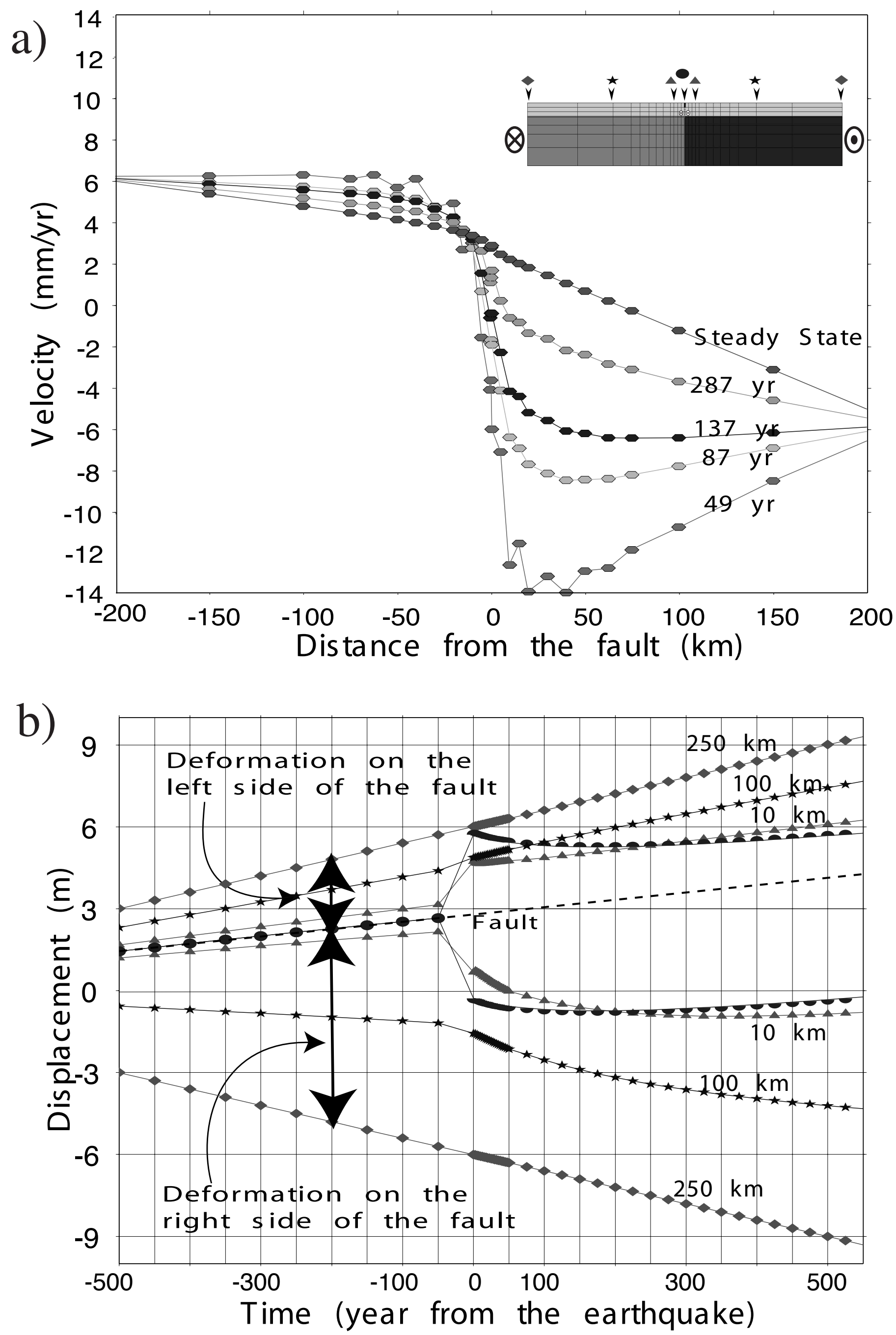

the studied block. The increasing divergence of the lines graphing the displacement of the surface points indicates internal deformation proportional to the elastic shear strain accumulated by the elastic layer. The contrast of viscosity in the viscoelastic layer introduces asymmetry in the system, and the post-seismic transient is no longer symmetric (Figure 2.3a). On the Sierra Nevada side, the perturbation of the fault-parallel velocity field with respect of the steady state is much smaller than the perturbation on the "weak" Basin and Range side. As expected, the smaller deformation on the "strong" Sierra side leads to a faster recovery to the steady state, with a longer transient in the "weak" region. Incidentally, this asymmetric post-earthquake transient indicates that in regions with complex rheologies or geometries, attempts to correct the observed GPS data to remove the earthquake effects must be done prudently. The displacement history (with respect of the original position) of 7 points at the surface (Figure 2.3b) differs from the no-contrast model. During the period prior to the earthquake, points on the western side of the fault move almost parallel to each other (i.e. the Sierra block behaves almost as a rigid block with little internal deformation). However, the displacements of points on the eastern side (Basin and Range) significantly diverge from the western points. This indicates that the deformation is dominantly on the "weak" side. Interestingly, because of different rates of viscous relaxation in the different parts of the model during the post-earthquake period, there is a time when the results for the homogeneous and the contrast models are practically indistinguishable (in our case around 280 yr after the event).

Figure 2.4 shows our model results compared with the fault-parallel velocity field measured with GPS. Curves are plotted at three different time steps for the contrast (Figure 2.4a) and homogenous models (Figure 2.4b). The contrast model results appear to mimic the pattern of the observed velocities quite well. The velocity field is almost flat for the western side; there is a steep gradient close to the fault with a transition to a gentler slope moving to the east. Although both models can satisfy the geodetic observations within the uncertainties, the homogenous model is inconsistent with the heat flow data.

2.5 DISCUSSION

During the pre-earthquake period of strain accumulation in the contrast model, there is a pattern of asymmetric deformation (Figure 2.3b): the western "strong" side is behaving almost as a rigid block with small deformation; the eastern "weak" side accommodates the majority of deformation. The concentration of the deformation in the "weak" side of the model is compatible with the observation of a higher slip rate observed in the faults east of the Owens Valley fault [Reheis and Dixon, 1996] since these faults can be seen as the surface manifestation of shear in the weaker lower crust/upper-mantle. This difference in internal deformation of the two sides implies a difference in shear strain accumulation and thus a difference in the storage of elastic energy. Such a difference in strain accumulation on either side of the fault should be reflected in significant asymmetries in the co-seismic "rebound" on either side of the fault during an earthquake.

Figure 2.4: Model predictions without (**a**) and with (**b**) viscosity contrast at 3 different time steps. Data and faults shown as in Figure 1. Data uncertainties are slightly larger than the symbols.

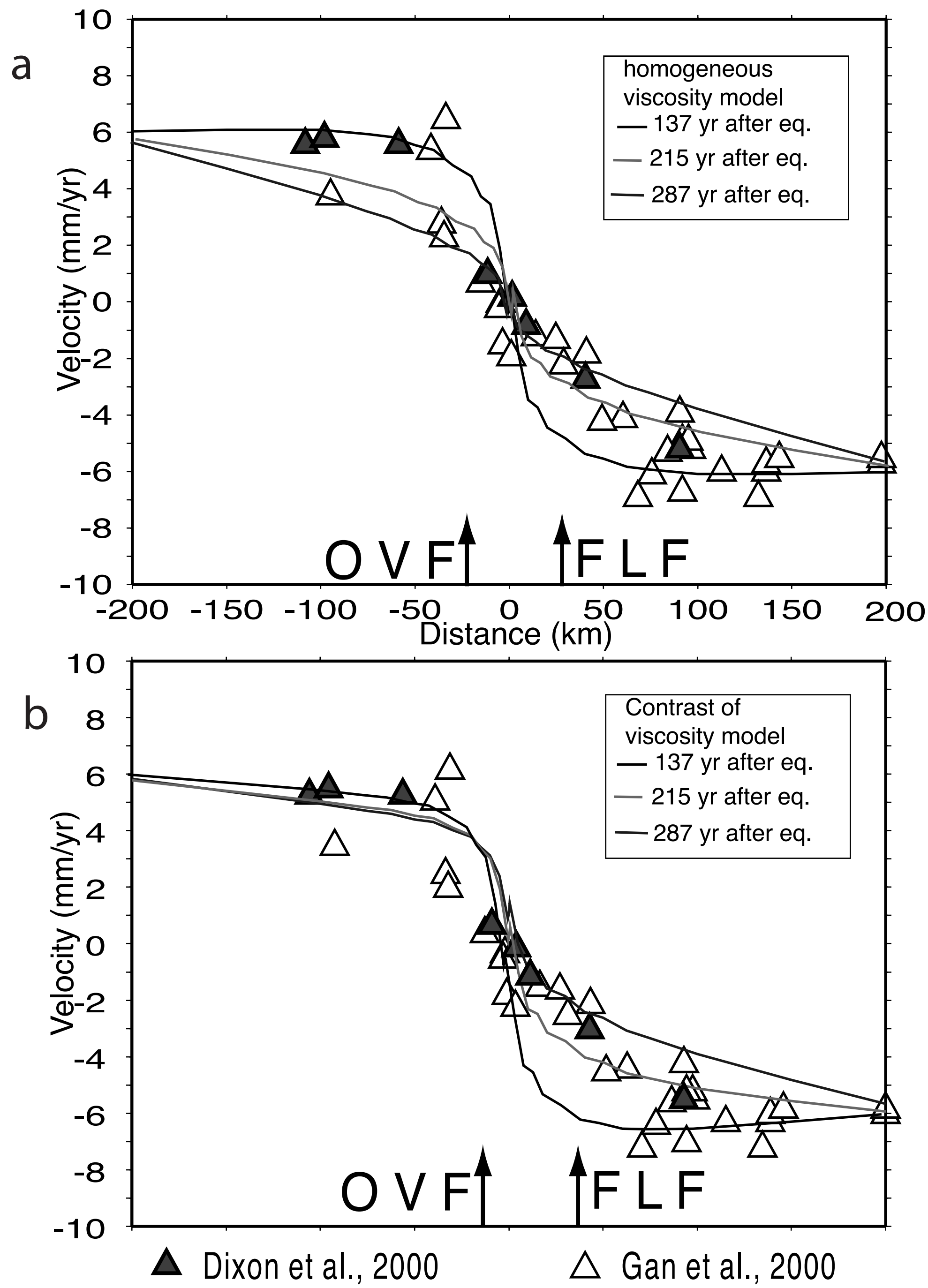

Although we have not specifically analyzed the consequences of such an "asymmetric" earthquake, it seems that effects might be observable in the pattern of strain energy release, ground shaking and/or the seismic radiation pattern. Such asymmetric slip on a strike slip earthquake has been observed elsewhere, although it has been explained with asymmetries in the elastic layer. The November 1997 Manyi, Tibet, earthquake ruptured on an E-W striking fault and shows an asymmetric displacement pattern across the fault [Peltzer et al, 1999]. Asymmetric behavior due to a contrast in elastic properties has been previously analyzed by Sato [1974], Rybicki [1978], and Mahrer and Nur [1979].

2.6 REFERENCES

Beanland, S., and M. M. Clark, The Owens Valley fault zone, eastern California, and surface rupture associated with the 1872 earthquake, *U.S. Geol. Sur. Bull.* 1982, 1995.

Bennett, R.A., J.L. Davis and B.P. Wernicke, Present-day pattern of Cordilleran deformation in the western United States, *Geology*, 27(4), 371-374, 1999.

Blackwell, D.D., K.W. Wisian, and J.L. Steele, Geothermal resource/reservoir investigations based on heat flow and thermal gradient data for the United States, *http://www.smu.edu/~geothermal*, 1998.

Dixon, T.H., S. Robaudo, J. Lee and M.C. Reheis, Constraints on present-day Basin and Range deformation from space geodesy, *Tectonics*, 14(4), 755-772, 1995.

Dixon, T.H., M. Miller, F. Farina, H. Wang and D. Johnson, Present-day motion of the Sierra Nevada block and some tectonic implications for the Basin and Range Province, North America Cordillera, *Tectonics*, 19(1), 1-24, 2000.

Dokka, R.K., Travis, C.J., Role of the Eastern California Shear Zone in accomodating Pacific-North America plate motion, *Geophys. Res. Lett.*, 17(9), 1323-1326, 1990.

Govers, R., Dynamics of Lithospheric Extension: A Modeling Study. Ph.D. Thesis, University of Utrecht, *Geologica Ultraiectina* 105, 1-240, 1993.

Gan, W., J.L. Svarc, J.C. Savage and W.H. Prescott, Strain accumulation across the Eastern California Shear Zone at latitude 36 30'N, *J. Geophys. Res.*, 105, 16229-16236, 2000.

Lachenbruch, A.H., Sass, J.H., Models of an extending lithosphere and heat flow in the Basin and Range Province, *Memoir - Geological Society of America*, 152, 209-250, 1978.

Mahrer, K.D., A., Nur, Static strike-slip faulting in a horizontally varying crust, *Bull. Seismol. Soc. Am.*, 69, 975-1009, 1979.

Melosh, H. J., and A. Raefsky, The dynamical origin of subduction zone topography, *Geophys. J. R. Soc.* 60, 333-354, 1980.

Melosh, H. J., and A. Raefsky, A simple and efficient method for introducing faults into finite element computations, *Bull. Seismol. Soc. Am.*, 71(5), 1391-1400, 1981.

Melosh, H. J., and C. A. Williams, Jr., Mechanics of graben formation in crustal rocks: a finite element analysis, *J. Geophys. Res.,* 94, 13961-13973, 1989.

Miller, M. M., D.J. Johnson, T.H. Dixon, R.K. Dokka, Refined kinematics of the Eastern California Shear Zone from GPS observations 1993-1998, *J. Geophys. Res.*, 106, 2245-2263, 2001.

Peltzer, G., F., Crampe and G. King, Evidence of nonlinear elasticity of the crust from the Mw 7.6 Manyi (Tibet) Earthquake, *Science*, 286, 272-276, 1999.

Reheis, M.C., Dixon, T.H., Kinematics of the Eastern California shear zone; evidence for slip transfer from Owens and Saline Valley fault zones to Fish Lake Valley fault zone, *Geology*, 24(4), 339-342, 1996.

Reheis, M.C., Sawyer, T.L., 1997, Late Cenozoic history and slip rates of Fish Lake Valley, Emigrant Peak, Deep Springs fault zones, Nevada and California, *Geol. Soc. Am. Bull.*, 109(3), 280-299, 1997.

Rutter, E.H., K.H., Brodie, The role of tectonic grain size reduction in the rheological stratification of the lithosphere, *Geol. Rund.*, 77, 295-308, 1988.

Rybicki, K., Static deformation of a laterally inhomogeneous half-space by a two-dimensional strike-slip fault, *J. Phys. Earth*, 26, 351-366, 1978.

Sato, R., Static deformations in an obliquely layered medium. Part 1. Strike-slip fault., *J. Phys. Earth*, 22, 455-462, 1974.

Sauber, J., W. Thatcher, S. Solomon and M. Lisowski, Geodetic slip rate for the Eastern

California shear zone and the recurrence time of Mojave Desert earthquake, *Nature*, 367, 264-266, 1994.

Savage, J. C., M. Lisowski, W. Prescott, An apparent shear zone trending north-northwest across the Mojave Desert into Owens Valley, *Geophys. Res. Lett.*,17, 2113-2116, 1990.

Verdonck, D., K.P., Furlong, Stress accumulation and release at complex transform plate boundaries, *Geophys. Res. Lett.*, 19, 1967-1970, 1992.

CHAPTER 3

NUMERICAL MODELING OF STRIKE-SLIP CREEPING FAULTS AND IMPLICATIONS FOR THE HAYWARD FAULT, CALIFORNIA[§]

ABSTRACT

The seismic potential of creeping faults such as the Hayward fault (San Francisco Bay Area, CA) depends on the rate at which moment (slip deficit) accumulates on the fault plane. Thus, it is important to evaluate how the creep rate observed at the surface is related to the slip on the fault plane. The surface creep rate depends on the geometry of locked and free portions of the fault and on the interaction between the fault zone and the surrounding lithosphere. Using a visco-elastic finite element model, we investigate how fault zone geometries and physical characteristics such as frictionless or locked patches affect the observed surface creep when the system is driven by far field plate motions. These results have been applied to creep observations of the Hayward fault. This analysis differs from most previous fault creeping models in that the fault in our model is loaded by a distributed viscous flow induced by far field velocity boundary conditions instead of imposed slip beneath the major faults of the region. The far field velocity boundary conditions simulate the relative motion of the stable Pacific Plate respect to the Rigid

---

[§] This Chapter has been submitted to Tectonophysics as: Malservisi, R., K.P. Furlong, C. Gans, Numerical modeling of creeping faults and implications for the Hayward fault, California.

Sierra Nevada block, leaving the rheology, fault geometry and mechanics (locked or free to creep patches), to determinate the patterns of fault creep.

Our model results show that the fault geometry (e.g. length and depth of creeping) and the local rheology influence the surface creep rate and the slip on the fault plane. In particular, we show that the viscoelastic layer beneath the elastic seismogenic zone plays a fundamental role in loading the fault. Additionally, the coupling with the surrounding lithosphere results in a smooth transition from regions free to creep to locked patches.

3.1 INTRODUCTION

Strike-slip faults, while mostly remaining locked between large stress-releasing events, can, in some cases, creep. Surface creep has been documented in two major continental strike-slip fault systems: the North Anatolian fault in Turkey [e.g. Ambraseys, 1970, Aytun, 1980; Sylvester, 1988], and the San Andreas and its related faults in California [e.g. Lienkaemper et al., 1991; Galehouse, 1992; Lienkaemper and Galehouse, 1998]. Although the occurrence of creep is documented, the interactions between locked and creeping portions of a fault and the conditions that lead to creep are not well understood.

Fault creep is an important issue, especially for earthquake risk assessment. The causes and the depth extent of creep on faults are not typically known, making risk assessment problematic. If creep extends through the seismogenic layer and matches the long-term slip rates, then earthquakes would not likely initiate on that area of the fault. However, if the creeping zone extends only to a shallow depth, or if the creep velocity does not match the long-term slip rate, a slip deficit can build, increasing the potential seismic moment for an earthquake on that segment of the fault.

The geometry of the fault section able to creep (unlocked), the length of the creeping section, the degree of coupling with the surrounding lithosphere, and the rheological properties of the lithosphere all play fundamental roles in the creeping process. Previous analyses reached conflicting conclusions as to the extent of creep on the Hayward fault. Prescott et al [1983], suggest deep slip on the fault based on limited comparison of near field and far field geodetic data. Lienkaemper et al [1991] could not resolve patterns of slip on the Hayward fault. Savage and Lisowski [1993], Bürgmann et al. [2000], and Simpson et al. [2001] all have proposed differing models for the extent and depth of creep on the Hayward fault. Using a 2D model, Savage and Lisowski [1993] proposed that the creeping zone on the Hayward fault extends to ~5 km depth, with the fault locked from 5 km to the base of the seismogenic layer. Burgmann et al. [2000], suggest little if any locking along the northern Hayward Fault. They inverted the surface creep rate and the local long-term strain field to estimate the amount of creep on the fault plane and to map the area with a slip deficit. Bürgmann et al. [2000], used GPS and InSAR data to constrain a 3D boundary element model. They argue that previous geodetic data did not allow for creep depth differentiation, but the addition of the GPS and InSAR data mitigates that problem. A best-fit to the geodetic and InSAR data is obtained when the northern 20 km of the Hayward fault is allowed to creep throughout the seismogenic zone, and creep in the south is restricted to shallower depths. Simpson et al. [2001], on the other hand, matched surface creep rate data using a different 3D boundary element model formulation, but with a significantly different pattern of fault creep.

A recently implemented approach for modeling fault/lithosphere interaction [Malservisi et al., 2001] allows us to address fault creep in a different way and to test the influence of tectonic forces on the creeping process. In particular, we can test the response of fault segments to the far field velocities and evaluate what conditions promote fault zone creep.

The Hayward fault (Figure 3.1) located on the east side of San Francisco Bay, is part of the San Andreas fault system and is a well-documented creeping fault. At the surface it is undergoing right-lateral creep at an average rate of 5 mm/yr, as compared to an inferred long-term fault slip rate of 9 to 10 mm/yr [Lienkaemper et al., 1991; Galehouse, 1992; Lienkaemper and Galehouse, 1998; Bürgmann et al., 2000; Lienkaemper et al., 2001]. The last major earthquake on the 82 km long fault (M = ~6.8) occurred in 1868, with surface rupture over the southern ~ 60 km of the fault [Lienkaemper et al., 1999]. Prior to the 1868 event, there is evidence for another earthquake on the northern segment of the Hayward Fault between 1640 and 1776 AD [Toppozada and Borchard, 1998; Lienkaemper et al., 1999].

Figure 3.1: a) Geometry and mesh for the Finite Element modeling in this study. The lithosphere is simulated through a 12 km thick elastic layer (white) over a linear viscoelastic region (gray). The dark gray region is assigned the same viscosity of the light gray area (homogeneous models) or a lower viscosity (shear zone models). A far field velocity boundary condition drives the system. The dark line at the center of the model represents the fault and specifies the area that can be allowed to creep. **b)** Extent of the model in the geographic reference of the San Francisco Bay area. The thick lines indicate the active faults mapped in the area (Jennings, 1994). The thickest line at the center of the mesh indicates the creeping segment of the Hayward fault.

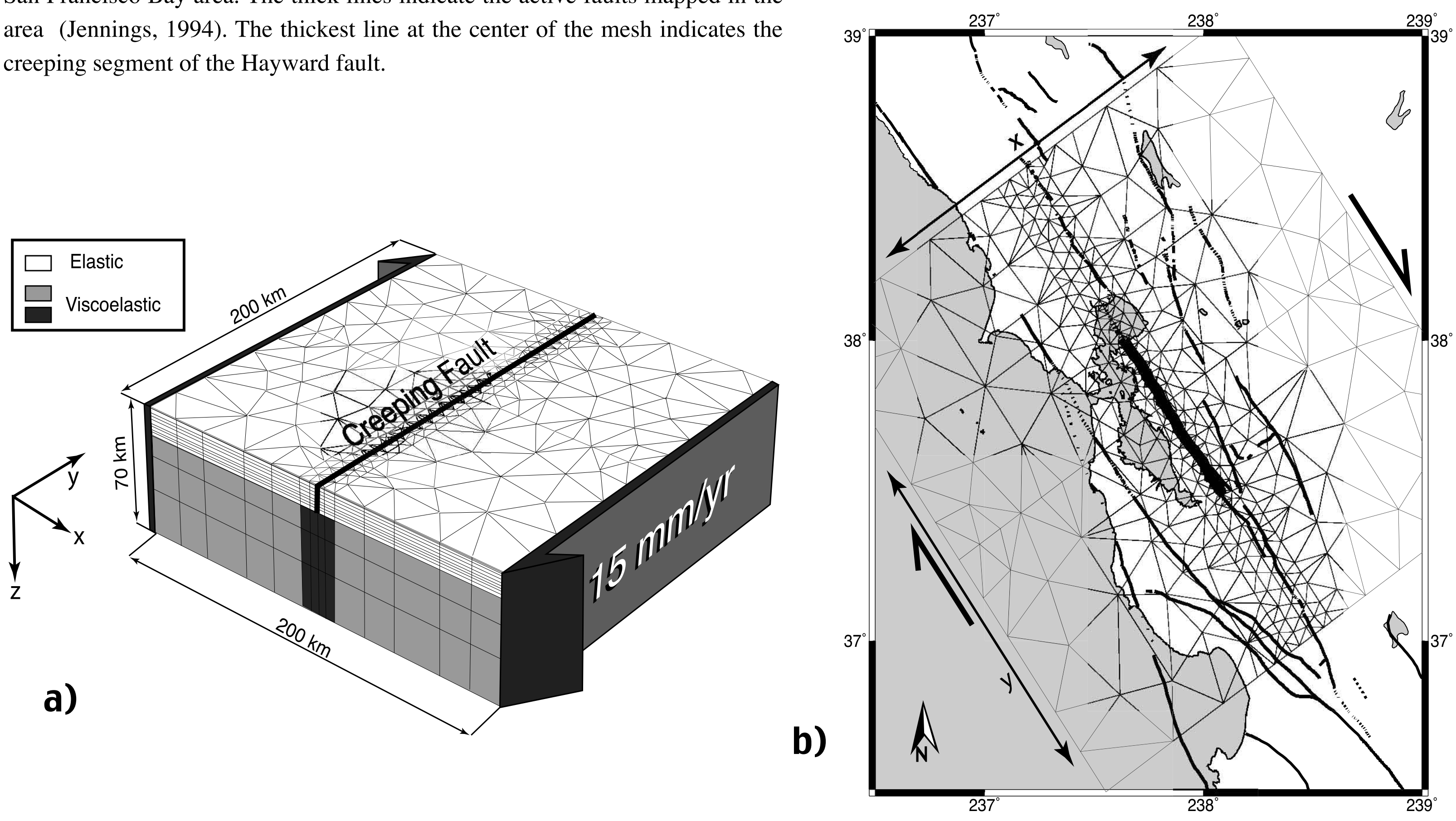

In all of the previous models [i.e. Savage and Lisowski, 1993; Burgman et al., 2000; Simpson et al., 2001], the goal was to fit surface geodetic data by specifying patterns of creep on the fault. In our modeling, we impose a far-field relative velocity on the sides of the model (Figure 3.1a) to examine the conditions under which creep can occur. Our models allow for "creepable" elements that have the potential to creep, but are not forced to do so. This approach allows us to test the influence of various parameters (e.g. fault length, viscosity, and geometry of the creepable/locked zones) on the potential of a fault to undergo creep.

3.2 THE MODEL

Our model approach allows us to test the conditions that drive creep on a fault in response to velocity boundary conditions applied in the far field. The goal is to examine the relationship between the physical characteristics of a fault and its potential to creep. We use a 3-D version of the finite element code TECTON [Melosh and Raefsky, 1980; Govers, 1993; Govers et al 2000; Govers and Meijer, 2001] to simulate different crust/lithosphere rheologies, fault geometries and fault properties (free/locked patches). Figure 3.1 shows the model geometry and the geographic position of the mesh. The model is 200 km wide (x direction, ~ SW-NE), 200 km long (y direction, ~NW-SE), and 70 km thick (z direction). We simulate the lithosphere as a 2-layer block. A shallow elastic layer represents the seismogenic crust, overlays a viscoelastic layer with a Maxwell (linear) rheology and variable viscosities that simulate the lower crust/upper mantle. Consistent with the thickness of the seismogenic layer along the Hayward fault, we specify the elastic layer to be 12 km thick. Micro-seismicity studies in the Hayward region show that the seismogenic layer is confined to the top 12 km [Waldhauser and Ellsworth, 2000]. We have tested the effect of viscosity variations in the viscoelastic layer and of a lower viscosity area localized beneath the creeping fault on creep behavior (viscosity ranging from 10^{18} Pa s to 10^{21} Pa s). The low viscosity region is included to simulate the presence of a narrow shear zone associated with the evolution of the North America/Pacific plate boundary due to the migration of the Mendocino Triple Junction [Furlong et al., 1989; Furlong, 1993, Furlong and Verdonk, 1993].

The creeping fault is defined using the method of "slippery nodes" [Melosh and Williams, 1989]. By adding a degree of freedom to a specific node, the method allows the slippery node to behave as if it were split into two parts. This allows a differential displacement along a fixed direction without friction. The actual amount of differential displacement depends on the local force field. In this way the slippery nodes represent the areas of the fault plane that have the potential to creep. In the models presented here, the fault plane is defined as a vertical plane oriented in the y direction, passing through the center of the model (x = 0). The fault is symmetric with respect to the center of the mesh (tips at y = ± L/2 where L = length of the fault) and free to creep from the surface to a specified depth in the seismogenic layer (maximum depth = 12 km). All the slippery nodes on this plane can potentially creep along the fault plane direction (“creepable” nodes) and the amount of differential displacement is dependent on the local force field.

To define locked patches on the fault plane we specify the corresponding nodes as "bound" or not slippery.

In all the models, the creep rate is defined as the average of differential displacement across the fault plane at two time steps divided by the time. In this way, creep is zero on all locked sections and within the viscoelastic layer, although elastic or viscoelastic deformation may occur in those regions.

In the San Francisco Bay area, the Pacific plate moves at ~47 mm/yr with respect to the North America plate [DeMets et al., 1994]. Approximately 12 mm/yr of this plate motion is accommodated along the Eastern California shear zone [e.g. Dixon et al., 2000] leaving about 35 mm/yr to be accommodated in the San Francisco Bay area (comparable with regional GPS and InSAR observations, e.g. Bürgmann et al., [2000], Argus and Gordon [2001]). Furlong et al. [1989] suggested that deep creep on the San Andreas alters the velocity field and Lisowki et al. [1991] indicated that that creep produces ~5 mm/yr near the San Andreas fault. The single fault model that we utilize in this study assumes that the remaining relative displacement is the far field velocity that drives the creeping on the Hayward fault. Thus a far field relative velocity of 30 mm/yr drives the deformation of our models. This is implemented as an applied velocity boundary condition along the side of the mesh (±15 mm/yr. at x = ± 100 km, Figure 3.1) in a direction parallel to the fault. In order to minimize the effect of the singularity at the tip of the fault, no vertical displacement is allowed at the top and bottom surfaces (z = 0 and 70 km respectively).

3.3 GENERAL PARAMETERS INFLUENCING CREEPING BEHAVIOR

We ran a suite of models to test the influence of different fault parameters on creeping behavior. Table 3.1 lists the parameters used in all our models, with a short definition of each. The first set of model runs were intended to test effects of rheological properties. Models 1 - 3 are described in Table 3.2. Once the best rheological model was determined, different model geometries were studied. Models 4 - 6 are described in Table 3.3.

Table 3.1: Parameters

Parameter	Description	Range / Value
L	**Length:** Fault length	10 km -
MSCR	**Maximum Surface Creep Rate:** Maximum creeping rate at the surface along the fault plane	mm/yr.
SCR	**Surface Creep Rate:** Creeping rate at the surface along the fault plane as a function of position	mm/yr.
TLD	**Top Locking Depth:** Depth at which the creeping section of the fault connected to the surface is locked	0-12 km
BLD	**Bottom Locking Depth:** Depth below which the seismogenic layer is allowed to creep	0-12 km

Table 3.2: Rheological Models

Model name	**Viscosity viscoelastic layer (Pa·s)**	**Viscosity Low viscosity zone (Pa·s)**	**Viscoelastic layer**
Model 1a	$1\ 10^{18}$	$1\ 10^{18}$	Homogeneous
Model 1b	$1\ 10^{19}$	$1\ 10^{19}$	Homogeneous
Model 1c	$1\ 10^{21}$	$1\ 10^{21}$	Homogeneous
Model 2	$1\ 10^{20}$	$1\ 10^{18}$	With Shear zone
Model 3	$1\ 10^{21}$	$1\ 10^{18}$	With Shear zone

Table 3.3: Model Geometries

Model name	**Model Description**
Model 4a	Fault locked from 4 km to 12 km
Model 4b	Fault locked from 4 km to 8 km (Fault free to creep from 0 - 4 km and 7 - 12 km)
Model 4c	Fault locked from 6 km to 12 km
Model 4d	Fault entirely free to creep from 0 km to 12 km
Model 5a	Fault free to creep from 0 km to 12 km
Model 5b	Fault free to creep from 0 km to 12 km, “creepable” zone extending beyond fault from 4 km to 12 km
Model 5c	Fault free to creep from 0 km to 12 km, “creepable” zone extending beyond fault from 6 km to 12 km
Model 5d	Fault free to creep from 0 km to 12 km, “creepable” zone extending beyond fault from 4 km to 12 km in a gradational pattern
Model 6a	Fault free to creep from 0 km to 12 km depth for 0 km to 41 km in length, fault locked from 4 km to 12 km for 41 km to 82 km in length
Model 6b	Fault locked from 6 km to 12 km for two 15km wide zones, with 10 km between fully “creepable” to depth
All faults are 82 km long, with a 12 km thick elastic layer and a 58 km thick viscoelastic layer. The viscosity is 10^{18} Pa·s in the shear zone and 10^{21} Pa·s in the viscoelastic layer.	

3.3.1 Fault length

The length of the “creepable” section of the fault is one of the main controls on the maximum surface creep rate (MSCR). This result is compatible with the observed

Figure 3.2: Maximum creep at the surface versus fault length for different rheological models. The different symbols correspond to the results for different rheological models. The horizontal dashed lines correspond to the asymptotic value (infinite fault) for the given model while the corresponding curved lines show the interpolated exponential relationship. The three points in the insert show the results for an homogeneous model with three different viscosities.

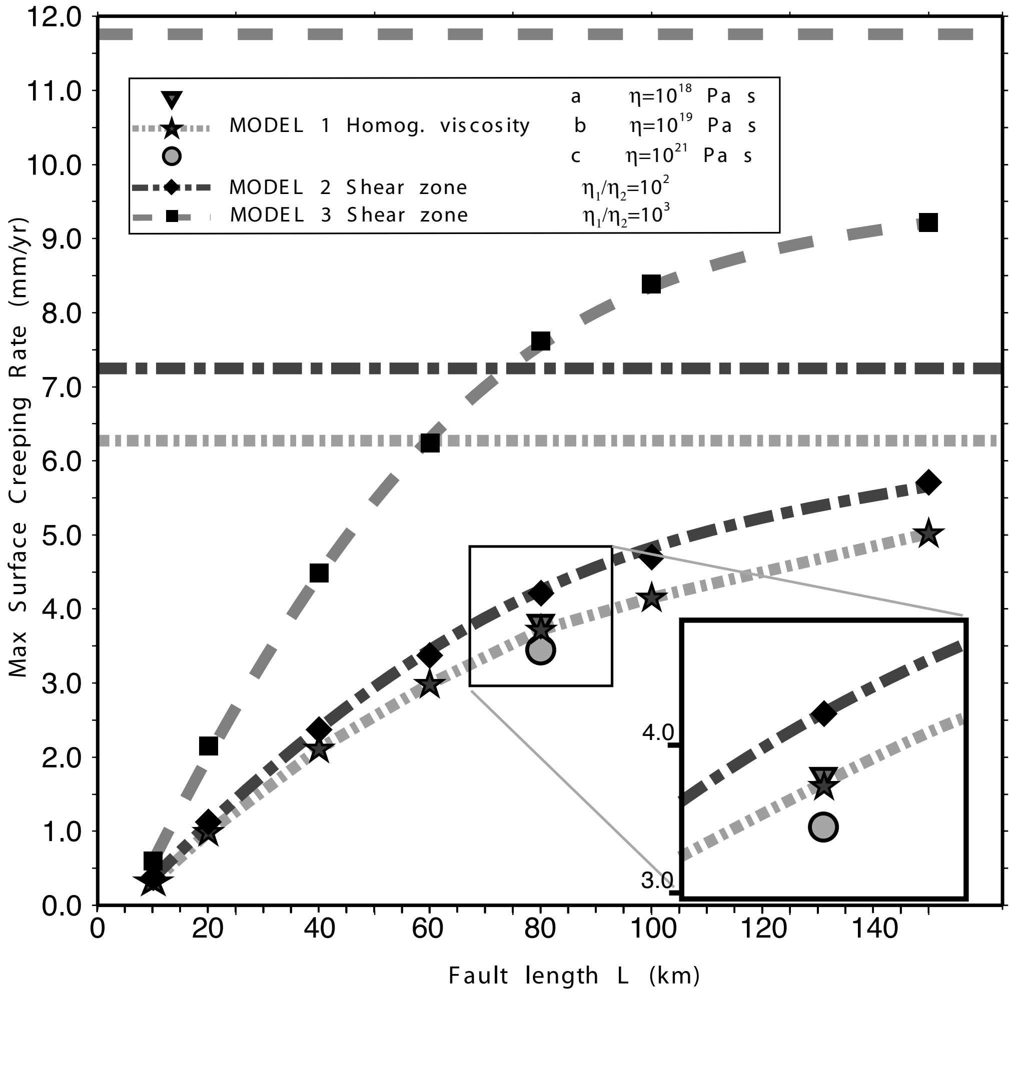

relationship between fault length and geological slip rate (i.e. Bilham and Bodin, 1992). Figure 3.2 summarizes the variation of MSCR as a function of fault length for different rheological models. In this set of simulations, the fault cuts through the entire seismogenic layer (0-12 km) and is "creepable" from y = -L/2 to y = L/2. The infinite fault case is simulated by defining all the nodes of the elastic layer on the plane x = 0 km as slippery. The MSCR increases as the fault becomes longer and asymptotically approaches the value for an infinite length fault (horizontal line in the graph). For each modeled rheology the relationship between MSCR and the length of the creeping section of the fault seem to follow an exponential expression of the form

$$(MSCR) = -A\, e^{-\frac{L}{B}} + C$$

where A and B are model-dependent constants, and C is the asymptotic (infinite fault length) value (dashed line in Figure 3.2).

3.3.2 Lower lithosphere viscosity

In the case of homogeneous viscosity, the MSCR is not sensitive to the absolute value of the viscosity. Results for an 80 km long fault (insert Figure 3.2) show the MSCR for three different viscosities (Model 1a: 10^{18} Pa·s, Model 1b: 10^{19} Pa·s, and Model 1c: 10^{21} Pa·s). The difference between the results (~ 0.2 mm/yr.) is smaller than measurement sensitivity with the system driven by specified displacement rate along the side boundaries, and in the absence of a feature to localize strain (e.g. a fault or a shear zone), we are essentially imposing a uniform shear strain across the model domain. For this reason, the shear strain in the homogeneous viscoelastic material is constant for the different viscosities and the driving force on the fault is constant. Consequently, although an increase in viscosity will increase both the time required to reach the steady state as well as the internal stress in the viscoelastic material, it will not affect the MSCR.

Because the MSCR is dependent on the shear strain rate applied to the base of the creeping section, when the far-field velocity drives the model with a uniform viscoelasticity, creep on the fault accommodates a relatively small fraction of the deformation. By including a low-viscosity zone beneath the fault, we effectively localize the shear strain in the viscoelastic layer. As the contrast of viscosity between the shear zone and the rest of the viscoelastic layer is increased, more strain is localized in the shear zone. For a contrast in viscosity of 3 orders of magnitude and a shear zone 20 km wide (Model 3), a geometry compatible with previous thermal/rheological models for the San Francisco Bay area [Furlong and Verdonck, 1993], almost all the deformation within the viscoelastic layer is concentrated in the shear zone and creep on the fault accommodates a higher fraction of the relative displacement. It is also interesting to note that the narrower the shear zone, the more the resultant stresses will be approximated by the deep slip model of Savage and Lisowski [1991], Bürgmann et al. [2000], and Simpson et al. [2001].

3.3.3 Locking depth

Another important parameter in the analysis of the MSCR is the depth at which a “creepable” fault is no longer allowed to creep but becomes locked (Top Locking Depth,

Figure 3.3: Maximum creep at the surface for three different models as function of depth to the base of the creeping section (locking depth). For each model the fault can creep from the surface down to the locking depth and is locked below this point. The maximum “creepable” depth corresponds to the elastic thickness. The inverse triangle and the square symbols correspond to a model with a low viscosity zone and different length of the “creepable” area. The star corresponds to a homogeneous viscoelastic layer.
The dashed line correspond to the result of Savage and Lisowski for a infinite fault in elastic half-space creeping to the given depth. The fault is loaded only from the dislocation beneath the seismogenic layer with a rate of 9 mm/yr.

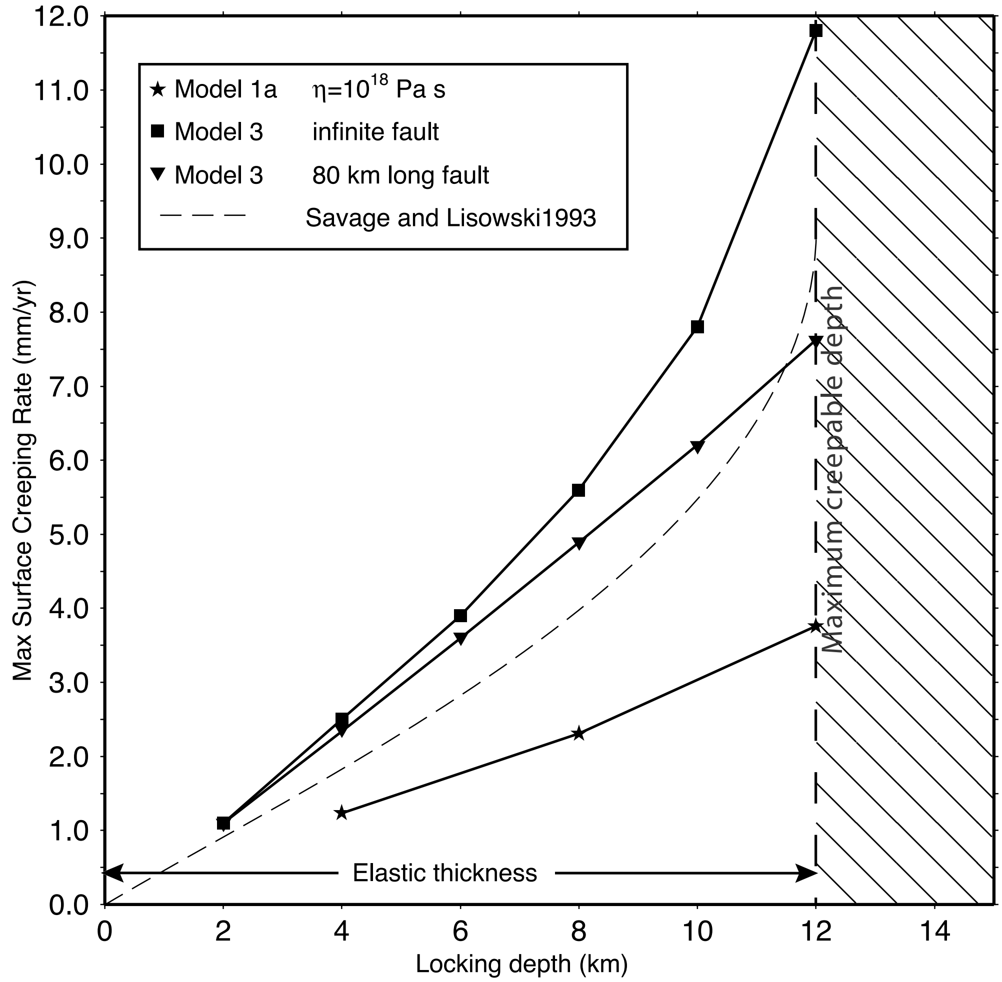

TLD). For a creeping fault in elastic half space, Savage and Lisowski [1993] suggested that the creep rate observed at the surface on a creeping fault is related to the depth to which creep extends. This result also holds for our models although we find a somewhat different relationship between TLD and surface creep rate as compared to the relationship suggested by these previous studies, the result holds also in our model. The dashed line in Figure 3.3 shows the surface creep for the Savage and Lisowski model. In general, the grater this depth, the larger the area free to creep and the faster the surface creep rate (SCR). Figure 3.3 shows the MSCR for different locking depths, rheological models, and fault lengths. The pattern of creeping rate on the fault plane and the creep rate at the surface (SCR) along the fault for three different fault TLDs are plotted in Figure 3.4. As expected, the MSCR increases in a non-linear fashion as the locking depth increases, for all models. In Figure 3.3 we see that the infinite-length fault is more sensitive to the locking depth than a finite-length fault. In the case of a finite fault, the creep is limited by stress accumulation at the fault tips. The difference in MSCR between the different rheological and fault-length models increases as the locking depth increases. For a very shallow locking depth, where the system is dominated by the behavior of the elastic layer, the difference in MSCR is negligible. Figure 3.4 compares three creeping faults of 82 km length locked to different depths and geometries. Model 4a shows the fault plane creep rate for a fault free to creep in the top 4 km and locked below this depth. Model 4b corresponds to a similar fault, free to creep down to 4 km (TLD), but locked from 4 km to 8 km and “creepable” from 8 km (Bottom Locking Depth, BLD) to the bottom of the seismogenic zone. In Model 4c the fault is free to creep from the surface to 6 km and

Figure 3.4: Models 4a - 4d. Models contain an 82 km fault with "creepable" patches extending to various depths. "Creepable" regions are enclosed by heavy dark lines. Regions shallower than 12 km and outside "creepable" zones are locked. Regions deeper than 12 km deform in a viscoelastic way. Shading indicates creep rates on fault plane. Figure 4e: Surface creeping rate as a function of position along fault for Models 4a - 4d. Increasing the depth of the "creepable" zone increases the surface creeping rate. The deformation is driven by far field velocity of 30 mm/yr.

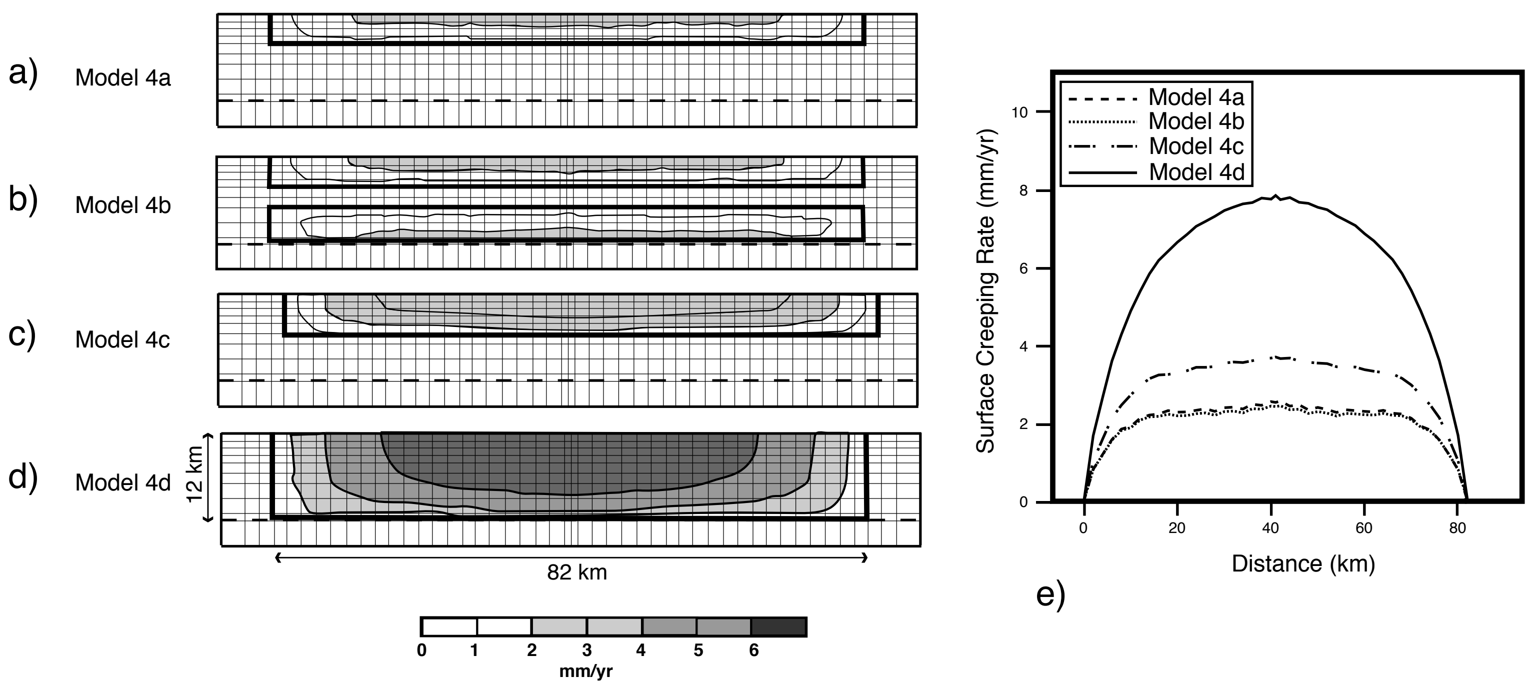

locked below this depth. Finally, the fault is “creepable” throughout the entire seismogenic layer in Model 4d. Figure 3.4e shows the surface creep rate (SCR) along the fault for the different models. As expected, when locking depth increases, MSCR increases. In the case of an 82 km long fault with the rheology of Model 3, the MSCR increases from 2.4 mm/yr for Models 4a and 4b (independent of the deep creeping behavior), to 3.7 mm/yr for Model 4c to 7.8 mm/yr for Model 4d.

Although the “creepable” surface in Model 4b is twice as large as in Model 4a, the surface creeping patterns of the two models are indistinguishable. Furthermore, the MSCR for these two models is much smaller than that observed for Model 4c, containing a “creepable” surface intermediate in area between Models 4a and 4b. These results suggest that the surface creep pattern is mainly influenced by the locking depth of the creeping area connected to the surface (TLD), and is not influenced to any large extent by fault behavior beneath a locked patch. This may be an important factor to consider in seismic risk assessment. Although the surface creep patterns for Models 4a and 4b are the same, Model 4a has substantially larger integrated slip deficit and thus could likely generate a greater seismic moment during an earthquake.

3.3.4 Fault tips and connectivity

How creeping fault segments terminate and the nature of strain accumulation at the tips of creeping sections is uncertain. Models 5a - 5d test some simple scenarios of fault tip behavior. Model 5a corresponds to a single, 82 km fault free to creep throughout the entire seismogenic layer. This is the geometry used to study the relationship between MSCR and fault length or locking depth. In Models 5b - 5d, the 82 km fault is connected at its ends with faults locked at the surface but allowed to creep below a fixed depth (BLD). The possible connections of the Hayward fault with the Calaveras fault in the south and the Rodgers Creek fault at the northern end may be geologic examples of this geometry. To simulate this interaction, we allowed the segment of the fault between y = ± 41 km to creep from the surface down to 12 km and locked the fault plane from the surface to a fixed depth (BLD) elsewhere. Model 5b and 5c correspond to different values of BLD. Model 5d contains a smoother transition between the creeping and the locked part of the system, with an increasing value of BLD outside the 82 km range. Despite the different creeping rates deep on the fault plane (Figures 3.5a – 3.5d), the surface creep rates seen in Figure 3.5e do not show significant differences and do not allow one to distinguish among the different models.

Bilham and Bodin [1992] show that the connectivity of different fault segments influences the amount of fault slip. Furthermore, with the exception of InSAR type studies, observations of creep are usually only made at discrete points along the fault. Thus it is possible that observed creeping sections may sometimes be disconnected despite the nearness of the creeping patches. To test how isolated creeping segments influence each other, we tested a model with two separated creeping segments. We analyzed the creep rate of two 40 km long "creepable" faults separated by patches locked from the surface to the bottom of the seismogenic layer. For locking patches as narrow as

Figure 3.5: Models 5a - 5d. Models contain an 82 km fault extending to the bottom of the seismogenic zone (12 km). Model 5a: Creep is only possible on the 82 km fault, extending the entire depth (12 km). For Models 5b - 5d the fault is allowed to creep for the entire model length (200 km) at lower seismogenic zone depths. Model 5b: Creep extends from 4 km to 12 km depth outside the fault. Model 5c: Creep extends from 7 km to 12 km depth outside the fault. Model 5d: Creep zone extent outside the fault decreases from initiating at an upper depth of 4 km to 7 km, extending to the base of the seismogenic zone at 12 km depth. Figure 5e: Surface creeping rate as a function of distance for Models 5a - 5d. Fault properties representation as in Figure 4. Note that the shading scale is different from the one on the other figures.

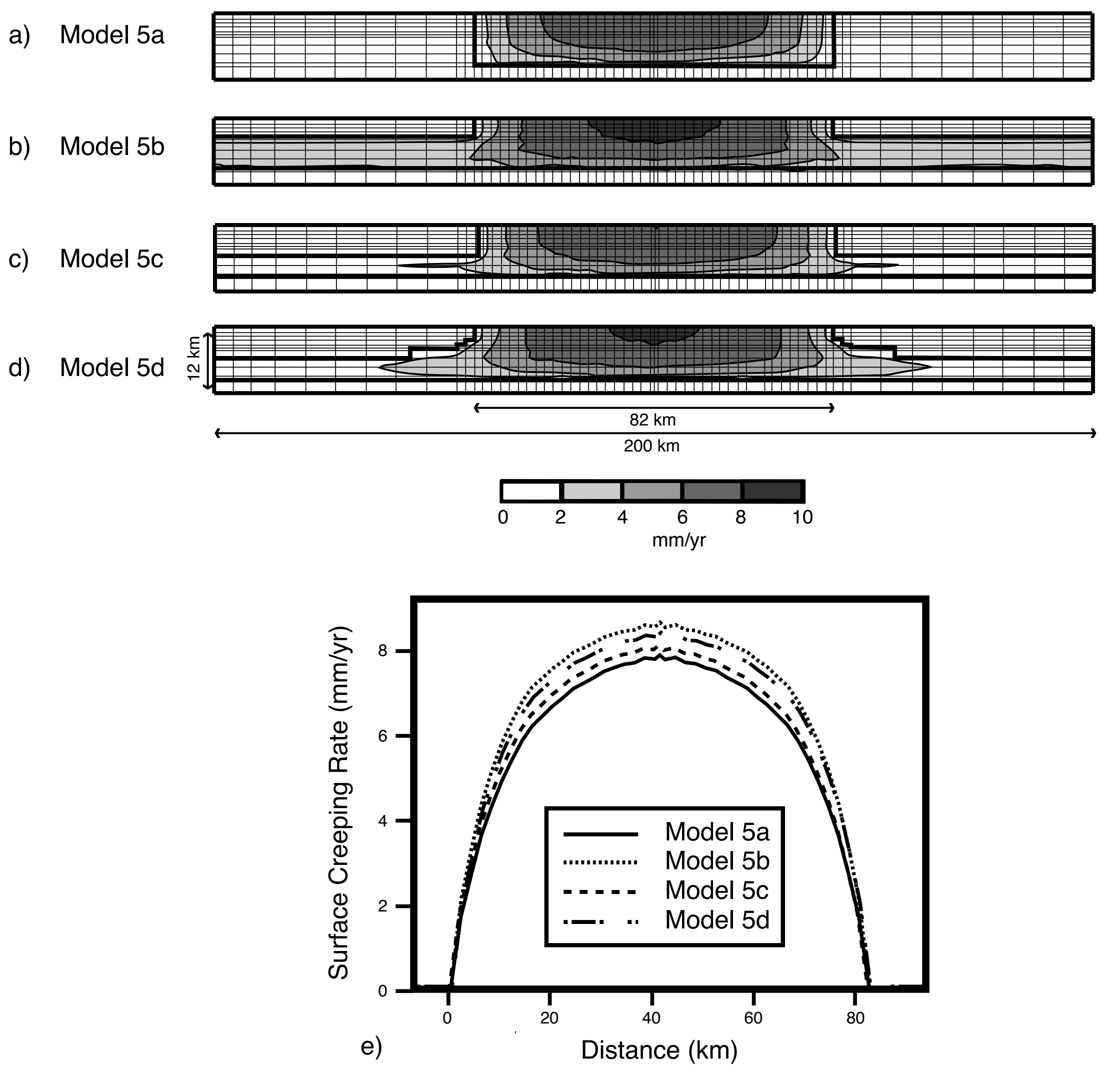

6 km (the shortest separation length tested) the two “creepable” areas behave as two independent, 40 km long faults.

3.3.5 Locked Patch Geometry

Locked areas influence creep at the surface in a complex way. To analyze this, we tested the effects of simple locking geometries (Figure 3.6). In Model 6a the right half of the fault is locked below 4 km and the left half is allowed to creep throughout the seismogenic zone. The surface creep rate decreased from ~ 5 mm/yr. over the left section to 3 mm/yr. in the right section. A gradient in the surface creep rate trends from the fully creeping zone to the region locked at a shallower depth. Because of this relatively smooth transition, in spite of the step discontinuity in fault zone geometry, one can not assume that there is a one-to-one correlation between the relative magnitude of creep at the surface and the depth extent of creep on the fault at any specific location.

In Model 6b, the fault has varying locking depths of 6 km and 12 km. The curve for this model is comparable with the results for a fault completely locked below 6 km (Figure 3.6, Model 4c). The effect of the smooth surface creep rate transition between step discontinuities in locked/creepable areas already shown in Model 6a helps explain the lack of peaks in the SCR curve of Model 6b. The “creepable” section in the middle of Model 6b is too narrow to allow a significant amount of creep, further contributing to a low variability surface creep rate curve.

Figure 3.6: Models 6a - 6b. Models contain an 82 km fault with varying patterns of locking depth. Model 6a: Creep extends from 0 km to 12 km for the left half of the fault (0-41 km), and from 0 km to 4 km for the right half (41-82 km). Model 6b: Two locked zones 15 km in width extend from 6 km to 12 km in depth. The zones are separated in the middle of the fault with a 10 km wide zone “creepable” to 12 km depth. Model 4c is shown for comparison, to demonstrate the similar behavior of Models 4c and 6b. Figure 6d: Surface creeping rate as a function of position for Models 6a, 6b, and 4c. A gradient exists in the surface creep rate from the fully creeping zone to the partially locked zone (Model 6a). Models 6b and 4c behave in a similar fashion, implying that the locked zones of Model 6b have an effect similar on surface creep to locking the entire fault from 6 km to 12 km depth.

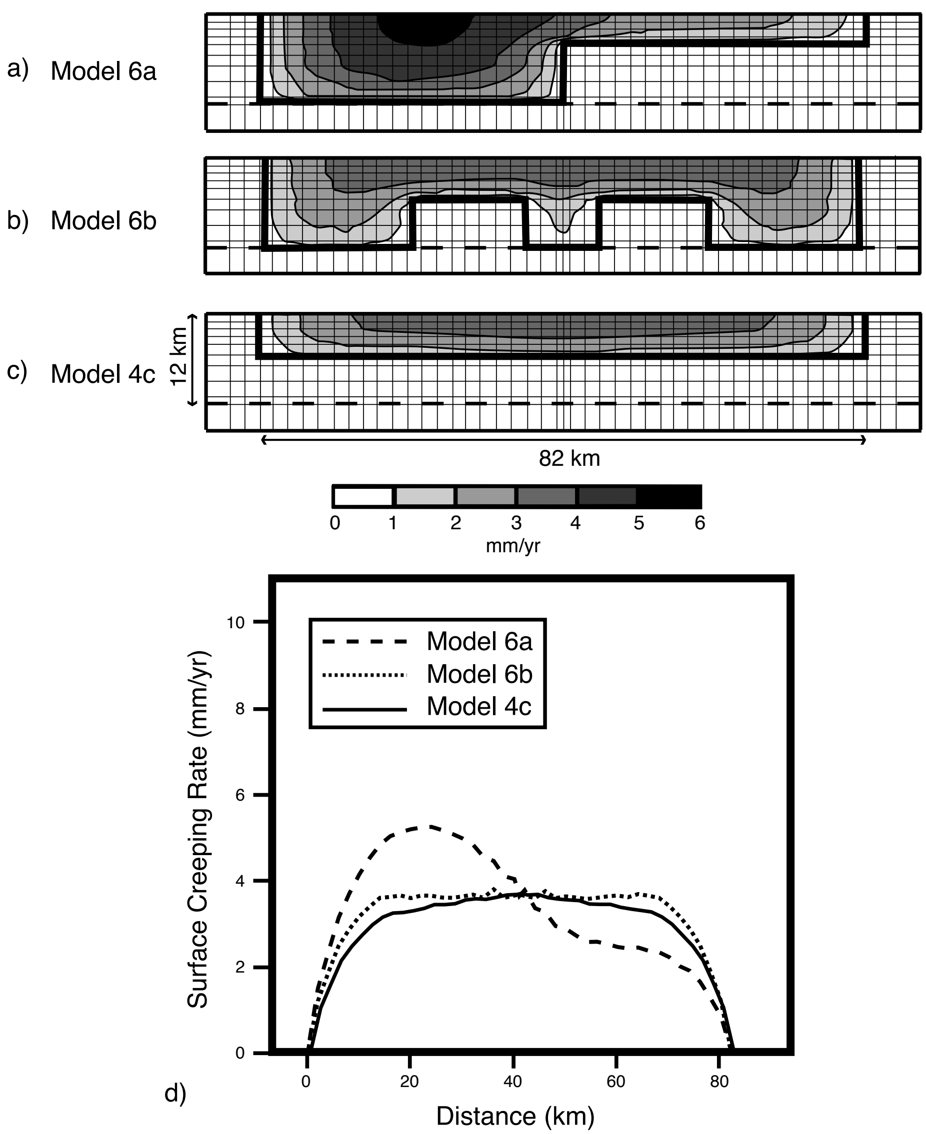

3.4 THE HAYWARD FAULT

As discussed in the introduction, previous authors have modeled the observed creep along the Hayward fault in terms of patterns of creep on the fault plane reaching different interpretations in spite of reasonable similar fits to the surficial creep. Here we apply our modeling approach to analyze the Hayward fault creeping behavior. Table 3.4 describes the Models in this section.

Table 3.4: Hayward Fault Models

	Model Description
Model 7a-B1	Best-fit model from Bürgmann et al. [2000]
Model 7b-S1	model 1 from Simpson et al. [2001]
Model 7c-HN	10 km wide locked zone, (4 - 12 km)
Model 7d-HW	18 km wide locked zone, 4km (7 -12 km) and 14 km (4 -12 km)
All faults are 82 km long, with a 12 km thick elastic layer and a 58 km thick viscoelastic layer. The viscosity is 10^{18} Pa·s in the shear zone and 10^{21} Pa·s in the viscoelastic layer.	

The observed creep data shown in Figure 3.7 are those used by Lienkaemper et al. [2001] They are comprised of decades worth of alignment arrays, offset cultural features, and creepmeters. These data are shown as points with error bars in Figure 3.7, along with the model results. The observed rates show two characteristic peaks: the northern and southern ends of the Hayward fault creep faster than the middle section. Models of Bürgmann et al. [2000] and Simpson et al. [2001] have attempted to match this observed "middle dip" in creep rates. Likewise, in our models, we focus on the northern and middle portions of the Hayward fault, including the fall of MSCRs from the northern end

Figure 3.7: Models 7a-B1 (Bürgmann et al.[2000]), 7b-S1(Simpson et al.[2001]), 7c-HN (Hayward Narrow), and 7d-HW (Hayward Wide). In all models the fault is 82 km long with varying locking depths. Figure 7a: Model 7a-B1: The distribution of "creepable" elements on the fault is varied to match the fault geometry of Bürgmann et al. [2000]. Figure 7b: Model 7b-S1: "Creepable" elements on the fault are varied to fit the fault geometry of Simpson et al. [2001]. Figure 7c: Model 7c-HN: A 10km wide locked zone extends from 4 km to 12 km depth. Figure 7d: Model 7d-HW: An 18 km wide locked zone with the geometry shown in the figure. Figure 7e: Surface creeping rate as a function of distance for Models 7a-B1, 7b-S1, 7c-HN, and 7d-HW. Models 7a-B1 and 7b-S1, based on fault geometries of previous studies, do not reproduce the pattern of the observed surface creep rates; there is a "flattening" of the curve. The models behave similarly to ones with a fixed locking zone at a depth of ~ 6 km (cf. Model 4c, Figure 4c). Models 7c-HN and 7d-HW are acceptable matches to the observed data; both reproduce the decrease in creep rate from the northern end to the middle of the fault. Data from Lienkaemper et al. (2001).

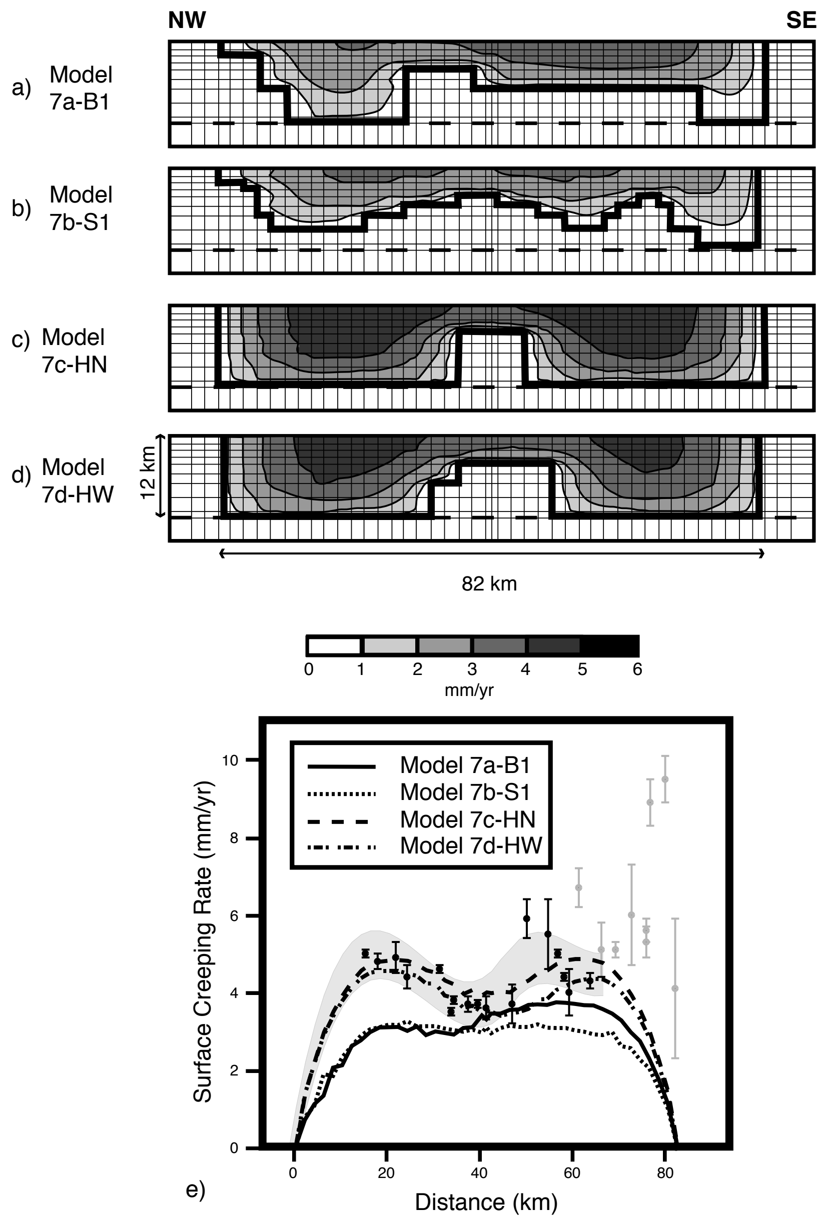

to the middle of the fault. As in the previous studies, we do not attempt to model the very high rates (~9 mm/yr.) at the southern end of the Hayward fault [Lienkaemper et al., 2001; Bürgmann et al., 2000]. The smooth variation of surface creep in response to changing fault behavior at depth does not allow unambiguous modeling of this behavior. The southern region of the Hayward fault and its interactions with the surrounding faults (i.e. Calveras and Mission) increase the complexity of the system with respect to the geometry of our model. Furthermore this part of the fault seems to be highly influenced by the Loma Prieta earthquake. While the high velocities were observed prior of the earthquake, they were significantly reduced and reversed as an effect of that event [Lienkaemper et al., 1997; Bürgmann et al., 1998].

We have first tested whether the model geometries from the previous studies produce the observed SCRs under the conditions of our model. Applying our model to the “creepable” fault geometries consistent with Bürgmann's model (our Model 7a-B1) and Simpson's model (our Model 7b-S1), we do not match the observed creep rates (Figures 3.7a, 3.7b, and 3.7e). Surface creep patterns are significantly smoothed as compared with the geometry of “creepable” patches on the fault. That is, the SCRs do not vary significantly along the fault, and we do not generate the two peaks in the SCRs as produced by previous models. These significant differences are a result of the different rheologies and boundary conditions among the models.

Bürgmann's model focused on the differences in creep rates at the northern and middle sections, i.e. higher creep rates in the northern 20 km of the Hayward fault equates to having creep to the bottom of the seismogenic zone in their model. Our results, however, show no significant difference in SCR arising from Bürgmann et al.'s geometry. In fact, our Model 7a-B1 shows slightly higher rates at the southern two-thirds of the fault compared with the northern third, i.e. the opposite of Bürgmann's model. This apparent contradiction in creep rates is explained by the influence of fault length on creep rate results. Although the northern third of the fault extends to the viscoelastic layer, it is relatively short compared with the southern two-thirds. The longer fault length in the south allows the SCR to increase in this region (cf. Figures 3.2, 3.3).

Model 1 geometry from Simpson et al. [2001] (our Model 7b-S1; Figure 3.7b,e) produces creep similar to our previously described Model 4c (Figure 3.4c). The surface creep behaves as if the entire lower surface is locked below a depth of ~ 6 km. Varying the size and shape of the locked patches at the fine scale of Simpson et al.'s model produces only minor changes in the distribution of creep at the surface.

In our modeling, we use a far-field velocity of 30 mm/yr. Increasing this velocity correspondingly scales the results. Thus it is possible to scale Models 7a-B1 and 7b-S1 to fall within the observed SCRs. However, the spatial pattern of the two peaks in the observations is still not produced; the curve retains its "flatness". One explanation for the differences among the model results may lie in the higher stresses at the bottom of the creeping fault in the Bürgmann et al. [2000] and Simpson et al. [2001] models due to the loading of the base of the fault by discrete dislocations immediately below the Hayward fault, as compared with the effects of our distributed 20-km-wide shear zone. This likely produces the smoother creep profiles in the models using our modeling approach, compared to those in prior studies.

Because the previously proposed model geometries, when analyzed with our modeling approach, do not produce the pattern in SCR observed along the Hayward fault, different geometries were tested to obtain a reasonable fit to the observations. It is possible to match observed surface creep rates using several creepable-fault geometries, two of which are shown in Figures 3.7c and 3.7d. These 'best-fits' (Models 7c-HN and 7d-HW) are obtained with a relatively narrow locked portion in the center of the fault below ~ 4 km, with the two ends "creepable" to depth. These models differ with respect to Models 7a-B1 and 7b-S1, in that the locked portion of the seismogenic layer in the middle of the fault zone is relatively narrow. Because this locked zone does not extend along a significant fraction of the entire fault plane, the smoothing effect of the SCR as seen in Models 7a-B1 and 7b-S1 does not occur. The locked area has the effect of pulling down the creep rates along the middle part of the fault without decoupling the faster creeping fault segments.

3.5 DISCUSSION

Determining the patterns of creep on a fault surface is an important component of assessing the potential size and rupture pattern of earthquakes along major fault strands. As shown here, different approaches to modeling the distribution of creep on the fault lead to significantly different patterns of inferred creep on the fault plane. Thus different model approaches can imply different patterns of slip deficit to be recovered during seismic events, suggesting different results for the seismic risk analysis. In comparing our modeling results with those of the Simpson et al. [2001] and the Bürgmann et al. [2000] studies we find some differences that are significant and need to be resolved as we improve our understanding of the Hayward fault seismic potential.

Although all the modeling approaches reasonably fit the observed data (Figure 3.8), when we analyze the locked patch geometries of Simpson et al. (2001) and Bürgmann et al. (2000) with our model we do not reproduce the pattern of creeping at the surface. Nevertheless, in comparing Simpson et al. [2001] results with our model 7c-HN (Figures 3.9a,b) we observe that the pattern of creep on the fault plane produced by the two models is reasonably similar. Thus the magnitude and pattern of slip deficit on the fault inferred from both models is comparable. It is interesting to note that in these models, the accumulation of slip deficit in the northern and southern part of the Hayward fault is comparable. If correct, this has implications for earthquake hazards in the Bay area. The occurrence of the 1868 event released part of the slip deficit on the southern part of the Hayward fault; the lack of a large seismic event on the northern segment combined with

Figure 3.8: Comparison between the observed geodetic data (adapted from Lienkaemper et al., 2001) and the results of our and previous models. The surface creep rate computed by our best fit model (thick black line) fit the observed geodetic data equally well to the results of Simpson et al. (thick gray line) and Bürgmann et al. (thick light gray line). The slightly faster creep rate in the northern section in Bürgman et al.'s model is partially due to their use of a data set with faster creep in that region which are not present in the data of Lienkaemper et al. (2001). The creeping patch geometry used by the two previous studies modeled with our approach (dashed lines) give results that do not reproduce the observed surface creeping pattern.

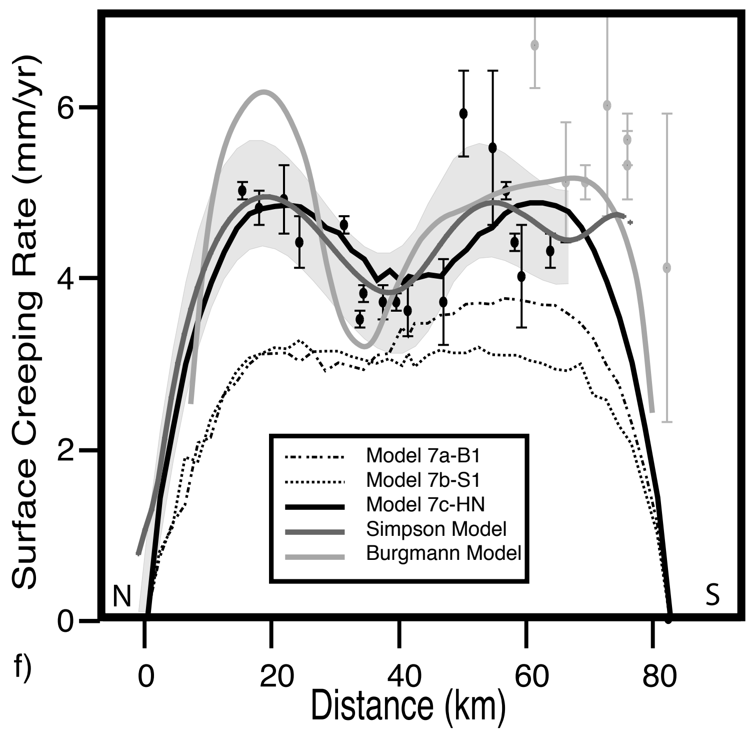

Figure 3.9: Comparison of fault plane creeping patterns for different modeling approches. Figure 9a: Model fit with the observed surficial geodetic data using approach of this paper. This figure corresponds to Figure 7c. In order to facilitate the comparison between our models and the results from Simpson et al. and Bürgmann et al.we utilized a courser color scale than in the previous figure. Figure 9b: Best fit model 1 result adapted from the paper of Simpson et al. (2001). Figure 9c: Creeping pattern resulting from our model for a locked geometry comparable with the one from Simpson et al. paper. Figure 9d: Best fit model adapted from the paper of Bürgmann et al. (2000). Figure 9e: Results for our model utilizing the “creepable” fault geometry inferred by Bürgmann et al. The results for Simpson et al. (Figure 9b) and Bürgman et al. (Figure 9d), show the creep on the upper 12 km (seismogenic layer) of the fault plane. Below this depth the fault plane has an imposed differential slip comparable with the long term displacement. Figures 9a, 9c, 9e show an additional layer (shaded with oblique lines) to indicate that in our models the fault plane ends at the base of the seismogenic layer. Beneath this depth the region is undergoing viscous deformations. In all the models the area shaded with edges indicates locked patches where the fault plane is not allowed to have differential displacement. The remaining area of the fault plane is allowed to creep. Note that in our model the transition between the locked area and the fast creeping patches is smoothed by a region with very low creeping rate not present in the Simpson et al. and Bürgmann et al. models. Note that the overall shape and amount of creep inferred by our study (gray blob in Figure 9a) is similar to the best fit results of Simpson et al. (Figure 9b) indicating a similar slip deficit. Note the different color scale respect to the previous figures.

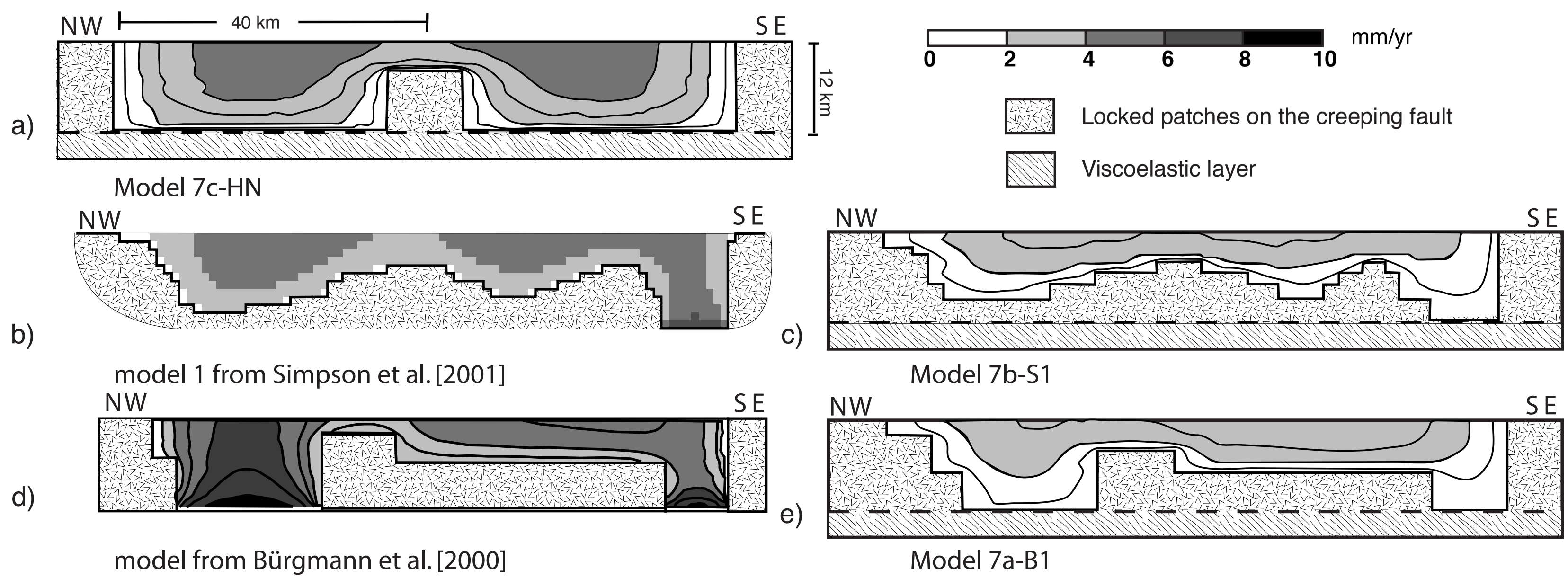

the similar accumulation of slip deficit on both fault segments led to a higher risk for the northern segment with respect to the southern one.

Patterns of creep and slip deficit on the faults differ substantially between the model presented by Bürgmann et al. [2000] and our models (Figures 3.9a,d). Their modeling constrained the slip below the seismogenic layer (at 12 km depth) to be at the long-term rate of 9 mm/yr , localized below the fault. This produces the very high creep rates at the base of the faults as seen in Figure 3.9d, and significantly changes the distribution of creep on the fault as compared with our model results. Whether such a condition of rapid localized slip is possible at the base of the seismogenic layer is not clear, but for it to exist requires a reasonably complex pattern of coupling between the elastic (seismogenic) upper crust and the lower crust and mantle beneath the fault. By including the region below the seismogenic layer in our models, we have tried to minimize this problem by allowing the system to adjust to the pattern of deformation compatible with the far-field boundary conditions and the assumed rheologic model.

These differences in patterns of creep obtained by the various modeling studies point out the importance of interpreting model results in light of the model assumptions and boundary conditions. The creep pattern inferred by the models can be substantially affected by the different assumptions made in the implementation of the strain localization below the creeping fault. At present we cannot determine the details of strain localization within the ductile layer beneath the seismogenic zone. It is possible that high resolution studies of deformation away from the creeping faults such as is possible through InSAR and similar techniques may provide some constraints on the coupling at the base of the seismogenic faults.

There are also significant differences among geometry of “creepable” patches determined in the three models. The models of Simpson et al. [2001] and Bürgmann et al. [2000] show spatially abrupt variations in fault creep, as compared with the creep pattern from the geometries that produce acceptable surface creep patterns in our modeling. This is a result of the differences in model assumptions, geometry and boundary conditions, but also raises some interesting issues related to fault surface properties. In our models we specify “creepable” elements – that is ‘frictionless’ patches that can creep if other conditions are right – with the result that in the transition between the “creepable” and locked portions of the fault there are “creepable” regions that accumulate significant slip deficit. How these weak (‘frictionless’) patches will react during an earthquake is not clear. Whether they will rupture, propagate rupture, and generate seismic moment similarly to locked fault segments with similar slip deficit or if their lack of intrinsic resistance to shear will lead to different rupture character is an important question to be resolved.

3.6 CONCLUSIONS

The creep rate at the surface is influenced by local as well as by regional parameters. Since local parameters such as the dimension of the “creepable” area (fault length and depth of the creeping section) or the geometry of the “creepable” area influence the surface creeping behavior of a fault, it is reasonable to utilize geodetic observations to infer the creep on the fault plane. On the other hand, fault creep is also influenced by regional characteristics such as the regional stress field and the coupling with the surrounding lithosphere. Indeed, the combination of all these parameters results in a smoothing effect on the creeping behavior that does not allow one to assume a one-to-one correlation between the observed creep at the surface and the behavior on the fault plane.

In our models, the properties of the viscoelastic layer play a fundamental role in the loading characteristics of the creeping fault. For this reason, the partitioning or localization of deformation into a shear zone beneath the creeping fault significantly influences the creeping behavior of the fault.

When the results from our models are considered with respect to the Hayward fault, several conclusions can be drawn. First, the spatial resolving power of previous models [Savage and Lisowski, 1993; Bürgmann et al., 2000; Simpson et al., 2001] in defining creeping patches is not obtained with our model formulation. Further, the observed surface creep rates on the Hayward fault can be matched using several different geometries. A characteristic of all acceptable models is a narrow, locked zone near the middle of the fault. Since, based on our results and the comparison of our results with previous models, the geometry of the creeping fault below the surface is not uniquely determined using surface creep rates, making robust estimates of seismic potential along creeping segments of faults is still problematic.

3.7 REFERNCES

Ambraseys, N.N. (1970), Some characteristic features of the Anatolian fault zone, Tectonophysics, 9, 143-165.

Argus D.F., R. G. Gordon, Present day motion across the Coast Ranges and San Andreas Fault system in Central California, *Geol. Soc. Amer. Bull*., 113, 1580-1592, 2001.

Aytun, A. (1980). Creep measurements in the Ismetpasa region of the North Anatolian fault zone. *in* Isakara, A.M. and Vogel, A., eds., Multidisciplinary approach to earthquake prediction 2: Braunschweig/Wiesbaden, Friedrich Vieweg & Sohn, 279-292.

Bilham, R. and Bodin, R. (1992). Fault Zone Connectivity: Slip Rates on Faults in the San Francisco Bay Area, California. *Science* **258**, 281-284.

Bürgmann, R. Schmidt, D., Nadeau, R.M., d'Alessio, M., Fielding, E., Manaker, D., McEvilly, T.V., and Murray, M.H. (2000). Earthquake Potential Along the Northern Hayward Fault, California. *Science* **289**, 1178-1181.

DeMets, C., Gordon, R.G., Argus, D.F., Stein, S., Effect of the recent revisions to the geomagnetic reversal time scale on estimates of current plate motions, *Geophys. Res. Lett.,* 21, 2191-2194, 1994.

Dixon, T.H., Miller, M., Farina, F., Wang, H., Johnson, D., Present-day motion of the Sierra Nevada block and some tectonic implications for the Basin and Range Province, North America Cordillera, *Tectonics*, 19, 1-24, 2000.

Furlong, K.P. (1993). Thermal-rheologic evolution of the upper mantle and the development of the San Andreas fault system. *Tectonophysics* **223**, 149-164.

Furlong, K.P., Hugo, W.D., and Zandt, G. (1989). Geometry and Evolution of the San Andreas Fault Zone in Northern California. *J. Geophys. Res.* **94** (B3), 3100-3110.

Furlong, K.P. and Verdonck, D. (1993). Three-Dimensional Lithospheric Kinematics in the Loma Prieta Region, California: Implications for the Earthquake Cycle. *in* USGS Professional Paper **1550-F**, F103-F131.

Galehouse, J. (1992). Theodolite Measurements of Creep Rates on San Francisco Bay Region Faults. USGS Open File Report **92-258**, 256-261.

Govers, R. (1993). Dynamics of Lithospheric Extension: A Modeling Study. Ph.D. Thesis, University of Utrecht, *Geologica Ultraiectina* **105**, 1-240.

Govers R., P.T. Meijer (2001). On the dynamics of the Juan de Fuca Plate, *Earth and Plan. Scie. Lett.,* **189**, 115-131.

Govers R., M.J.R. Wortel, S.J.H. Buiter (2000). Surface expression of slab breack-off, results from 3D numerical models, *Geophysical Research Abstract*, EGS 25th general assembly, Nice, France,

Jennings, C.W., (1994). Fault activity map of California and adjacent areas, Geologic map number 6, Department of Conservation Division of Mines and Geology.

Lienkaemper, J., Borchart, G., and Lisowski, M. (1991). Historic Creep Rate and Potential for Seismic Slip Along the Hayward Fault, California. *J. Geophys. Res*. **96** (B11), 18,261-18,283.

Lienkaemper, J.J., Schwartz, D.P., Kelson, K.I., Lettis, W.R., Simpson, G.D., Southon, J.R., Wanket, J.A., and Williams, P.L. (1999). Timing of Paleoearthquakes on the Northern Hayward fault -- Preliminary Ecidence in El Cerrito, California. USGS Open-File Report **99-318.**

Lienkaemper, J. and Galehouse, J. (1998). New Evidence Doubles the Seismic Potential of the Hayward Fault. *Seis.Res.Lett.* **69** (6), 519-523.

Lienakemper, J.J., Galehouse, J.S., and Simpson, R.W. (2001). Long-term monitoring of creep rate along the Haywardfault and evidence for a lasting creep response to 1989 Loma Prieta earthquake. *Geophys. Res. Lett.* **28** (11), 2269-2272.

Lienakemper, J.J., Galehouse, J.S., and Simpson, R.W. (1997). Creep response of the Hayward Fault to stress changes caused by the Loma Prieta earthquake, *Science*, 276, 2014-2016.

Lisowski, M., Savage, J.C., Prescott, W.H., The velocity field along the San Andreas fault in central and southern California, *J. Geophys. Res*., 96, 8369-8389, 1991.

Malservisi, R., Furlong, K.P., and Dixon, T.H. (2001). Influence of the earthquake cycle and lithospheric rheology on the dynamics of the Eastern California shear zone. *Geophys. Res. Lett.,* **28** (14), 2731-2734.

Melosh, H.J. and Raefsky, A. (1980). The dynamical origin of subduction zone topography. *Geophys. J. R. Astr. Soc*. **60**, 333-354.

Melosh, H.J. and Williams, C.A. (1989). Mechanics of graben formation in crustal rocks: A finite element analysis. *J. Geophys. Res*. **94**, 13,961-13,973.

Savage, J.C. and Lisowski, M. (1993). Inferred depth of creep on the Hayward Fault, central California. *J. Geophys. Res.* **98**, 787-793.

Simpson, R. (2000). Watching the Hayward Fault. *Science* **289,** 1147-1148.

Simpson, R.W., Lienkaemper, J.J., and Galehouse, J.S. (2001). Variations in creep rate along the Hayward Fault, California, interpreted as changes in depth of creep. *Geophys. Res. Lett.* **28** (11), 2269-2272.

Sylvester, A.G. (1988). Strike-slip faults. *GSA Bull.* **100,** 1666-1703.

Toppozada, T.R. and Borchart, G. (1998). Re-evaluation of the 1836 "Hayward Fault" and the 1838 San Andreas Fault Earthquakes. *Bull. Seism. Soc. Am.* **88,** 140-159.

Waldhauser, F., and Ellsworth, W.L. (2000). A Double-Difference Earthquake Location Algorithm: Method and Application to the Northern Hayward Fault, California. *Bull. Seismol. Soc. Am*. **90** (6), 1353-1368.

Wessel, P., and W. H. F. Smith (1998), New improved version of Generic Mapping Tools released, EOS Trans. Amer. Geophys. U., 79 (47), 579.

CHAPTER 4

MICROSEISMICITY IN STRIKE-SLIP CREEPING FAULTS: A LESSON FROM THE HAYWARD FAULT, CALIFORNIA

ABSTRACT

Creeping segments of strike-slip faults are often characterized by high rates of micro-seismicity on or near the fault. This micro-seismicity releases only a small fraction of the slip occurring on the fault and the majority of the accumulating elastic strain is released either through aseismic creep or in rare large events. Distinguishing between creeping or non-creeping faults, and determining the resulting accumulated slip deficit is important in assessing the seismic hazard associated with a fault. Improved mapping of creep on the fault surface, are key to this assessment. Recent models of creep on the Hayward Fault constrained by observations of surface creep, reach substantially different conclusions about the distribution of slip at depth on the fault. The result of one of these models (chapter 3 of this thesis) shows that there is a smooth transition in the creep rate from locked to low friction patches of the fault. This leads to "creepable" (low friction) areas that accumulate a high slip deficit and strain as compared to similar low friction segments of the fault that creep at higher rates. A comparison of chapter 3 creep patterns (from here called model KT2) with precisely relocated micro-seismicity [Waldhouser and Ellsworth, 2002] indicates that the non-repeating earthquakes mainly occur in these transitional

zones while recurrent (repeating) earthquakes cluster in high creep-rate regions. With this observation, we can better define patterns of creep, and thus the slip deficit, on the Hayward fault. This leads to the conclusion that slip deficit accumulates at comparable rates on both the northern and southern segment of the Hayward Fault. When slip effects of the 1868 earthquake (magnitude ~6.8) of the southern segment are included, the present day accumulated slip deficit is highest for the northern segment, which has apparently not ruptured since the late 1600's.

4.1 INTRODUCTION

A characteristic of some strike-slip faults is the accommodation of part of the inter-seismic differential motion through fault creep. While most faults and fault segments remain locked between major seismic events, creeping fault segments accommodate much of the motion by slipping aseismically. Creeping faults were first identified along the San Andreas Fault in central California where cultural features were progressively offset [Steinbrugge et al., 1960]. Two major continental strike-slip fault systems have been observed to undergo significant creep along specific fault segments: the North Anatolian fault in Turkey [e.g. Ambraseys, 1970; Aytun, 1980; Sylvester, 1988], and the San Andreas fault system in California (which includes the Hayward fault, Figure 4.1) [e.g. Lienkaemper et al., 1991; Galehouse, 1992; Lienkaemper and Galehouse, 1998]. In general, faults observed to creep also generate significant numbers of small earthquakes on or near the fault [Scholz, 1992] and it is common practice to identify creeping segments as those characterized by this on-fault micro-seismicity [e.g. Scholz, 1992;

Rubin et al, 1999; Waldhauser and Ellsworth, 2002]. These small events have been interpreted to represent small frictionally locked patches that slide in an unstable way (stick-slip) surrounded by larger regions of stable sliding [e.g. Vidale et al., 1994; Nadeau et al., 1995; Sammis and Rice, 2001; Waldhauser and Ellsworth, 2002]. Although this micro-seismicity occurs at a high rate, it does not contribute significantly to total fault slip [Scholz, 1992].

4.2 HAYWARD FAULT

Because the combination of creep plus micro-seismicity does not account for the total slip on creeping faults, the remaining slip deficit is recovered through large events. In the case of the Hayward fault (Figure 4.1), the southern segment of the fault last ruptured in 1868 in a magnitude ~6.8 earthquake [Lienkaemper et al., 1999; Lienkaemper and Williams, 1999]. There is evidence that the last earthquake on the northern segment occurred between 1640 and 1776 AD [Toppozada and Borchard, 1998; Lienkaemper et al., 1999; Lienkaemper and Williams, 1999]. The occurrence of large earthquakes on the creeping fault segments, shows that such faults can accumulate significant slip deficit. If we can confidently map the pattern of creep on the Hayward fault, we can improve the estimation of earthquake risk for the various segments.

The pattern of observed surface creep along the Hayward fault [e.g. Liekaemper et al, 2000] implies a complexity of creep on the fault plane. Several studies have previously investigated possible patterns of fault creep on the Hayward fault compatible with surface

Figure 4.1 San Francisco Bay area map with Hayward fault seismicity. The map shows the location of the geographical references used in the text and the main faults of the San Andreas faults system in the region [Jennings, 1994]. The relocated seismicity from Waldhouser and Ellsworth [2002] is indicated by the small solid dots. Our study area in the vicinity of the Hayward fault is highlighted by the gray shaded box and the Hayward surface trace of the fault is marked by the thicker line. The double arrow indicates the maximum inferred length of fault rupture during the1868 earthquake. There is uncertainty in the extent of 1868 rupture north of Oakland and south of Fremont [Lienkaemper et al., 1999; Yu and Segall, 1996]. (PP Point Pinole, BK Berkeley, OA Oakland, FR Fremont, SF San Francisco)

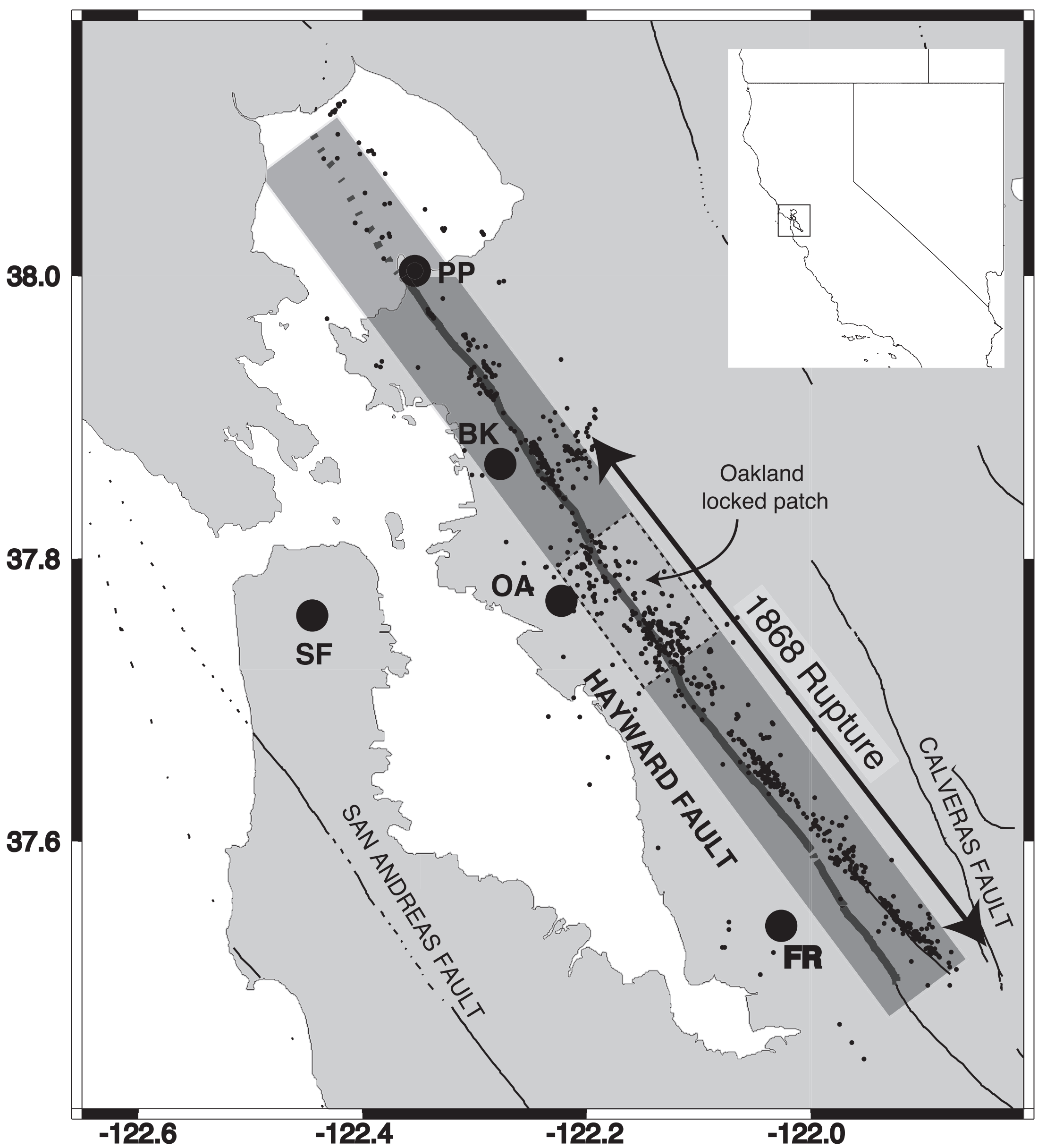

creep observations [Savage and Lisowski, 1993; Bürgmann et al., 2000; Simpson et al., 2001; Malservisi et al., 2002, chapter 3 of this thesis]. In focusing on the response of a creeping fault to different geometries of locked patches and the interaction of the fault with the surrounding lithosphere, in chapter 3, we showed that creep on the fault plane increases smoothly from locked patches to fully creeping areas (Figure 4.2). This transition produces a gradient in creep on the fault plane and thus generates strain in the crust immediately adjacent to the fault. This strain may be sufficient to generate the diffuse micro-seismicity on and adjacent to the creeping fault. With this framework, this micro-seismicity can be used to map patterns of creep on faults. The combination of high quality surface creep data [e.g. Lienkaemper et al., 2001; Bürgmann et al., 2000], studies modeling creep and slip deficit [e.g. Savage and Lisowski, 1993; Bürgmann et al., 2001; Simpson et al., 2001; Malservisi et al., 2002; Chapter 3 of this thesis], and precisely relocated micro-seismicity through the application of the double-difference approach [Waldhauser and Ellsworth, 2002], allows us to develop a new approach to map patterns of the on-fault creep.

4.3 CREEPING AND MICRO-SEISMICITY

A locked patch represents a region on the fault plane allowing no differential motion across the fault. However, since the crust surrounding the fault is a continuum, there cannot be step discontinuities in displacement (except across the fault itself). As a result, there is a transitional region from the fully locked to the free-slip region of the fault. Although the fault properties in the transitional area allow free-slip, the proximity to the

Figure 4.2 Fault creep rate and effective strain rate. **a)** Fault creep rate for the model KT2 from chapter 3. The open circles represent the relocated micro-seismicity from Waldhouser and Ellsworth [2002] (Seismicity from 1984 to 1996) projected on the fault plane. As in all the following figures we projected seismicity up to 2 km from the fault plane (gray box in figure 4.1). The dimension of the circle is scaled with the event magnitude (magnitude from 0 to 4). PP, BK, OA and FR as in figure 4.1. The arrow labeled 1868 indicates the estimated maximum extent of the 1868 rupture. **b)** effective strain rate in by the crust surrounding the fault (computed 500m from the fault plane). We use the effective strain rate (defined as $\sqrt{1/2\,\dot{e}_{ij}\,\dot{e}_{ij}}$) as a measure of the magnitude of the strain rate [Ranalli, 1992]. In this case the effective strain rate is comparable with the shear strain.

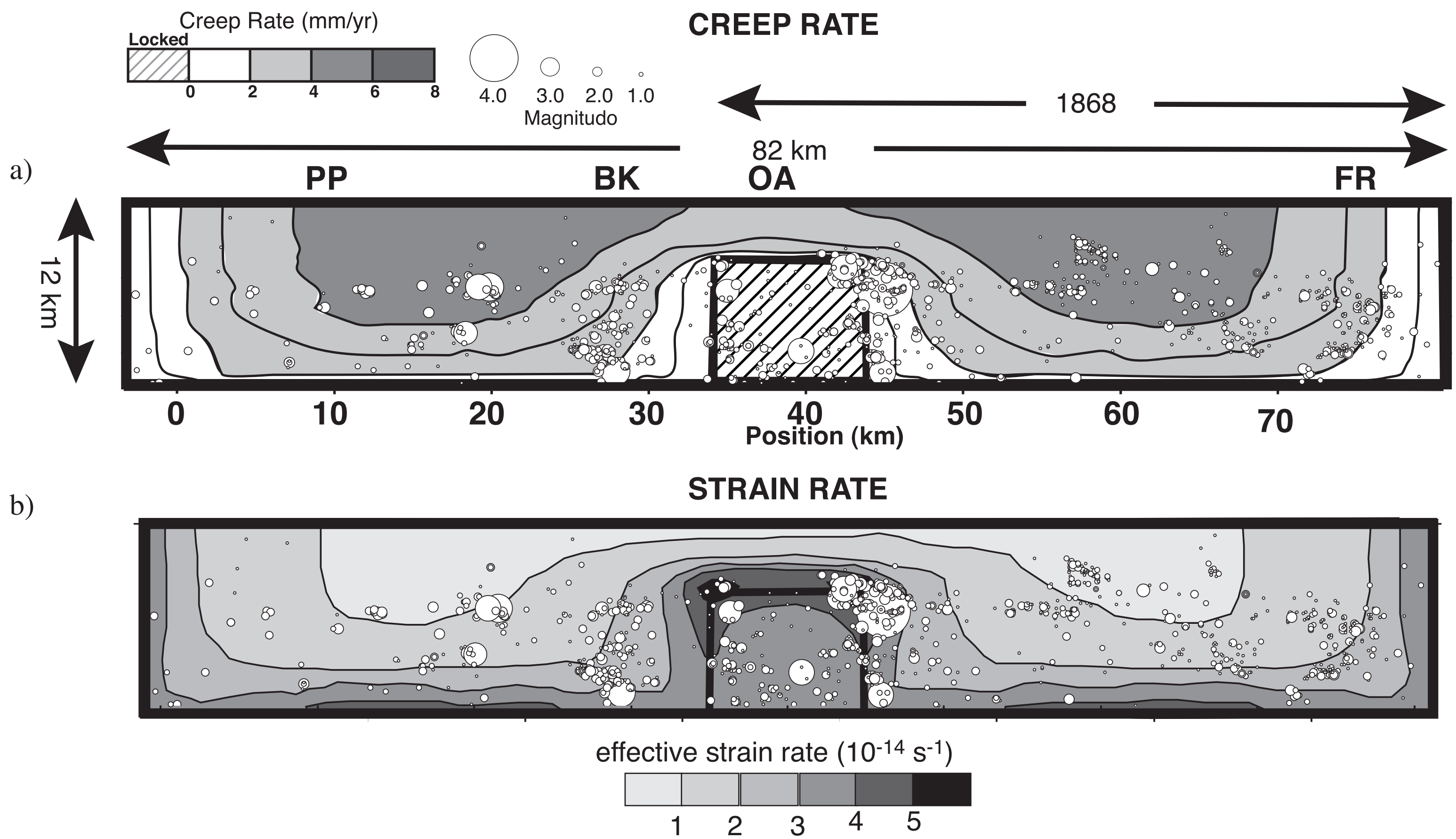

locked patch reduces the slip on the fault. These locked and transitional regions slide at a velocity slower than the surrounding creeping regions and thus accumulate strain energy at a faster rate. We propose that the micro-seismicity observed along creeping faults such as the Hayward Fault partly reflects these patterns of strain.

By combining the recent study by Waldhouser and Ellsworth [2002] of precisely relocated seismicity along the Hayward Fault with our 3-D model of the Hayward fault creep (Model KT2, chapter 3) we can begin to test the hypothesis that the deformation in the locked/free transition zone generates the observed micro-seismicity. A comparison of the relocated seismicity with the patterns of creep on the fault and the resulting strain rate in the surrounding material (Figure 4.2) indicates a clustering of events in the transitional areas with high strain rate. As indicated before, despite the low friction, the regions surrounding locked patches have a low creep rate and accumulate strain. For example, in model KT2, the maximum strain rate occurs in the region surrounding the lock area beneath Oakland (dark gray in Figure 4.2 b) and along the border of the creeping section of the fault. Plotting the relocated micro-seismicity over the strain/creep rate maps (Figure 4.2) indicated that it clusters in these high strain rate ($>1.5\ 10^{-14}\ s^{-1}$) or slow creep rate (< 2 mm/yr) regions.

We have attempted to quantify this correlation between seismicity and creep rates by categorizing the seismicity into creep and/or strain rate bins. For simplicity in this analysis, we use a sum of earthquake magnitudes. The results do not substantively differ if we use moment release or energy release as the quantitative measure of seismicity, but uncertainty in correlating the reported magnitude with either seismic moment or energy for the relatively small earthquakes of our study (magnitudes ranging from 0 to 4.0), has led us to the simple approach of using magnitudes.

Table 4.1 summarizes the percentage of cumulative magnitude released by the earthquakes in the different creep/strain categories. For model KT2, 45% of the total magnitude of the relocated earthquakes is released in the region creeping less than 2mm/yr (strain rate >1.5 10^{-14} s^{-1}), a region that corresponds to only 31% of the fault area. In contrast, only 20% of the seismicity is released in the fully creeping region (rate >4mm/yr) which corresponds to ~29% of the area. A close analysis of Figure 4.2 also shows that many of the events assigned to the locked patches are located close to the edge of those patches. This observation is in agreement with the results of Tse et al. [1985] who found that stress concentrates at the border of locked patches.

In their study, Waldhouser and Ellsworth [2002] identified a subset of earthquakes that appear to be repeated ruptures of the same small asperities (solid circles in Figure 4.3a). They referred to this subset as repeating or recurring earthquakes. It has been argued that such repeating earthquakes represent very small locked patches surrounded by free-slip regions of the fault [Vidale et al., 1994; Nadeau et al., 1995; Sammis and Rice, 2001]. In the following analysis, we consider as repeating all the events within 250 m of the events identified as repeating by Waldhouser and Ellsworth [2002]. More than 60% of the

	KT2 (Malservisi et al. [2002])				KT3 (this paper)				Simpson et al. [2001]				Burgmann et al. [2000]			
Creep Rate	% Area	% ΣMagnitude (all)	% ΣMagnitude (repeated)	% ΣMagnitude (all-repeated)	% Area	% ΣMagnitude (all)	% ΣMagnitude (repeated)	% ΣMagnitude (all-repeated)	% Area	% ΣMagnitude (all)	% ΣMagnitude (repeated)	% ΣMagnitude (all-repeated)	% Area	% ΣMagnitude (all)	% ΣMagnitude (repeated)	% ΣMagnitude (all-repeated)
Locked	10	17	13	18	11	16	18	14	43	49	17	58	42	39	25	43
0-2 mm/yr	21	26	15	29	27	26	2	35	2	3	3	3	2	1	1	1
2-4 mm/yr	40	35	7	43	42	44	27	47	25	26	34	23	21	28	25	29
4-6 mm/yr	29	22	63	10	20	14	53	4	29	22	46	16	27	22	32	19
6-8 mm/yr	0	0	0	0	0	0	0	0	1	0	0	0	8	10	17	8

% Σmagnitude (all): percentage of cumulative magnitude released by all the relocated events.

% Σmagnitude (repeated): percentage of cumulative magnitude released by the events in a radius of 250m from the events defined as repeating by Waldhouser and Ellsworth [2002]

% Σmagnitude (all-repeated): percentage of the cumulative magnitude released by the relocated events not identified as repeating and not within 250m from repeating earthquakes.

Table 4.1 Percentage of area and of total magnitude assigned to different creep-rate categories.

Figure 4.3 Comparison between non-recurrent earthquakes and KT2 model results. **a)** Relocated microseismicity along the Hayward fault (open circles). The circles are scaled according to their magnitude (see Figure 4.2). The solid circles represent the cluster of earthquakes defined as recurrent by Waldhouser and Ellsworth, 2002. In the analysis, we also considered as recurring all the earthquakes within 250 m of these events. **b)** Comparison of fault creep as evaluated in chapter 3 and non-recurrent seismicity. **c)** Comparison between off-fault strain rate from the chapter 3 model and the non-recurrent microseismicity.

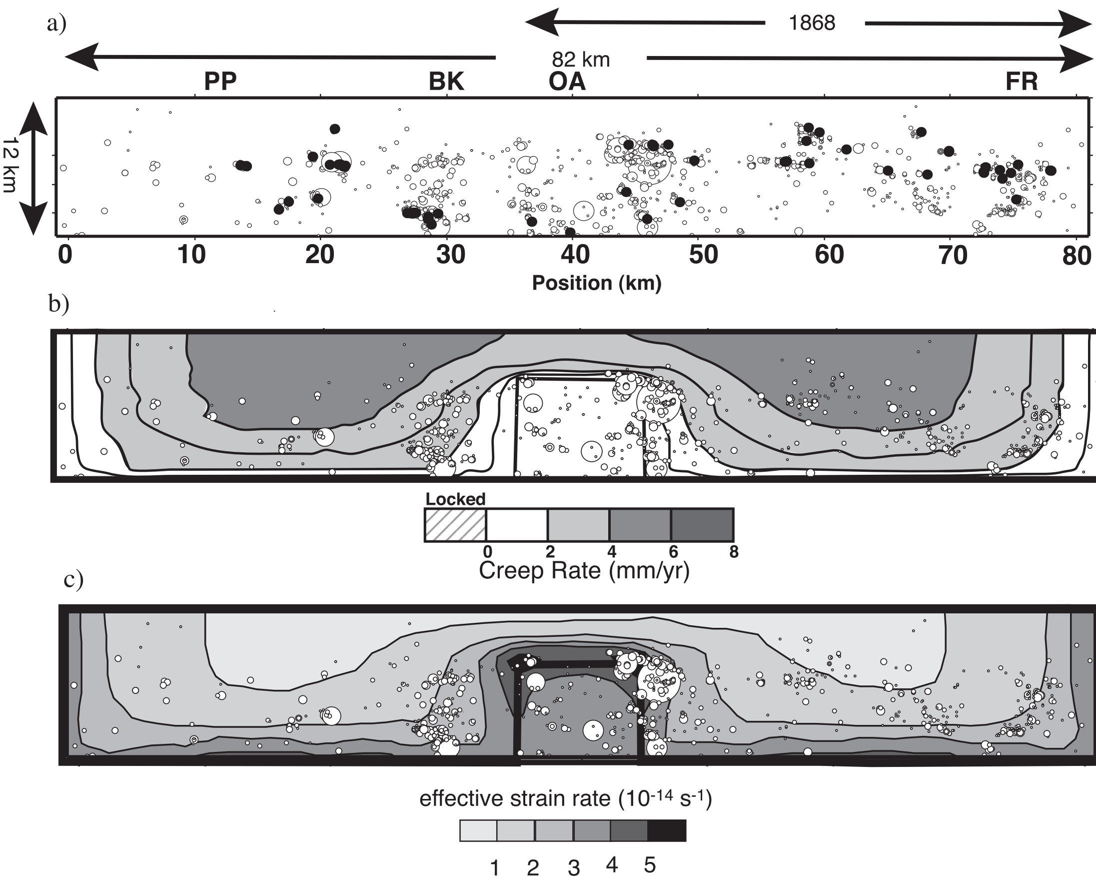

magnitude released by repeated earthquakes is in the fully creeping area. This correlation is consistent with the model that these events represent small locked patches (mini-asperity) within a free-slip region. When we remove the repeating earthquakes from the data set and repeat the above analysis of cumulative magnitude as a function of creep rate, we find that earthquakes in the fully creeping region (creep rate >4 mm/yr) release only 10% of the total magnitude while earthquakes in the high strain region (creep rate <2 mm/yr) release ~47% (Table 4.1, Figure 4.3).

We can use the observation that the micro-seismicity clusters in the transition areas as a tool to place additional constraints on patterns of locked patches and fault creep. For example, we can add a small locked patch in areas were non-repeated earthquakes cluster. The region around position 60 km (Figure 4.3) is a good candidate to test this hypothesis. In this region, a significant amount of seismic moment is released by non-repeating earthquakes that fall in the part of the fault that according to model KT2 is fully creeping. As we saw in chapter 3, adding a locked patch at depth, does not significantly alter the observable surface creep rate, thus we can try to improve the correlation between creeping rate and seismicity pattern adding a small locked patch. We find that by adding such a small locked patch, we increase the correlation between regions of high strain rate and seismicity. This improved fit to seismicity does not modify the fit to the surface creep. That is, we produce a model that improves the correlation of seismicity and creep rate on the fault and still satisfies surface creep observations. Figure 4.4 shows the results for a model with a small locked patch in the southern section of the

Figure 4.4 Fault creep and strain rate for the model with two locked patches (KT3). By adding a locked patch in the southern segment of the fault we better fit the observation that the non-repeating seismicity clusters in the transitional zones.

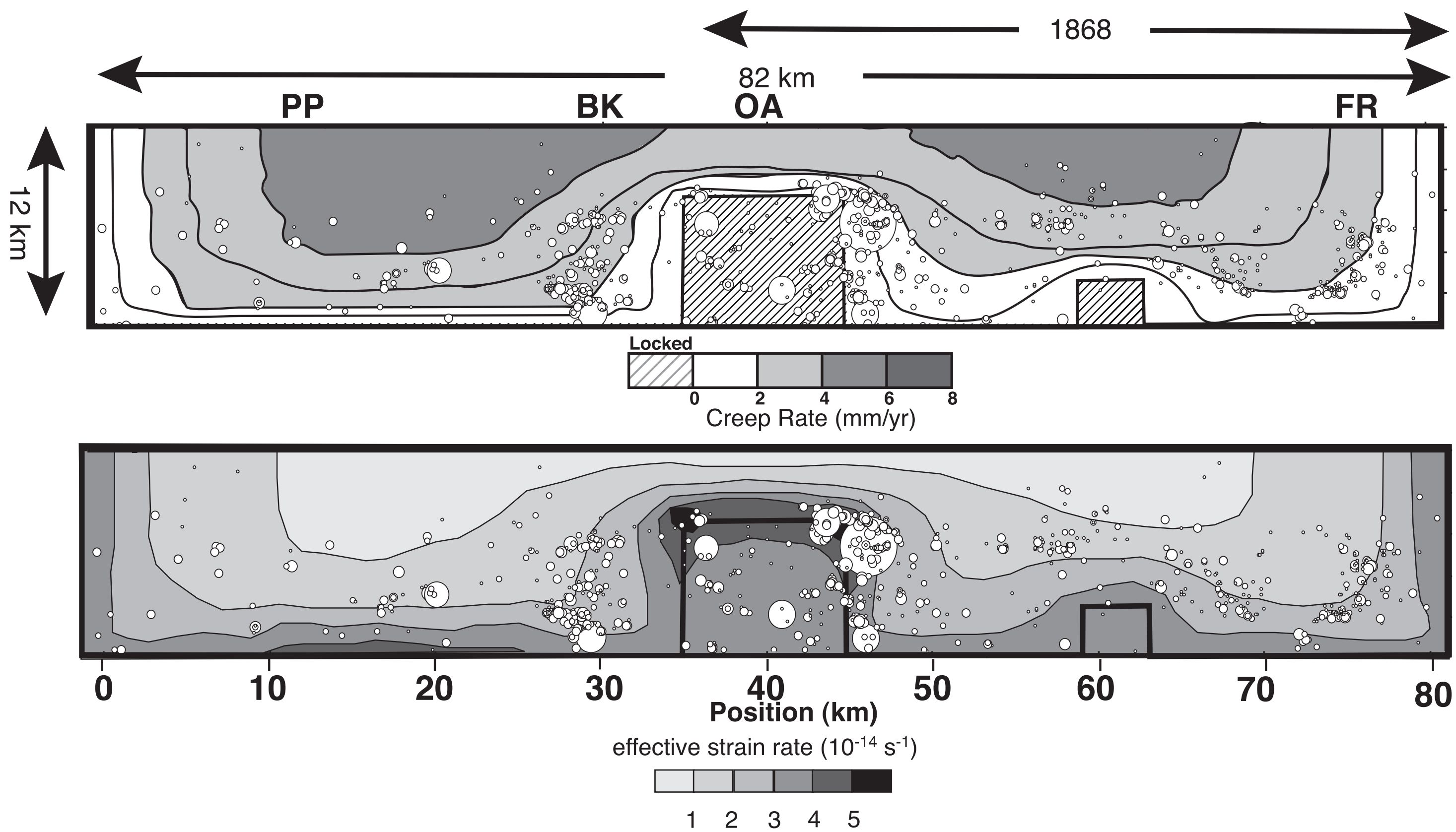

Hayward fault (Model KT3). The fully creeping area (in model KT3 corresponding to 22% of the total area) releases 14% of the total seismicity but only ~4% of the non-repeating events. By including the seismicity to help define locations of free and/or locked patches, we can explain ~95% of the seismicity as being either recurrent (repeating) in the fully creeping regions or non-recurrent in the locked/transition zones. Meanwhile if we compare the fit of the new model to the observed surface creep (Figure 4.5) we note that the model-generated surface creep pattern is not significantly changed with respect to the previous model and fits equally well the observations. In a similar way, we can further improve the fit adding small locked patches. Two examples can be the deep events at position 20km and the Berkeley region. Here, the cluster of non-repeating earthquakes suggests that the locked patch beneath Oakland is not really a simple box shape but may extend at depth further north. As this study is a first attempt to use the micro-seismicity as a further constraint in mapping locked/creeping patches on the fault, we have not extended the application to such fine spatial resolution.

4.4 DISCUSSION

Since observations of surface creep rate are not sufficient to unequivocally determine the pattern of creep on the fault, we need to introduce new observables such as the micro-seismicity or the surface strain field in the region surrounding the fault to better constrain the creep rate at depth. Precise locations for the micro-seismicity along creeping faults has the potential to be one of the tools that can better constrain the pattern of locked and creeping patches on the faults themselves. Recurrent seismicity, where earthquakes

Figure 4.5 Comparison between observed geodetics data [adapted from Lienkaemper et al., 2001] and the results of our models. The shaded area represents the best-fit for long-term surface creep rate along the Hayward fault [Lienkaemper et al., 2001]. Both the surface creep rate computed by Malservisi et al. [2002] (dashed line) and the modified model that uses seismicity as further constraint (this paper, continuous line) fit the observed data (shaded area). As with all of the previous models, we do not account for the high creep rates at the southern end of the fault That appears to be a result of interaction with the surrounding faults. The Hayward fault goes offshore at Point Pinole (PP in Figure 4.1, position 12km), for this reason the creep rate in the northermost area (0-13 km) it is not constrained.

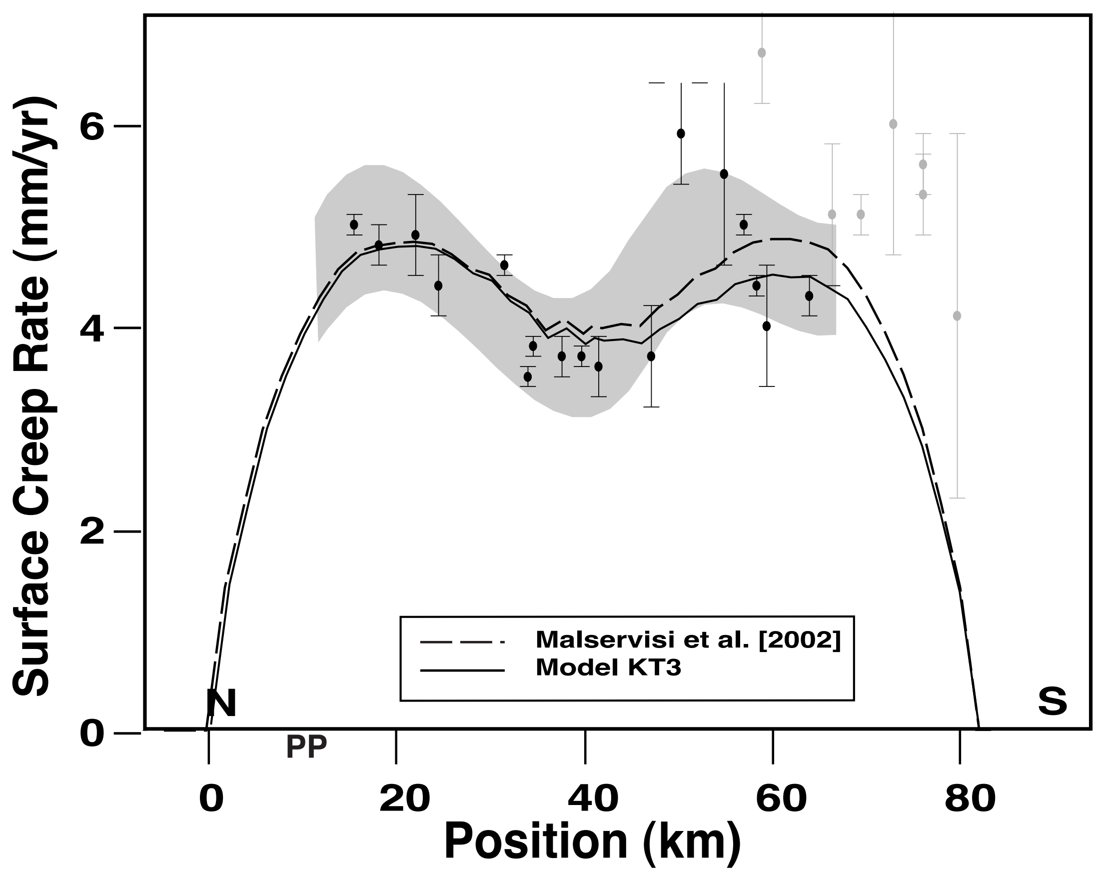

appear to be repeated ruptures of the same small asperities, predominantly occurs within the fully creeping regions, while the non-recurrent seismicity clusters in the transitional creeping zones which are regions of high strain rate. With this assumption/observation we can refine the pattern of fault creep on the Hayward Fault, as shown in the improvement from model KT2 [Malservisi et al, 2002; Chapter 3 of this thesis] to model KT3 in this chapter.

The seismic risk associated with a creeping fault is related to the amount and spatial pattern of slip deficit accumulated by the system. Unfortunately, there are some significant variations in the patterns of creep on the fault plane determined from modeling studies [Burgman et al., 2000; Simpson et al., 2001; Malservisi et al 2002; Chapter 3 of this thesis], in spite of equally good fits to the surface creep observations (Figure 4.6). Integrated over the entire Hayward Fault, all three models accumulate a comparable slip deficit (compatible with a mag. ~7 every century). However, the distribution of the regions where the seismic energy would be released is significantly different. Our modeling indicates that micro-seismicity correlates with patterns of creep strain on and near the faults. This observation can be inverted to allow us to use the pattern of micro-seismicity to potentially differentiate among the models. The models of Hayward Fault creep [Bürgmann et al., 2000; Simpson et al., 2001; Malservisi et al 2001; Chapter 3 of this thesis] show distinctly different relations between seismicity and creep (Figure 4.6). In the Bürgmann et al. model the micro-seismicity (both recurrent and non-recurrent) does not occur preferably in any creep rate region; that is, as much seismicity

Figure 4.6 Distribution of the recurrent and non-recurrent micro-seismicity with respect to the fault creep patterns of the different models. Comparison of the recurrent microseismicity (white circles), non recurrent microseismicity (black circles) and the creep rate inferred by 3 different models. a) this study (model KT3), b) Burgmann et al. [2000], and c)Simpson et al. [2001]

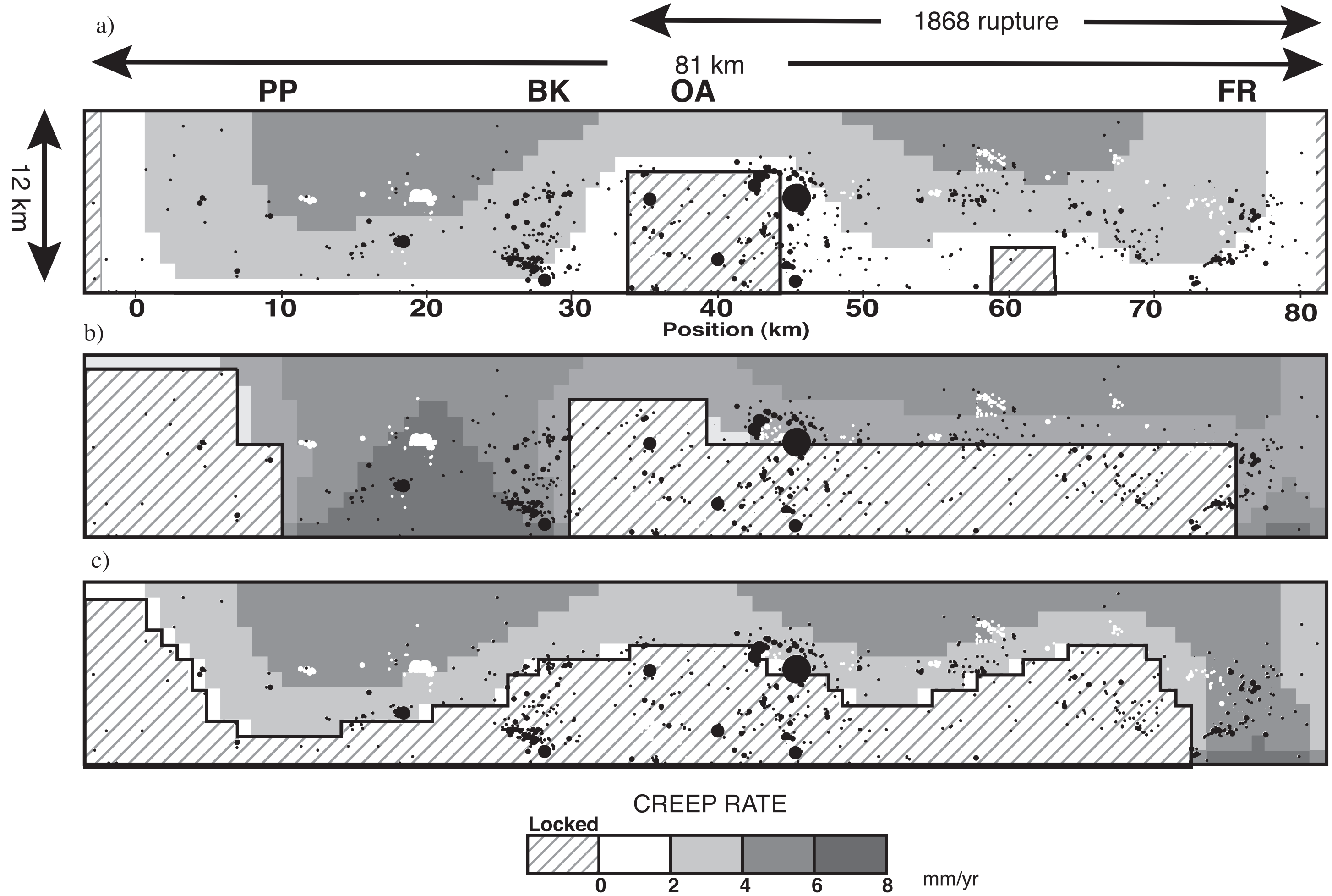

occurs in locked, as rapidly creeping regions (Table 4.1). In the Simpson et al. model, non-recurrent seismicity tends to cluster in the locked regions. Our model results show a preference for locked and transitional regions as the location of non-recurrent micro-seismicity. In both model KT3 and Simpson et al. model, the recurrent seismicity mainly corresponds to regions of high creep rate (Table 4.1). From this point of view, both the KT3 and Simpson et al. models have similar consequences. The borders of locked patches and low creep-rate regions accumulate strain generating the micro-seismicity.

The creep patterns for the three models produce significantly different distributions of slip-deficit accumulation on the fault. Assuming the present motion represents the long-term fault slip rate and extending the computed creep rate over time, we can evaluate the average slip deficit on the Hayward fault inferred from the three models. Figure 4.7a shows the resulting slip deficit averaged over the seismogenic thickness for the 9mm/yr long-term slip rate estimated for the Hayward fault [Savage and Lisowsky, 1993; Yu and Segall, 1996; Bürgmann et al., 2000]. Poorly constrained boundary conditions at the north end of the model (position 0-10 km, where the fault is offshore) and fault complexity at the southern end (position >70km, where the Hayward interacts with a complex network of faults) preclude placing significance on the slip deficit in those regions. On the southern part of the fault (position ~40-60km), all the models produce a similar vertically-averaged slip-deficit accumulation of ~7 mm/yr. The accumulated deficit increases around the locked patch beneath the Oakland region where all models predict greater slip deficit. On the northern segment (position 10-30km), the models

Figure 4.7 Hayward fault slip deficit. **a)** Vertically-averaged slip deficit rate in the seismogenic layer predicted the models by Bürgmann et al. [2000], Simpson et al. [2001], and this paper assuming a 9mm/yr long-term slip on the Hayward fault. The double-arrowed line indicates the extent of the 1868 rupture [Lienkaemper and Williams, 1999] **b)** Slip deficit accumulated on the seismogenic layer in the past 350 years assuming a constant slip deficit rate as in Figure 4.7a. We assume that 1.9m of the slip deficit accumulated in the southern segment of the fault (position >32km) was released in the 1868 earthquake (inset). The slip deficit in the transition from the northern and the southern segment is dependent on the poorly constrained extent and coseismic slip of the 1868 earthquake (question marks). The shaded area schematically shows average slip deficit inferred from the models results. The northern (position 0-13km) and the southern (position 70-82km) ends of the model are not interpreted since the surfice creep data are poorly constained or influenced by the interaction of the surrounding faults.

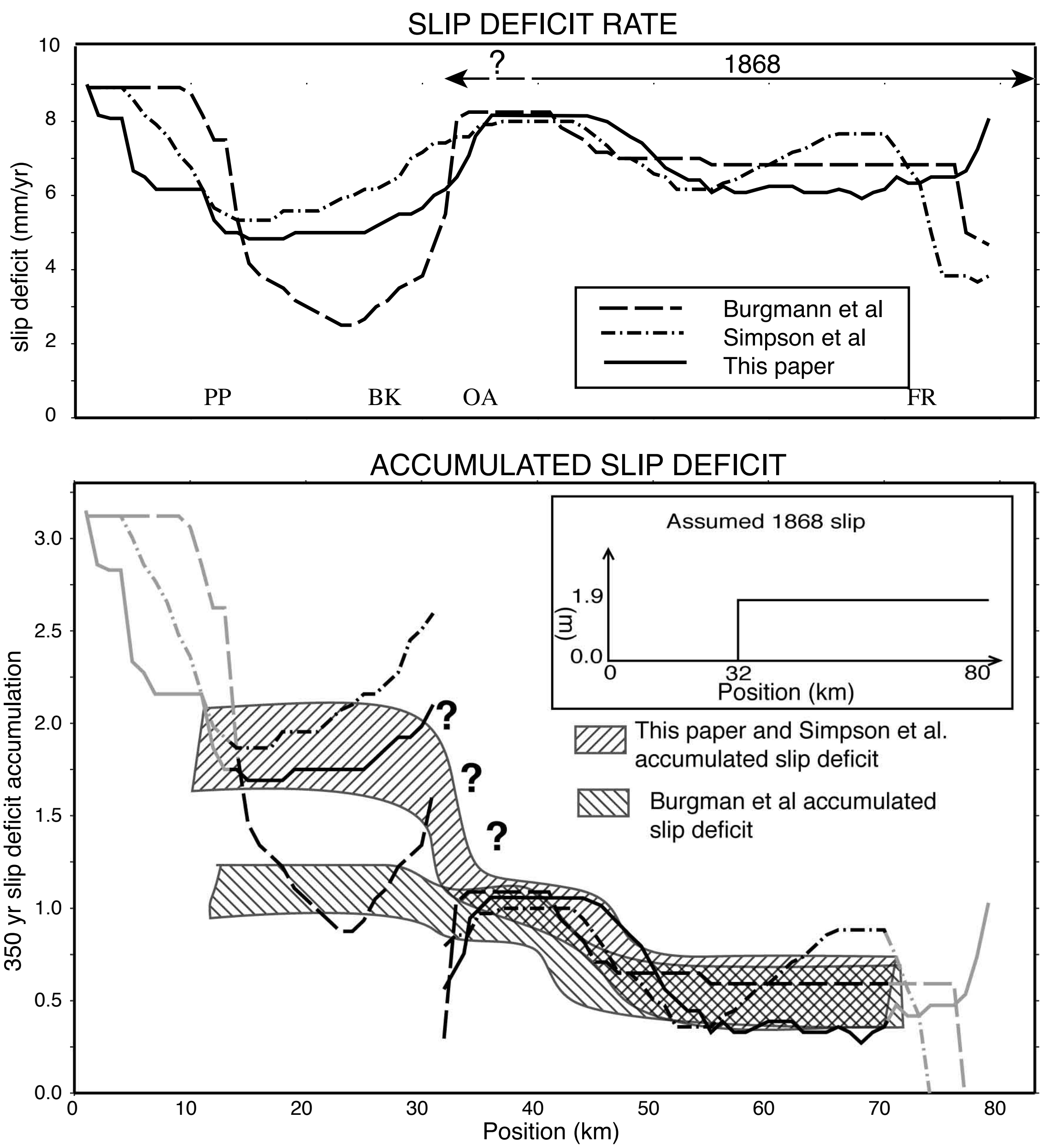

produce significantly different patterns. The high creep-rate region in the Bürgmann et al. model, results in a low accumulation rate for slip deficit (~ 3mm/yr) while the Simpson et al. model and our models (e.g. KT3) generate a similar rate of slip deficit accumulation (~6mm/yr). Integrated over the seismic cycle, these different spatial patterns and rates of slip deficit accumulation result in different amounts of moment (elastic energy) storage on the fault.

While the pattern of creep rate on the fault plays a primary role in the accumulation of slip deficit, the addition of the effects of the earthquake cycle, including the1868 earthquake and previous earthquakes, affects the pattern of the net accumulated moment on the fault. An additional complication to evaluating the pattern of accumulated slip deficit is the transient creep behavior throughout the earthquake cycle. In our determination of the slip deficit from the long-term slip rate and the present pattern of fault creep, we have implicitly assumed that the creep rate and pattern we have found for the present is constant over the time. However, it is reasonable to think that large events such as the 1868 earthquake in the southern segment or a possible 17^{th} century event for the northern segment would have large transient effects on fault creep. Additionally, much of the slip deficit accumulated over time is released in these large events. For these reasons knowing the extent of the rupture and the amount of slip during the events are crucial for estimating the current pattern of stored elastic energy accumulated on the fault. Unfortunately, neither rupture extent nor slip is well constrained for the 1868 event and virtually unconstrained for the 17^{th} century event. These uncertainties complicate any attempts at risk assessment for the region. Although the Working group on California Earthquake probabilities [1999] estimates the Hayward fault has the highest risk for a large event in the next 30 years (32% of probability for a magnitude >6.7) they also associate a low reliability to their result.

Figure 4.7b shows the deficit accumulated in a 350 yr period (a time compatible with the recurrence interval on the Hayward fault [Lienkaemper et al., 1999; Lienkaemper and Williams, 1999]) and approximately the time since the 17th century event. On the southern segment (position ~50-60 km) all the models predict a slip-deficit accumulation of ~2.5m over the period. Applying an assumed slip of ~1.9m during the 1868 event [Yu and Segall, 1996] the net deficit would be of the order of ~0.6m. On the northern segment (position ~10-30), the different rates shown in Figure 4.7a produce important differences in the slip deficit accumulated. The fast creep modeled by Bürgmann et al. [2000] produces low slip deficit of ~1m. The lower creep rates estimated by Simpson et al. [2001] and in this paper predict a significantly higher slip deficit of ~2m. With our assumption of temporally constant creep on the fault, the differences between these two estimations will increase with the time. Our modeling (and the Simpson et al. [2001] model) identify the northern segment of the fault as the region with the greatest accumulated slip deficit, while the high creep rate generated by the model of Bürgmann et al., implies for that region a low rate of slip-deficit accumulation (Figure 4.7).

The location of the northern termination of the 1868 rupture and the likely decay in slip magnitude near that terminus, also affects the earthquake cycle scenario for the fault. A shorter rupture than the one used in our analysis or a smaller coseismic slip in the Oakland area (position ~30-50km), would leave a large slip-deficit accumulation in that locked patch. The low creep-rate/locked area beneath Oakland is present in all the models. The models all predict a 350 yr slip deficit of ~3m for the Oakland region. Depending on the different 1868 rupture scenario, this deficit will have been released to different amounts leaving significantly different risk residuals. It is interesting to note that the Oakland region appears to have been involved in both the 1868 event of the southern segment and the 17th century event of the northern (?) segment [Lienkaemper and Williams, 1999]. This locked patch accumulates slip deficit faster than the surrounding areas. Furthermore, the transition from this large locked patch to freely creeping regions, induces a large strain and stress localization at its boundary. Tse et al. [1985] suggested that these regions of higher stress are responsible for the nucleation of great rupture, thus the Oakland locked patch may play some role in the rupture initiation or the termination of large events on the Hayward fault.

4.5 REFERENCES

Ambraseys, N.N., Some characteristic features of the Anatolian fault zone, *Tectonophysics*, 9, 143-165, 1970.

Aytun, A., Creep measurements in the Ismetpasa region of the North Anatolian fault zone. *in* Isakara, A.M. and Vogel, A., eds., Multidisciplinary approach to earthquake prediction 2: Braunschweig/Wiesbaden, Friedrich Vieweg & Sohn, 279-292, 1980.

Bürgmann, R. Schmidt, D., Nadeau, R.M., d'Alessio, M., Fielding, E., Manaker, D., McEvilly, T.V., and Murray, M.H., Earthquake Potential Along the Northern Hayward Fault, California. *Science,* 289, 1178-1181, 2000.

Galehouse, J., Theodolite Measurements of Creep Rates on San Francisco Bay Region Faults. *USGS Open File Report*, 92-258, 256-261, 1992.

Jennings, C.W., Fault activity map of California and adjacent areas, *Geologic Map*, 6, Department of Conservation Division of Mines and Geology, 1994.

Lienkaemper, J., Borchart, G., and Lisowski, M., Historic Creep Rate and Potential for Seismic Slip Along the Hayward Fault, California. *J. Geophys. Res.*, 96 (B11), 18,261-18,283, 1991.

Lienkaemper, J.J., Schwartz, D.P., Kelson, K.I., Lettis, W.R., Simpson, G.D., Southon, J.R., Wanket, J.A., and Williams, P.L., Timing of Paleoearthquakes on the Northern Hayward fault -- Preliminary Ecidence in El Cerrito, California, *USGS Open-File Report,* 99-318, 1999**.**

Lienkaemper, J. and Galehouse, J., New Evidence Doubles the Seismic Potential of the Hayward Fault. *Seis. Res. Lett.,* 69 (6), 519-523, 1998.

Lienkaemper, J.J., Galehouse, J.S., and Simpson, R.W., Long-term monitoring of creep rate along the Hayward fault and evidence for a lasting creep response to 1989 Loma Prieta earthquake. *Geophys. Res. Lett,*. 28 (11), 2269-2272, 2001.

Lienkaemper, J.J., P.L. Williams, Evidence for surface rupture in 1868 on the Hayward fault in north Oakland and major rupturing in prehistoric earthquakes, *Geophys. Res. Lett.*, 13, 1949-1952, 1999.

Malservisi, R., K.P. Furlong, T.H. Dixon, Influence of the earthquake cycle and lithospheric rheology on the dynamics of the Eastern California shear zone. *Geophys. Res. Lett.,* 28, 2731-2734, 2001.

Malservisi, R., C. Gans, K.P. Furlong, , Numerical modeling of creeping faults and implications for the Hayward fault, California., *submitted to Tectonophysics.*

Melosh, H.J. and Williams, C.A., Mechanics of graben formation in crustal rocks: A finite element analysis. *J. Geophys. Res.* **94**, 13,961-13,973, 1989.

Nadeau, R.M., W. Foxall, T.V. McEvilly, Clustering and periodic recurrence of micro-earthquake on the San Andreas Fault at Parkfield, California, *Science*, 267, 503-507, 1995.

Ranalli, G., Rheology of the Earth, 413 p., Chapman & Hall, London, UK, 1992.

Rubin, A.M., D. Gillard, J-L. Got, Streaks of microearthquakes along creeping faults, *Nature*, 400, 635-641, 1999.

Sammis, C.G, J. R. Rice, Repeating earthquake as low-stress-drop events at a border between locked and creeping fault patches, *Bull. Seismol. Soc Am.*, 91, 532-537, 2001.

Savage, J.C. and Lisowski, M., Inferred depth of creep on the Hayward Fault, central California. *J. Geophys. Res.,* 98, 787-793, 1993.

Scholz, C.H., The mechanics of earthquakes and faulting, Cambridge University Press, p 439, 1990.

Simpson, R.W., Lienkaemper, J.J., and Galehouse, J.S., Variations in creep rate along the Hayward Fault, California, interpreted as changes in depth of creep. *Geophys. Res. Lett.* 28 (11), 2269-2272, 2001.

Steinbrugge, K.V., E.G. Zacher, D. Tocher, C.A. Whitten, C.N. Claire, Creep on the San Andreas fault, *Bull. Seismol. Soc. Am.*, 65, 93-112, 1960.

Sylvester, A.G., Strike-slip faults. *GSA Bull.* 100, 1666-1703, 1988.

Toppozada, T.R. and Borchart, G., Re-evaluation of the 1836 "Hayward Fault" and the 1838 San Andreas Fault Earthquakes. *Bull. Seism. Soc. Am.* 88**,** 140-159, 1998.

Tse, S.T., R. Dmowska, J.R. Rice, Stressing of locked patches along a creeping fault, *Bull. Seisol. Soc Am.*, 75, 709-736, 1985.

Vidale, J.E., W.L. Ellsworth, A. Cole, C. Marone, Variation in rupture process with recurrence interval in a repeated small earthquake, *Nature*, 368, 624-626, 1994.

Waldhauser, F., L.W. Ellsworth, Fault structure and mechanics of the Hayward Fault, California, from double-difference earthquake locations, *J. Geophys. Res.*, 107, 10.1029/2000JB000084, 2002.

Working Group on California Earthquake Probabilities, Earthquake probabilities in the San Francisco Bay region: 2000-2030. A summary of findings, *U.S. Geol. Surv. Open-file rept.*, 99-517, 1999.

Yu, E., P. Segall, Slip in the 1868 Hayward earthquake from the analysis of historical triangulation data, *J. Geophys. Res.*, 101, 16101,16-118, 1996.

CHAPTER 5

DYNAMIC UPLIFT IN A TRANSPRESSIONAL REGIME: THE SUBDUCTION AREA OF FIORDLAND, NEW ZEALAND‡

ABSTRACT

The Southwest region of the South Island of New Zealand, Fiordland, is characterized by high elevation and a large positive Bouguer gravity anomaly. This combination of high topography with high Bouguer gravity argues against an isostatic equilibrium and for the need of an additional support mechanism for the elevation. Earthquakes as deep as 150 km, a deformed Benioff zone and inference from plate reconstructions, all support a tectonic model where the eastern margin of the Australian plate is subducting beneath Fiordland and is sharply bent. This bending of the Australian plate is proposed to provide the needed non-isostatic support for Fiordland topography and generates the observed gravity anomaly. Typically in subduction zones, the bending of the plate leads to an offshore uplift (peripheral bulge) with an associated positive free air gravity anomaly. In contrast, the positive gravity anomaly (Bouguer and Free Air) in Fiordland is onshore, localized close to the shoreline, and generally corresponds spatially with the high elevations. Here we propose a mechanism that allows the subducted sliver of slab to be decoupled from the main Australian plate and strongly bent beneath Fiordland to generate

---

‡ This Chapter has been submitted to EPSL as: Malservisi, R., K.P. Furlong, H. Anderson, Dynamic uplift in the subduction area of Fiordland, New Zealand, June 2002.

these observations. We use a finite element model (FEM) to test this scenario. The model allows us to study the flexural response of a subducting elastic slab when bent by lateral compression into a shape similar to one inferred from the seismicity pattern. We test how different plate geometries and plate boundary forces influence the flexural dynamic support of Fiordland topography, providing important constraints on the local plate dynamics. The model results show that for a tectonically reasonable combination of plate geometries and boundary forces, the deformation of the lithosphere produces the observed topography and gravity signature. In particular we find that the bending of the subducted Australian plate can supply the needed uplift and support for the topography of Fiordland. However, a weak area west of but nearby the Fiordland shoreline, perhaps a fault or tear, is needed to decouple the subducted sliver, confine the bulge, and localize the uplift within Fiordland.

5.1 INTRODUCTION

The Fiordland region (Figure 5.1) in the southwest corner of South Island, New Zealand, is characterized by high elevations (>1000 m) and a large positive regional Bouguer and free air gravity anomaly (>150 mgal) [Reilly and Whiteford, 1979] (Figure 5.2). Earthquakes as deep as 150 km, a deformed Benioff plane [Christoffel and Van der Linden, 1972; Reyners, 1995; Reyners et al., 2001] and plate reconstructions [Sutherland and Melhuish, 2000; Sutherland et al., 2000, Sutherland 1995], support the concept that the eastern margin of the Australian plate is subducting below Fiordland with a sharply

Figure 5.1: Topo-Bathymetry map of the southwestern corner of the South Island of New Zealand with the principal tectonic features of the region. The map includes the geographic references used in the text.

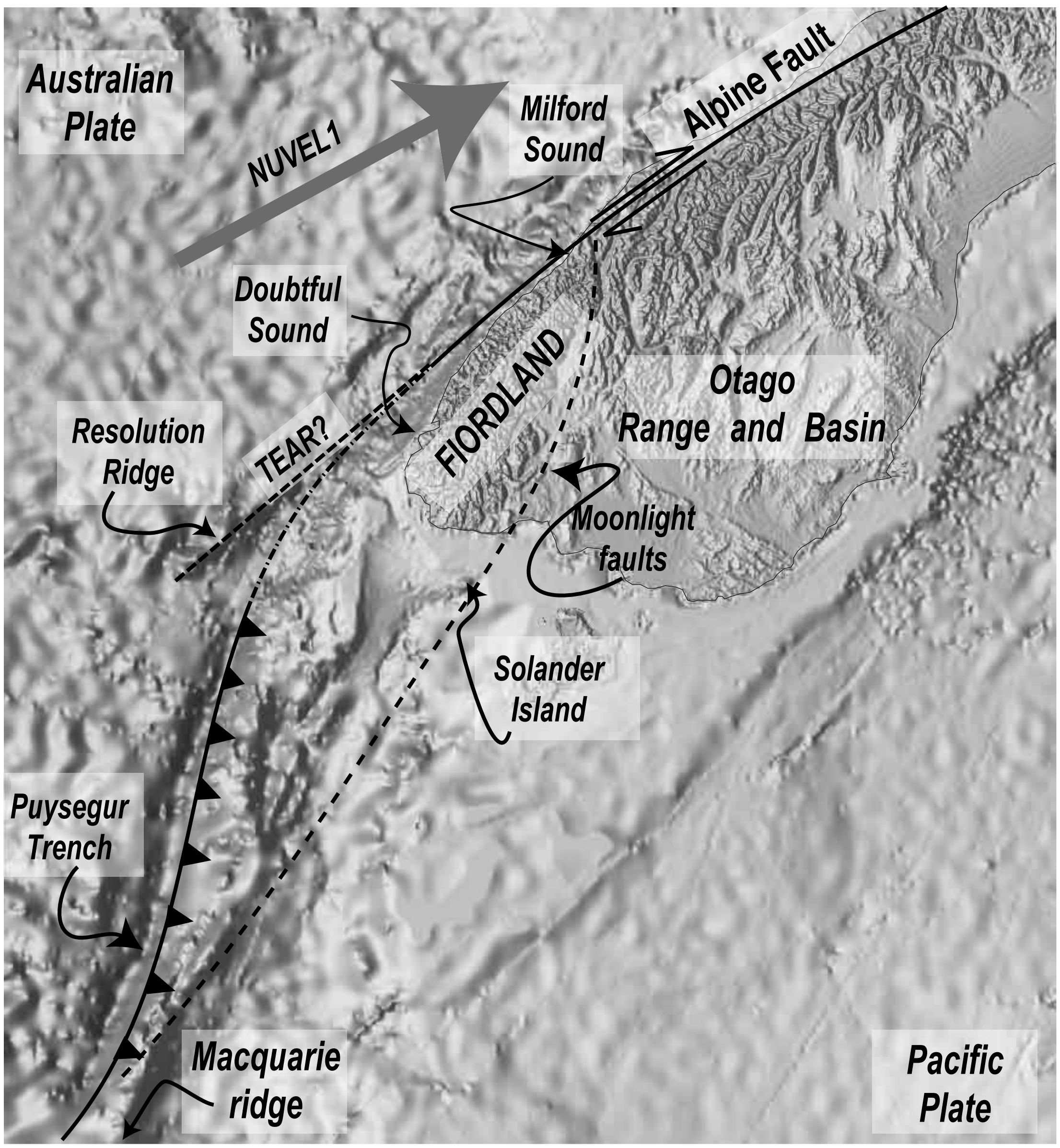

Figure 5.2: Topography and gravity anomaly for the South Island of New Zealand.
a) hillshade image of the topo-bathymetry of South island (from GTOPO30, http://edcdaac.usgs.gov/gtopo30/gtopo30.html) The box indicate the area of figure 5.1. **b)** Bouguer (inland) and Free Air (offshore) gravity anomaly of the South Island (Reilly and Whiteford, 1979). Contour every 25 mgal. **c)** Profile of gravity anomaly (black line) and topography (dashed line) across the Fiordland/Otago region (line AA' in Figure 5.2 a,b). **d)** Profile of gravity anomaly (black line) and topography (dashed line) across the Southern Alps region (line BB' in Figure 5.2 a,b).

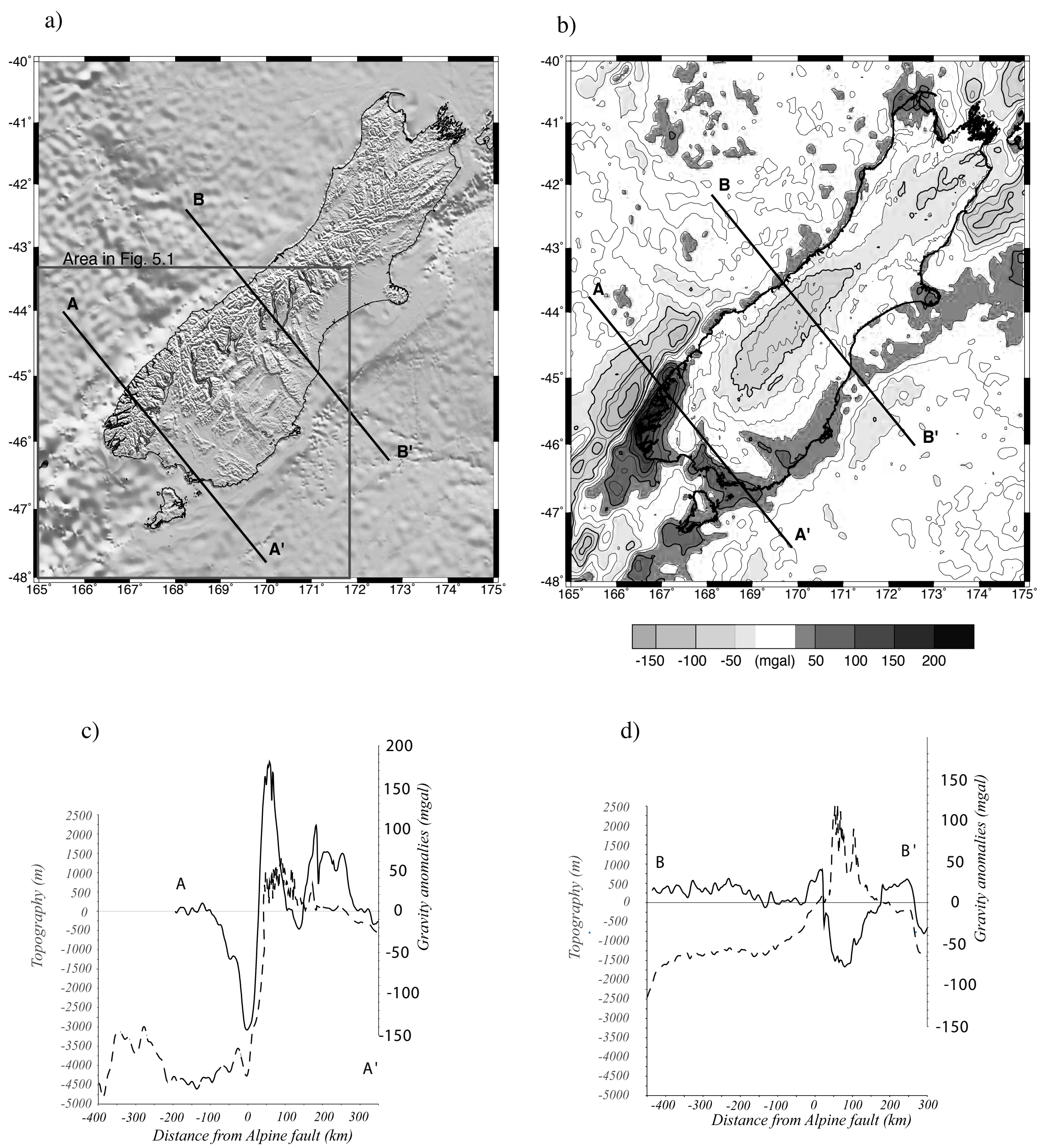

bent geometry. Typically in subduction zones, the bending of the plate leads to an offshore uplift (peripheral bulge) with an associated positive free air gravity anomaly. In contrast, the positive free air and Bouguer gravity anomaly are onshore in Fiordland and generally correspond with areas of high elevations. The occurrence of a significant positive Bouguer gravity anomaly (>150 mgal) with regions of high elevation (>1000 m) argues against simple isostatic compensation as the mechanism to support the topography (Figure 5.3). Rather we propose that there is flexural dynamic support for the elevation of Fiordland, with that support derived from the effects of the sharp bending of the subducting Australian plate.

The South Island of New Zealand straddles the Pacific/Australian plate boundary (Figure 5.1). Tectonically the area of Fiordland is characterized by the transition from a subduction regime along the Puysegur trench to a transpressive transform boundary along the Alpine Fault [Delteil et al., 1996; Sutherland, 1995; Lamarche and Lebrun, 2000] (Figure 5.1). Since ~5 Ma, migration of the Australian/Pacific Eulerian pole has produced an increasingly compressive component of relative motion along the plate boundary in the region of Fiordland and the Southern Alps [Sutherland, 1995; Sutherland and Melhuish, 2000]. Along the Alpine Fault, this increased compression has been accommodated through lithospheric thickening and the formation of the Southern Alps [e.g. Stern et al., 2000; Molnar et al., 1999; Shi and Allis, 1995]. In the area of Fiordland, because of the existence of a complex series of structures inherited from previous tectonics regimes, transpression has led to the subduction of a corner of the Australian

Figure 5.3: Implications on gravity/topography observations for mechanisms of support. **a)** A positive gravity anomaly is associated with dense material close to the surface. We assume a two-layer model with an upper layer (crust, light gray) of density ρ_c and the lower layer (mantle, dark gray) of density ρ_m. The area labeled Fiordland, corresponds to the region with a Bouguer gravity anomaly of 180 mgal with respect to a reference region labeled Otago. In order to have that gravity anomaly, the dense material (mantle) must be ~8500 m closer to the surface than in the reference region. The light layer above the mean sea level (MSL) is not included in the computation since we are computing the Bouguer anomalies. **b)** Two regions are in isostatic equilibrium if the pressure due to a column of material is equal at the compensation depth. As in (a) we analyze a two-layer model of density ρ_c and ρ_m and we assume the density of the atmosphere to be equal to zero. Computing the isostatic pressure due to the column of material, we evaluate the difference of elevation between the two regions if they are in equilibrium. In the region labeled Fiordland the denser material (mantle) is ~8500m closer to the surface with respect to the reference region (Otago). To be in isostatic equilibrium the average topography of the reference region (Otago) should be 1500m higher than the Fiordland region. In reality, the average elevation of Fiordland is higher than the adjacent Range and Basin (see Figure 5.2 c), thus its elevation is not isostatically compensated.

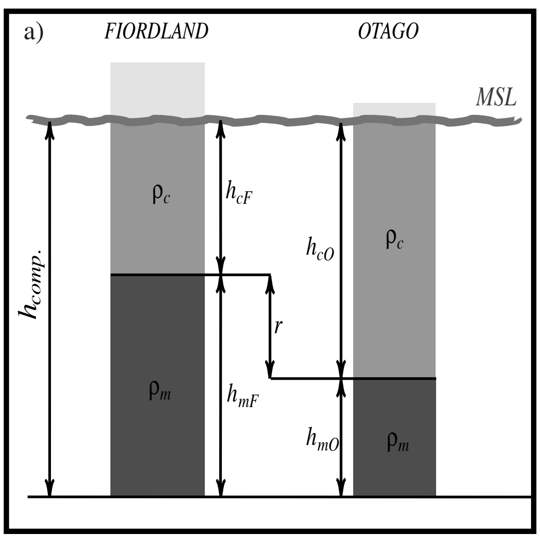

Gravity vs. Crustal Structure

$$\begin{cases} h_{cO} - h_{cF} = r \\ h_{mF} + h_{cF} = h_{comp.} \\ h_{mO} + h_{cO} = h_{comp.} \\ 2\pi G(\rho_c h_{cF} + \rho_m h_{mF}) = \Delta g + 2\pi G(\rho_c h_{cO} + \rho_m h_{mO}) \end{cases} \Rightarrow r = \frac{\Delta g}{2\pi G(\rho_m - \rho_c)}$$

$\rho_m = 3300 \, \frac{kg}{m^3}$

$\rho_c = 2800 \, \frac{kg}{m^3}$

$\Delta g = 180 \, mgal$

$$r = 8590 \ m$$

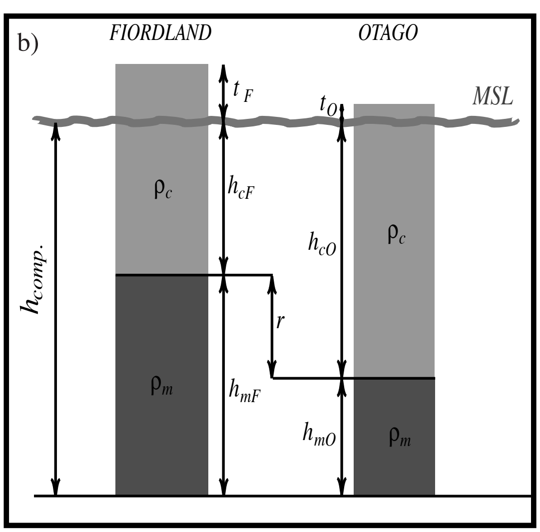

Gravity vs. Elevation (Isostasy)

$$\begin{cases} h_{cO} - h_{cF} = r \\ h_{mF} + h_{cF} = h_{comp.} \\ h_{mO} + h_{cO} = h_{comp.} \\ g\rho_c(h_{cF} + t_F) + g\rho_m h_{mF} = g\rho_c(h_{cO} + t_O) + g\rho_m h_{mO} \end{cases} \Rightarrow t_O - t_F = \frac{(\rho_m - \rho_c)\, r}{\rho_c}$$

$\rho_m = 3300 \, \frac{kg}{m^3}$

$\rho_c = 2800 \, \frac{kg}{m^3}$

$r = 8590 \, m$

$$t_F = t_O - 1534 \ m$$

plate [Sutherland, 1995; Sutherland et al., 2000] and to its localized bending [Furlong et al., 2002].

Furlong et al. [2002] suggest that the collision between the subducting Australian plate and the lithospheric root growing beneath the Southern Alps helps to initiate the bending of the slab and produces a sharp bend in the subducting slab. They argue that the flexure of the Australian plate can generate the dynamic support onshore that uplifts Fiordland to its present elevation. In this paper, we test that hypothesis. We study the response of a bent elastic slab to the deformational forces produced by the interaction of the subducted Australian lithosphere with the lithospheric root that has formed beneath the Southern Alps of New Zealand.

An additional factor that may help to localize the dynamic support beneath Fiordland is a tear in the Australian plate adjacent to Fiordland. Bathymetric and seismic analysis [Lamarche and Lebrun, 2000; Lebrun et al, 2000] in addition to a flexural-gravity analysis south of Fiordland [Lebrun et al., 1998, 2000], argue that there is a tear in the Australian plate, essentially extending the Alpine Fault south-westward. Such a tear would decouple the subducting slice of the Australian lithosphere and greatly influence the subduction geometry. Previous work in other regions has suggested that the transition from a strike-slip regime to subduction can be facilitated by the presence of a tear in the downgoing plate [e.g. Calais et al., 1992; Millen and Hamburger, 1998; Bos and Spakman, 2001]. This may be important in the Fiordland region, where the highly deformed sliver of subducting plate and the presence of weakness along the inactive Cretaceous passive margin east of the Alpine Fault-Resolution Ridge line [Sutherland et al., 2000] could serve to localize the mechanical decoupling in this weak spot. We analyze the role that such a decoupling zone, which for simplicity we refer to as a tear, can play in the dynamic support of Fiordland's high topography.

5.2 SLAB GEOMETRY

We combine the observed pattern of seismicity and focal mechanisms to define the geometry of the subducting sliver of the Australian plate beneath Fiordland. The distribution of the seismicity as recorded by the New Zealand National Seismic Network [Anderson and Webb, 1994] and a local portable network [Reyners, 1995; Reyners et al. 2002] shows a highly deformed Benioff zone. Offshore Fiordland, to the south, the Benioff plane is sub-horizontal with an increase in eastward dip moving northward. The Benioff zone is almost vertical beneath the northern part of Fiordland. At the northern end, the deep seismicity stops abruptly (in the area of Milford sound) (Figure 5.4). The pattern of seismicity defining the Benioff zone is relatively diffuse. Whether this is simply a consequence of uncertainty in location, or the seismicity actually images a broad deformation zone associated with the sharp bending of the slab is uncertain. We favor the latter explanation, as a detailed micro-earthquake study in the region with good control in relative locations, indicates a similarly diffuse pattern of seismicity [Reyners, 1995]. In order to better define the actual plate interface and its approximate geometry, we use the

Figure 5.4: Seismicity pattern (events from 1964 to 1998) from the NZNSN [Anderson and Webb, 1994] and focal mechanisms in the Fiordland region. The local seismicity has been projected onto vertical cross-section planes (b, c, d). One cross-section plane is parallel to the plate motion (5.4b) and 2 cross-section planes are perpendicular, a southern one (5.4c) and a northern one (5.4d). The shaded boxes in the map view correspond to the region mapped in the different cross-sections. The focal mechanisms on the map-view (fig 5.4 a) are a lower hemisphere projection while in the cross-sections are side projections on the plane of the cross-section. The focal mechanisms for the larger event in the area are labeled with the depth and a letter or a number corresponding respectively to the solution published by [Anderson and Webb, 1993] and [Moore et al., 2000].

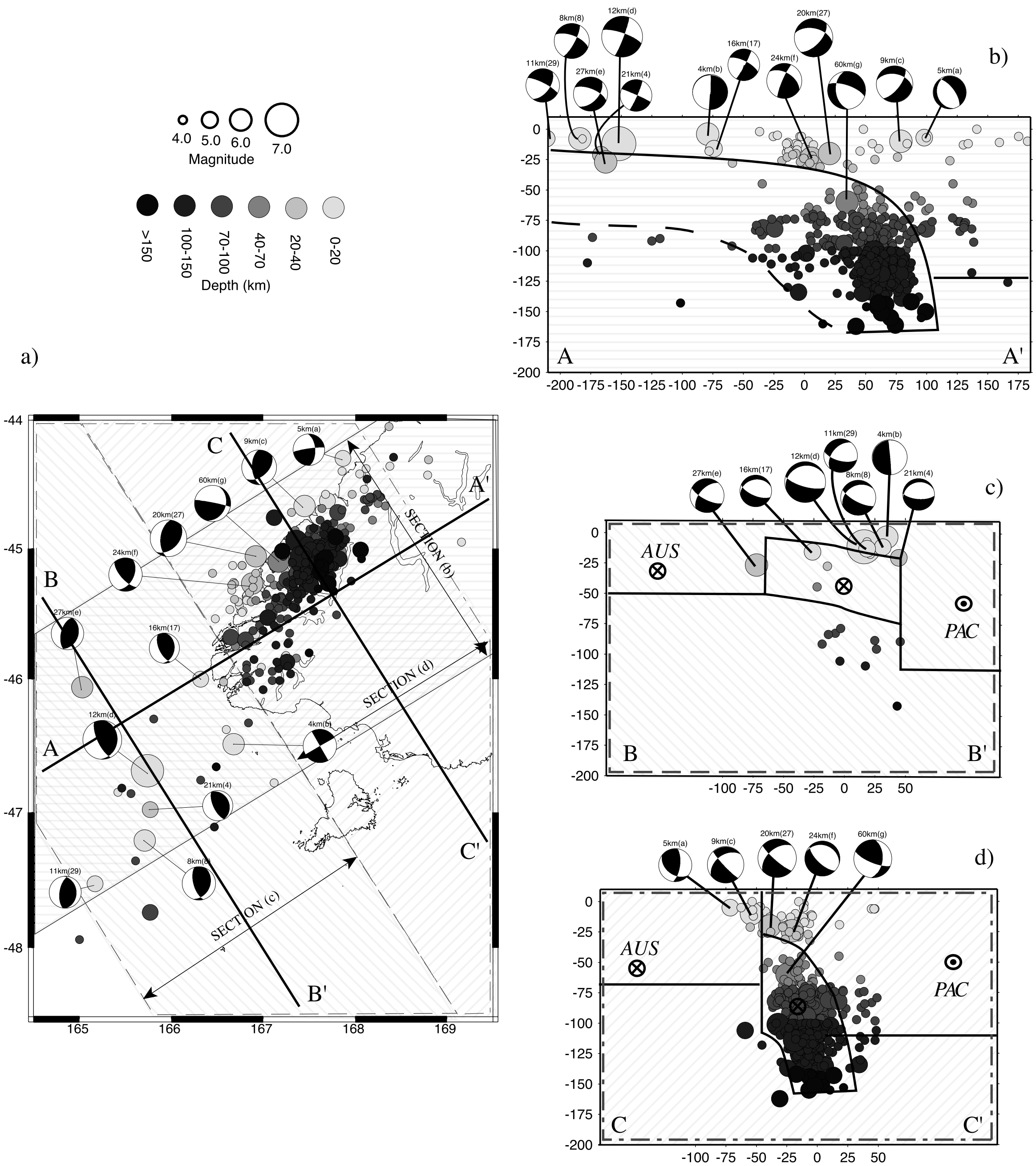

orientation of candidate slip-planes from focal mechanisms from large events in the region [Moore et al., 2000; Anderson et al., 1993].

While it is likely that the diffuse seismicity is related to stress relief inside the highly deformed slab, we assume that the larger events more likely represent interplate earthquakes. These can be used to map the location of the interface between the two plates, and thus the thickness of the overlying plate. South of the Fiordland coast the main events lie at a depth of ~10km (events 29,8,4,12 in figure 5.4a). Moving northward, the depth of the larger events increases to ~25km. This pattern of event depths suggests that the Fiordland block is only ~25km thick onshore and that it thins moving southward offshore. Although this is in contrast to the interpretation of crustal thickness recently proposed by Eberhart-Phillips and Reyners [2001], we argue it is consistent with both the pattern of seismicity, geological history, and the gravity pattern. The presence of thin crust in Fiordland is compatible with unroofing during the Cretaceous [Hill, 1995] that has led to the exposure of deep crustal rocks at the surface in Fiordland [e.g. Oliver, 1990]. Additionally, independent of the nature of the support mechanism, the gravity anomaly argues for very high-density material near the surface [e.g. Walcott, 1978], consistent with a thin Fiordland crust.

Offshore to the south, near the Puysegur trench, the larger events (events 29, 8, 4, and d) have depths of ~10 km and the fault planes are sub-horizontal with a slight northward dip. The consistency in both orientation and depth of these events, and the alignment of their slip vectors with the plate motion direction, suggests that the plate interface in this area is at a shallow depth and dips shallowly. West of this cluster of events, there is a very interesting, and we think important, focal mechanism, the Resolution ridge earthquake (event e). The depth and location of the event suggest that it is not associated with the subduction beneath Fiordland. Furthermore, the slip vectors of both nodal planes are highly rotated with respect to the plate motion direction. Furlong et al. [2002] suggested that the event might be related to slip on the tear into the Australian plate. Moving northward the larger earthquakes become progressively deeper ranging from 16km (event 17 close to the shoreline) to ~20 km in the central part of Fiordland (events f and 27). The slip vectors partially rotate [Reyners, 2002] while the slip planes increase in dip both in the northward and eastward direction indicating a twisting of the interplate surface and an increased bend of the slab. The large event on the northernmost part (event g) is also the deepest (60 km) and we interpret it to be an indication of the bending of the nose of the slab. The deep seismicity stops abruptly north of Milford sound. North of that area, the seismicity is dominated by small, shallow events, with mainly strike-slip movement on planes subparallel to the Alpine Fault (e.g. event a) and not related to subduction.

5.3 FLEXURAL MODEL

To test the hypothesis that the sharp bending of the Australian plate beneath Fiordland can support the regional uplift and elevation pattern, we have analyzed the response of a bent elastic plate using a numerical model. We deform the lithosphere to a shape consistent with the geometry inferred from seismicity using the 3-D finite element model code, TECTON [Melosh and Raefski, 1980; Govers, 1993].

The elastic thickness and the forces applied to the plate are parameters that will influence the behavior of the slab and the resulting uplift and gravity. For an oceanic slab, the elastic thickness can be related to its age [e.g. Bodine et al., 1981]. The age of the subducted Australian lithosphere beneath Fiordland is not well constrained and falls in the range of 12 to 35 Ma [Wood et al., 1996; Lamarche et al., 1997; Lebrun et al., 1998; Sutherland et al., 2000]. This corresponds to a range in possible elastic thickness from 12 to 25 km. Here, we focus on the bending of a 13 km thick elastic slab. This was chosen to be consistent with the plate reconstruction of Sutherland et al. [2000], who argues for a relatively young lithosphere subducting beneath Fiordland. If the subducted slab is significantly older (greater elastic thickness) it will tend to deform on a broader wavelength, widening the uplift and pushing it further offshore.

Figure 5.5 shows the geometry and boundary conditions of the model. The elastic slab has a horizontal domain of 700 km by 600 km, with the long dimension in the direction of the plate motion. Although the region of interest in this model is only approximately 300km x 200km, we extend the southern and western extents of the model to minimize artifacts introduced by a no-displacement boundary condition applied along those margins.

Figure 5.5 (Next page): a) extent of the model and boundary conditions. Elastic slab 700x600x13 km bent by lateral pressure applied at the northeastern corner of the model (big arrows). A vertical load applied on the light shaded area of the grid simulates the load of Fiordland. A tear (light dashed line) is added in some models to simulate the decoupling of the subducting sliver from the main Australian plate. **b-f)** Modeling method to compute the topography created by the dynamic support of the bent slab and the load of the Fiordland crust sitting on the subducting plate. Step 1 (b): computation of the bending of the elastic plate due to the lateral pressures ("bent slab"). Step 2 (c): To simulate the loading effect of "Fiordland" necessary for the computation of the gravity signature, we computed the isostatic/elastic flexure equilibrium for a 13 km thick elastic plate under a load sitting on the northeastern corner of the slab. In concert with the observed interplate seismicity and Fiordland extension, the block is 150 km wide and 300 km long with a density of 2800 kg/m^3 and it is assumed to be ~20 km thick in the northern part and taper to 0 southward. The effect of the Fiordland crust is simulated as a load sitting at the northeastern corner of the slab ("loaded slab") using the consistent load method [e.g. Rao, 1992]. Step 3 (d): The total resulting displacement from the applied boundary pressure and the load of "Fiordland" is given as sum of the two previous solutions ("total displacement"). Step 4 (f): The final topography is computed adding the "Fiordland" block over the total displacement solution. In this computation the Fiordland block is displaced vertically with respect to its isostatic equilibrium position wherever the total displacement gives a positive support.

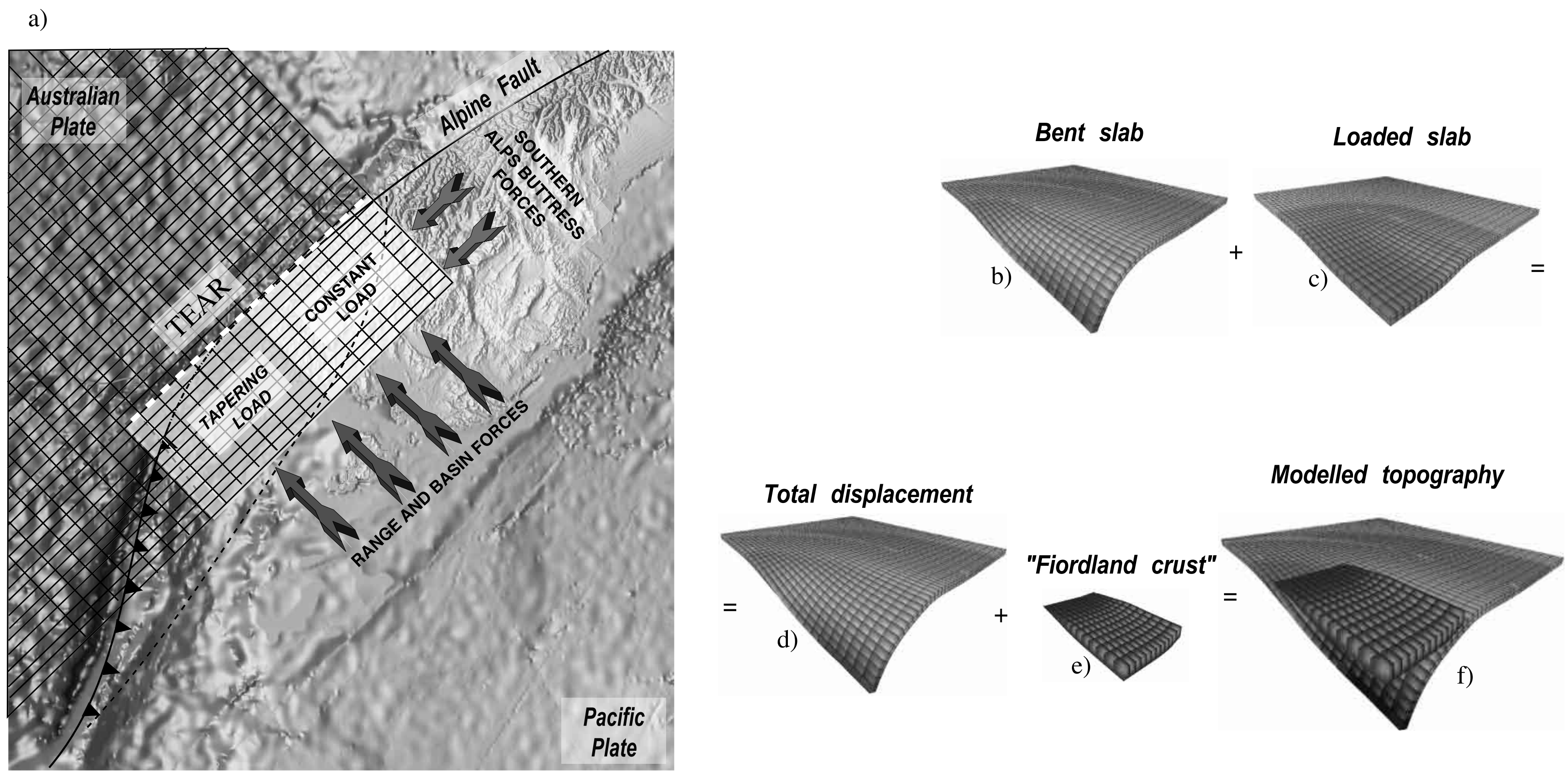
a)
Australian Plate
Alpine Fault
SOUTHERN ALPS BUTTRESS FORCES
TEAR
CONSTANT LOAD
TAPERING LOAD
RANGE AND BASIN FORCES
Pacific Plate
Bent slab
b)
+
Loaded slab
c)
=
Total displacement
d)
+
"Fiordland crust"
e)
=
Modelled topography
f)

We test the consequences of having the Australian plate interact on its north eastern corner with the thickening lithosphere of the Southern Alps to the north and the existing thicker lithosphere of the Otago Range and Basin [Eberhart-Phillips and Reyners, 2001] on the east. Our modeling strategy is to apply boundary pressures along the northern and eastern ends of the model, simulating the effects of this interaction with the root of the Southern Alps and/or the thicker/stronger lithosphere of Western Otago and Southland. This produces a "bent slab" whose geometry is further modified by the effects of the mass of the overlying Fiordland crust, producing the coupled slab geometry and Fiordland uplift (Figure 5.5b). We use a Winkler restoring pressure [Hall-Wallace and Melosh, 1994] applied at the top and bottom surface of the slab to simulate the forces introduced by vertical displacements of density contrasts (isostasy) (e.g. displacement of the surface or the Moho).

Additionally we are interested in the consequences of tears or other decoupling weaknesses internal to the Australian plate. To analyze the role of such a detachment, we add to the elastic slab a tear implemented with the method of the "slippery" nodes [Melosh and Williams, 1989]. Nodes defined as slippery behave as if they have been cut, allowing the two sides to have differential displacement (slip) on the defined surface. Such a fault, 150 km west of the "collision" area, runs southward from the northern end of the slab simulating the proposed propagation of the Alpine Fault into the Australian plate (Figure 5.3) [Lebrun et al., 2000].

5.4 DYNAMIC TOPOGRAPHY RESULTS

We present two suites of model results: (1) a continuous Australian plate subducting beneath New Zealand, and (2) a similar plate geometry to (1) except with the addition of a "tear" simulating the effects of a mechanical decoupling in the plate.

5.4.1 Continuous plate

For the deformed continuous plate, when boundary forces are applied on both the northern (Southern Alps) and eastern (Otago) margin, the resulting uplifted bulge is oriented diagonally with respect to the plate boundary orientation. This is inconsistent with the observed uplift pattern (Figure 5.6 a). To better match the plate boundary parallel observed pattern of uplift, we need to minimize the interaction with the Southern Alps lithospheric root. This would imply that the interaction with the thickening lithosphere of the growing Southern Alps does not significantly influence the subduction beneath Fiordland.

The deformation of the slab resulting from an application of the pressure only on the eastern side of the northeastern corner is similar to the inverted ploughshare model described by Christoffel and Van der Linden [1972] (Figure 6a), but even for a thin (13 km) plate the dynamic uplift (peripheral bulge) generated by the deformation poorly matches the observed topography. The uplift produced by this deformation is quite far away from the collision zone, offshore in the Tasman Sea, a region without high

Figure 5.6: Bent slab dynamic uplift. **a-b)** Peripheral bulge for a continuous elastic slab deformed by pressures applied at the northern and eastern corner. 3-D (a) and map (b) views of the results. The 3-D view in all the figures is observed from the north (as for a hypothetical observer on the Southern Alps). **c-d)** Peripheral bulge for a continuous elastic slab bent from eastern lateral pressures. **e-f)** Peripheral bulge for an elastic slab with a tear decoupling the bent sliver from the main plate. The slab is bent applying both eastern and northern lateral pressures.

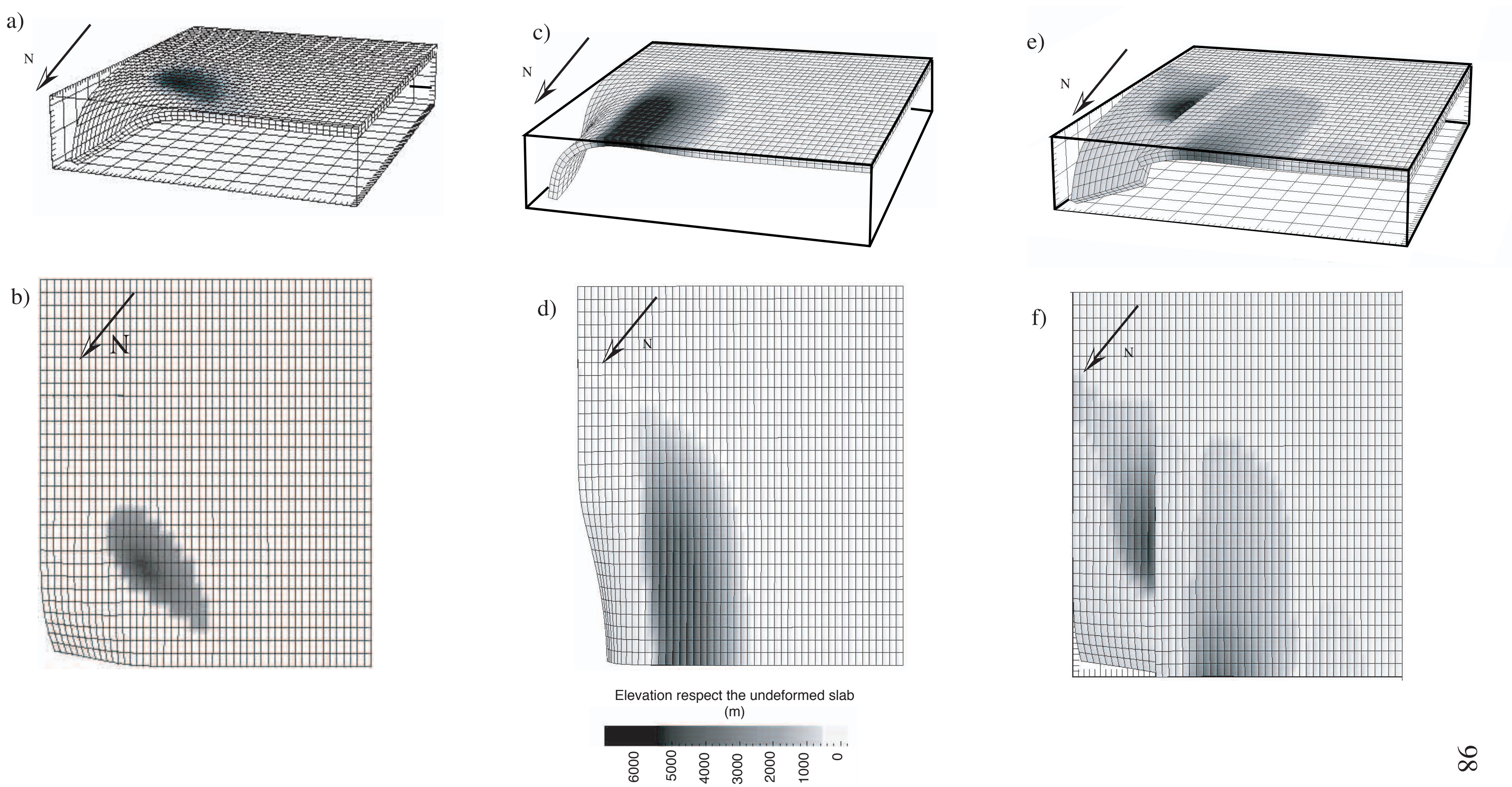

elevations or a significant gravity anomaly. (Figure 5.6b). Additionally, the resulting shape of the slab in the plate motion direction does not match the pattern of observed seismicity (Figure 5.4).

5.4.2 Broken plate

The presence of a tear or weak area mechanically decoupling two sides of the Australian plate significantly changes the lithospheric dynamics of the Fiordland region. Although here we refer to the decoupling as a tear, mechanically the effects are compatible with any localized weak zone cutting the elastic portion of the Australian plate.

The tear decouples the deformation of the sliver of Australian plate east of the tear from the rest of the plate removing the offshore bulge we saw using the models described in the previous section. For this case of a torn plate, an application of bending forces on the east is not sufficient to bend the slab into a geometry that matches the shape of the slab inferred from seismicity. If the only force that bends the slab is a pressure on the eastern side of the sliver of Australian plate, the flexural support increases from south to north reaching the maximum at the northern end. However, the highest gravity anomaly is located in the area of Doubtful Sound, more toward central Fiordland. Incorporating the buttress effect of the lithospheric root of the growing Southern Alps to the north via a pressure on the northern side of the slab in combination with the effects from the applied pressure on the eastern side, improves the correlation of model results with observations. The application of the pressures on the eastern side induces an easterly dip that increases from south to north, while the pressure on the northern side bends the tip of the subducting slab downward increasing the northern dip and reducing the dynamic topography in the northern section. This moves the produced uplift in center coastal Fiordland. With these two pressures applied, the final geometry assumes a shape consistent with seismicity pattern. A sub-horizontal slab is subducting at the Puysegur trench and it is progressively bent moving northward increasing in dip both in the north and east direction to an almost vertical plane below northern Fiordland (Figure 5.4). At the same time, the dynamic uplift generally reproduces the observed pattern of the topography (Figure 5.6 c). Furthermore, the presence of the tear introduces a preferred orientation in the bulge direction that follows the eastern side of the fault/tear in a pattern compatible with topography-bathymetry observations [e.g. Lebrun et al 2000; Cutress et al., 1998; Smith and Sandwell, 1997].

5.5 GRAVITY

A primary motivation for analyzing the role of the Australian plate flexure in producing the uplift of Fiordland was the pattern of gravity and topography. The association of the positive Bouguer gravity anomaly with the high elevations of Fiordland suggests that the region is not in isostatic equilibrium. Our modeling indicates that the flexure of a broken plate can provide the dynamic support to sustain these elevations. This section discusses the resulting gravity signature associated with the computed subduction geometry.

Previous gravity models [Walcott, 1978] suggest that the gravity signature can partially be explained by juxtaposition of oceanic and continental crust at the coast. However, this

Figure 5.7: Fiordland topography utilized for the computation of the gravity field. **a-b)** Modeled topography for a continuous plate bent by eastern lateral pressure and loaded by the Fiordland "crust" (see figure 5.5 f). As in the previous figure the 3-D view is observed from the north. The map views show the combination of the topography due to the bent elastic slab and the supported crust. **c-d**) Modeled topography for a broken plate.

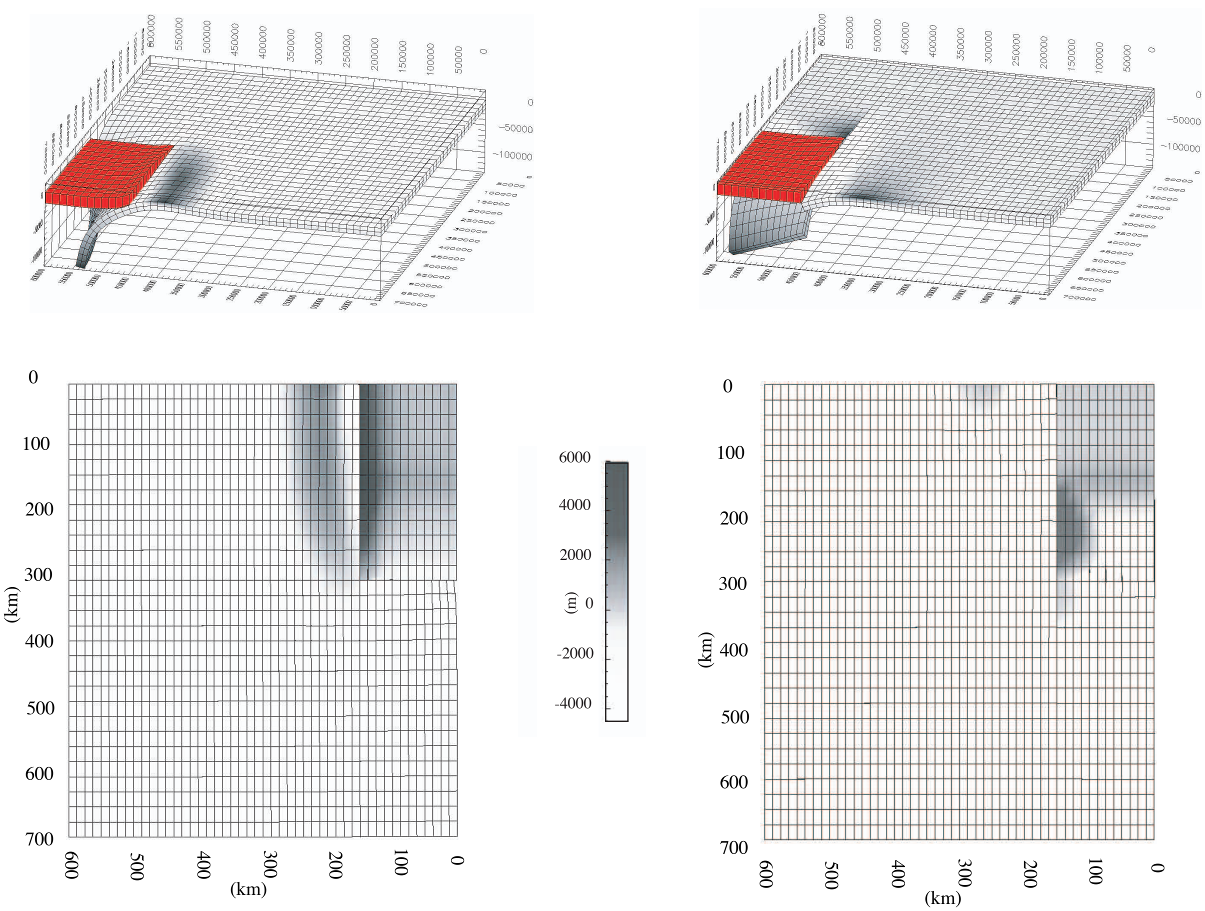

effect by itself can only explain one half of the anomaly observed on Fiordland. Walcott [1978] also suggests that the Fiordland block need to be sharply tilted up to the west and that Fiordland is considerably elevated above its equilibrium position. He proposed that the forces that maintain the Fiordland block out of isostatic equilibrium rise from the internal flexural rigidity of the plate. In contrast, we suggest that the vertical displacement of Fiordland is due to a dynamic support from the bending of the subducting Australian lithosphere. Since the Fiordland block is bounded by major fault systems (Alpine Fault in the west and the Moonlight fault system on the east), we prefer the concept of the dynamic support over lithospheric rigidity. In order to compute the gravity field, we include in our models the effect of the Fiordland block as explained in Figure 5.5. The resulting topography for the case of a continuous and a torn plate, are shown in Figure 5.7.

The plate geometry, the crustal structure, and elevations determined in the 3-D FEM modeling are converted to an equivalent mass distribution for the gravity model. The modeled area (Figure 5.7) is approximated with rectangular prism elements of prescribed density (Figure 5.8). We assume that the top of the model prior to deformation lay 4500 m below sea level (reference model). In order to eliminate edge effects in computing the gravity field, we include the region surrounding the model assuming that it has the same composition of the reference model (4500 m of water over oceanic lithosphere). The gravity signature is computed using the algorithm described by Nagy (1966,1988). To generate the gravity anomalies, we subtract from the result the reference value obtained

Figure 5.8:Model utilized to compute the gravity field for a continuous elastic slab **(a)** and the broken one **(b)**. A density of 3300 kg/m^3 has been assigned to the region delimited by the top of the elastic slab or the bottom of the “Fiordland” crustal block down to 150km. The depth of the elastic slab in the area where it is not deformed is assumed to be 4500m with water filling the vacant space. The Fiordland block is assumed to have a density of 2800kg/m^3.

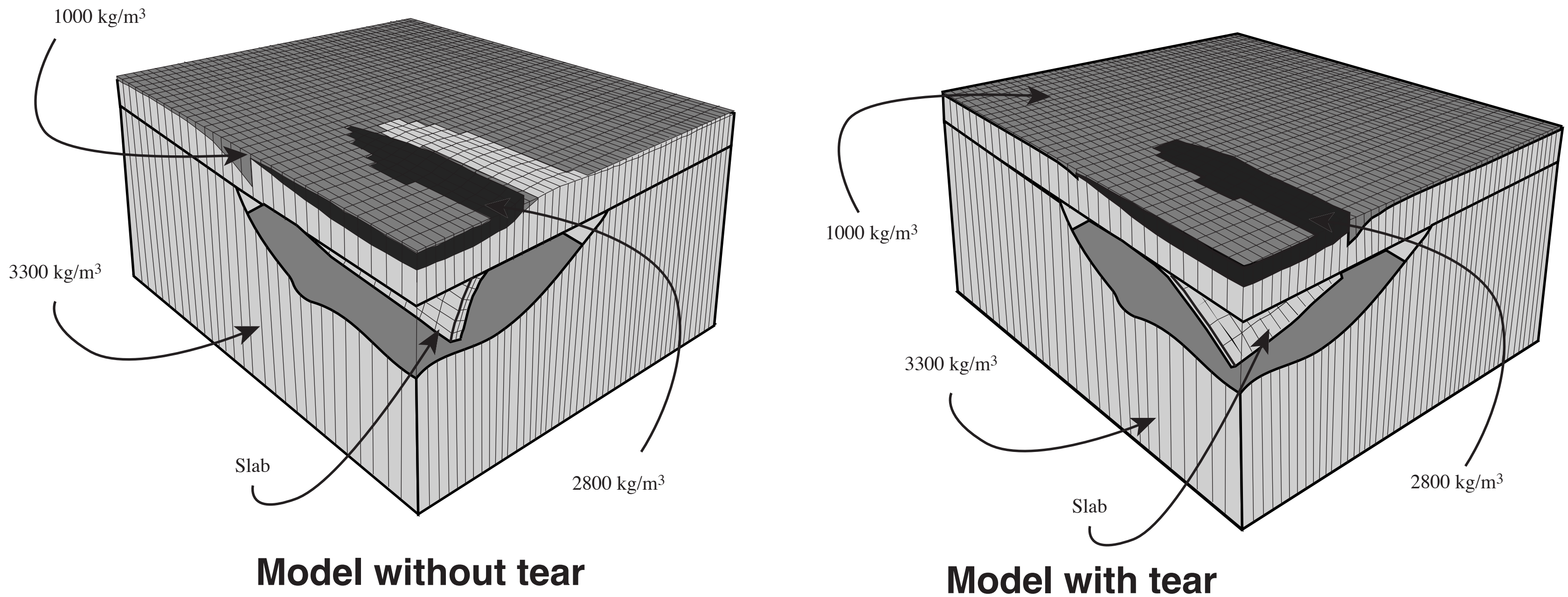

Figure 5.9: Observed and modeled gravity anomalies in Fiordland. a) Map view of the gravity anomalies computed from the model of Figure 5.8 b, broken plate. As in all the map views on this page, the contouring interval is 25 mgal. The positive anomaly close to the boundary in the north and the negative anomaly beneath the letter A' are artifacts of the boundary conditions. b) Comparison of the gravity anomaly computed for a broken plate along the profile AA' of figure a (continuous line) with the anomaly observed along the profile BB' of the map c (dashed line). c) Map of the gravity anomalies observed in the Fiordland region. As in all the plots on this page we report Bouguer anomaly inland and Free Air anomaly offshore. d) Map view of the gravity anomalies computed from the model of Figure 5.8 a, continuous plate. The negative anomaly beneath the letter C' is an artifact of the boundary conditions. E) Comparison of the gravity anomaly computed for a continuous plate along the profile CC' of figure a (continuous line) with the anomaly observed along the profile BB' of the map c (dashed line).

a) MODEL WITH TEAR

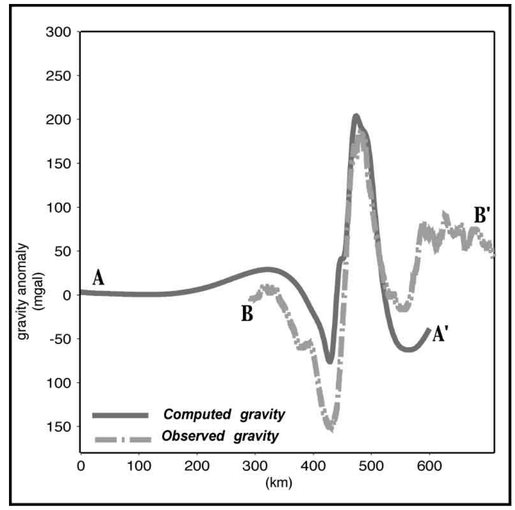

b) MODEL WITH TEAR

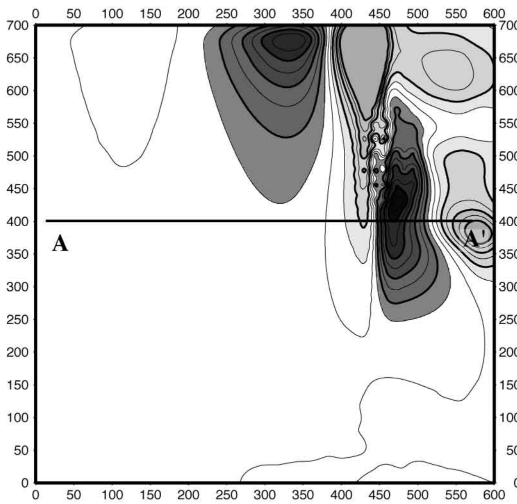

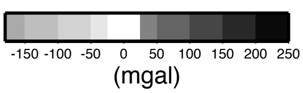

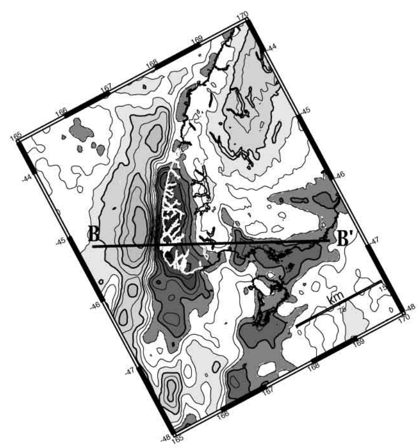

d) MODEL WITHOUT TEAR

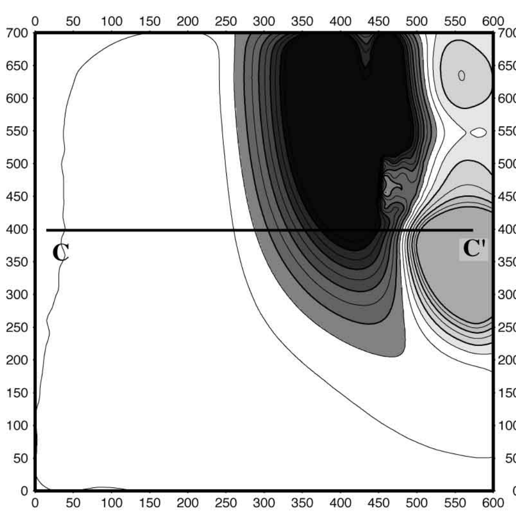

e) MODEL WITHOUT TEAR

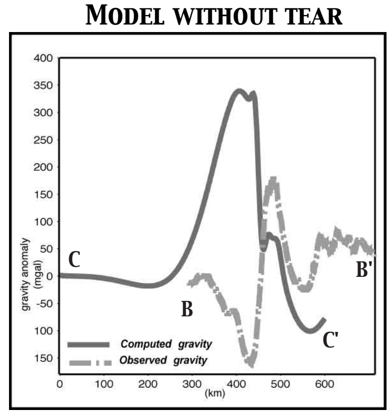

from the gravity signature of an infinite slab with the reference model density structure. We also apply a Bouguer correction to every point above the water level (z=0m).

Figure 5.9 shows the results of the gravity computation for the continuous and the broken plates. The offshore bulge created by bending a continuous plate generates a high positive gravity anomaly that is not present in the observed data (Figure 5.9a). In contrast, the gravity signature for the broken plate model reproduces the wavelength, shape and magnitude of the observed gravity anomaly reasonably well, in particular, for the positive (onshore) side. The model underestimates the negative anomaly. Our model does not include the effects of the ~5 km of sediment in the Fiordland trench [Barnes et al., 1999; Cutress et al., 1998; Hayes and LaBrecque, 1991]. This would increase the downward deflection of the western side of the system increasing the magnitude of the negative anomaly. In both models, the large negative anomaly in the eastern Otago region is simply an artifact of boundary condition effects as well as the positive anomaly offshore in the broken plate model.

5.6 CONCLUSIONS AND DISCUSSIONS

Sharply bending an elastic slab to the shape of the Australian plate subducted beneath Fiordland generates a dynamic uplift. For the model of a continuous slab, the dynamic uplift is localized well offshore in the Tasman Sea an area where neither high bathymetry nor positive gravity anomaly are observed. A tear or a weak zone mechanically decoupling the subducting sliver of the Australian plate from the main plate eliminates the problem of the offshore bulge and confines the dynamic uplift beneath Fiordland. In this case, the dynamic uplift provides the necessary support to keep the Fiordland region in a non-isostatic equilibrium while creating topographic and gravity signatures compatible with the observations. We conclude that a mechanical decoupling of the highly deformed sliver of the slab beneath Fiordland from the main Australian plate is necessary to match the observed data. The nature of this decoupling is still not completely clear. A tear extending the Alpine Fault into the Australian plate as suggested by Lebrun et al [2000] is a viable candidate and would also be compatible with the stress field determined by Reyners et al. [2002]. Nevertheless, the lack of seismicity along such a fault [Reyners et al., 2002] may argue for the decoupling to be a more diffuse weak region. At present, the available observations do not allow us to distinguish between these two models. Recent bathymetric and seismic data acquisitions on the area west of Fiordland (Barnes and Lamarche, pers. comm., 2001) will hopefully allow us to refine the models and improve our understanding of this decoupling.

5.7 REFERENCES

Anderson, H., T. Webb, J. Jackson, Focal Mechanisms of Large Earthquake in South Island of New Zealand: Implications for the Accomodation of Pacific-Australia Plate Motion, *Geophys. J. Int.*, 115, 1032-1054, 1993.

Anderson, H., T. Webb, New Zealand seismicity: patterns revealed by the upgraded National Seismograph Network, *New Zealand Journal of Geology and Geophys.*, 37, 477-493, 1994.

Barnes, P., Davy, B.W., Sutherland, R., Delteil, J., Structure and kinematics of the offshore Fiordland margin, New Zealand, *Geological Society of New Zealand Miscellaneous Publication*s, 107A, 11, 1999.

Bodine, J.H., M. S. Steckler, A. B. Watts, Observation of Flexure and the Rheology of the Oceanic Lithosphere, *Journal of Geophys. Res.*, 86, 3695-3707, 1981.

Bos, A.G., W. Spakman, Tectonic setting of Taiwan inferred from an analysis of GPS data, tomography and seismicity, *Geophysical Research Abstract*, EGS 26th general assembly, Nice, France, 2001.

Calais, E., N. Bethoux, B. Mercier de Lepinay, From trascurrent faulting to frontal subduction: a seismotectonic study of Northern Caribbean plate boundary, *Tectonics*, 11, 98-113, 1992.

Christoffel, D. A., W. J. M. Van der Linden, Macquarie Ridge-New Zealand Alpine Fault transition, in Antarctic Oceanography II: The Australian-New Zealand sector, Antarc. Res. Ser., 19, Ed D.E. Hayes, 235-242, AGU, Washington, 1972.

Cutress, G., R.H. Herzer, R. Wood, J. Delteil, J.F. Lebrun, GEODYNZ Team, Fiordland offshore geology: integrated swath mapping and geophysics, Institute of Geological and Nuclear Sciences, Folio series #3, 1998.

Delteil, J., J.Y. Collot, R. Wood, R., R. Herzer, S. Calmant, D. Christoffel, M. Coffin, J. Ferriere, G. Lamarche, J.F. Lebrun, A. Mauffret, B. Pointoise, M. Popoff, E. Ruellan, M. Sosson, R. Sutherland, From Strike-slip faulting to oblique subduction: a survey of the Alpine Fault-Puysegur Trench transition, New Zealand, Results of Cruise GEODYNZ-sud Leg 2, Marine Geophys. Res., 18, 383-399, 1996.

Eberhart-Phillips, D., M. Reyners, A complex, young subduction zone imaged by three-dimensional seismic velocity, Fiordland, New Zealand, *Geophys. J. Int*, 146, 731-746, 2001.

Furlong, K.P., R. Malservisi, H., Anderson, Initiation (?) of subduction in a complex transpressional regime, Fiordland, New Zealand, *Geophysical Research Abstract*, EGS 27th general assembly, Nice, France, 2002.

Govers, R. Dynamics of lithospheric extension: a modeling study, Ph.D. thesis, Utrecht University, Utrecht, NL, 240 pp, 1993.

Hall-Wallace, M., H. J. Melosh, Buckling of Pervasively Faulted Lithosphere, PAGEOPH, 142, 239-261, 1994.

Hayes, D. E., J. L. LaBrecque, Sediment Isopachs: Circum-Antarctic to 30S, in Marine Geological and Geophysical Atlas of the Circum-Antarctic to 30S, edited by D.E. Hayes, 29-33, AGU, Washington, 1991.

Hill, E.J., A deep crustal shear zone exposed in western Fiordland, New Zealand, *Tectonics*, 14, 1172-1181, 1995.

Lamarche, G., J.Y. Collot, R.A. Wood, M. Sasson, R. Sutherland, J. Delteil, The Oligocene-Miocene Pacific-Australian plate boundary, south of New Zealand, evolution from oceanic spreading to strike-slip faulting, *Eart Plan. Sci. Lett.*, 148, 129-139, 1997.

Lamarche, G., J.F. Lebrun, Transition from strike-slip faulting to oblique subduction: active tectonics at the Puysegur Margin, South New Zealand, *Tectonophysics,* 316, 67-89, 2000.

Lebrun, J.F., G. D. Karner, J.Y. Collot, Fracture zone subduction and reactivation across the Puysegur ridge/trench system, southern New Zealand, *J. Geophys. Res.*, 103, 7293-7313, 1998.

Lebrun, J.F., G. Lamarche, J.Y. Collot, J. Delteil, Abrut strike-slip fault to subduction transition: The Alpine Fault-Puysegur Trench connection, New Zealand, *Tectonic*s, 19, 688-706, 2000.

Melosh, H. J., A. Raefsky, The dynamical origin of subduction zone topography, *Geophys. J. R. Astr. Soc.*, 60, 333-354, 1980.

Melosh, H. J., C. A. Williams, Mechanical of graben formation in crustal rocks: a finite elemement analysis, *Journal of Geophys. Res.*, 94, 13961-19973, 1989.

Millen, D.W., M.W. Hamburger, Seismological evidence for tearing of the Pacific plate at the northern termination of the Tonga subduction zone, *Geology*, 26, 659-662, 1998.

Molnar, P., H. J. Anderson, E. Audoine, D. Eberhart-Phillips, K.R. Gledhill, E. R. Klosko, T. McEvilly, T. V. McEvilly, D. Okaya, M. k. Savage, T. Stern, F. T. Wu, Continuous deformation versus faulting through the continental lithosphere of New Zealand, *Science*, 286, 516-519, 1999.

Moore, M. A., H. J. Anderson, C. Pearson, Seismic and Geodetic Constraints on Plate Boundary Deformation Across the Northern Macquarie Ridge and Southern South Island of New Zealand, *Geophys. J. Int.*, 143, 847-880, 2000.

Nagy, D., The gravitational attraction of a right rectangular prism, *Geophysics*, 31, 362-371, 1966.

Nagy, D., A short program for three-dimensional gravity modeling, *Acta Geod. Geoph. Mont. Hung.*, 23, 449-459, 1988.

Oliver, G.J.H., An exposed coss-section of continental crust, Doubtful Sound, Fiordland, New Zealand; geophysical and geological setting, in: Exposed cross-sections of the continental crust, edited by Salisbury M.H. and D.M. Fountain, 43-69, 1990.

Reilly, W.I., C.M. Whiteford, South Island gravity map of New Zealand, N.Z. Dep. Of Sci. and Ind. Res., Wellington, 1979.

Rao, S.S., The Finite Element Method in Engineering, second edition, p.644, Pergamon Press, 1992.

Reyners, M., R. Robinson, Seismicity, Structure and Tectonics of the Fiordland Region as Revealed by a Microearthquake Survey, personal communication, 1995.

Reyners, M., R. Robinson, A. Pancha, P. McGint, Stress and Strain in a Twisted Subduction Zone, Fiordland, New Zealand, *Geophys. J. Int.*, 148, 637-648, 2002.

Shi, Y., R. G. Allis, New insight to temperature and pressure beneath the central Southern Alps, New Zealand, *New Zealand Journal of Geology and Geophysics*, 38, 585-592, 1995.

Smith, W. H. F., D. T. Sandwell, Global sea floor topography from satellite altimetry and ship depth soundings, *Science*, 277, 1956-1962, 1997, *http://www.ngdc.noaa.gov/mgg/fliers/01mgg04.html.*

Stern, T., P. Molnar, D. Okaya, D. Eberhart-Phillllips, Teleseismic P wave delays and modes of shortening the mantle lithosphere beneath South Island, *New Zealand, Journal Geophys. Res.*, 105, 21615-21631, 2000.

Sutherland, R., The Australian-Pacific boundary and Cenozoic plate motions in the Southwest Pacific: some constraint from GEOSAT data, *Tectonics*, 14, 819-831, 1995.

Sutherland, R., F. Davey, J. Beavan, Plate boundary deformation in South Island, New Zealand, is related to inherited lithospheric structure, *ESPL*, 177, 141-151, 2000.

Sutherland, R., A. Melhuish, Formation and evolution of the Solander Basin, southwestern South Island, New Zealand, controlled by a major fault in continental crust and upper mantle, *Tectonics*, 19, 44-61, 2000.

Walcott, R. I., Fiordland gravity models, in: The Fiordland seismic refraction survey, 1974-5, edited by M. Broadbent and F.J. Davey, Report #124 Geophysics Division, Dept. of Scientific and Indus. Res., Wellington, New Zealand, 1978.

Wood, R., G. Lamarche, R. Herzer, J, Delteil, B. Davy, Paleogene seafloor spreading in the southeast Tasman Sea, *Tectonics*, 15, 966-975, 1996.

APPENDIX A

FEM EARTHQUAKE CYCLE: A COMPARISON WITH AN ANALITYCAL SOLUTION

High precision geodetic measurements such as GPS, provide average movements of the observed monuments during the interval of the observations. To infer a long-term or geological slip rate from such observations, it is necessary to "clean" the data by removing the signal of transient phenomena such as post-earthquake relaxation. For this reason, the geological interpretations of geodetic data are substantially influenced by the dynamic and rheological models utilized in analyzing the data.

An easy and widely applied method to deal with the deformation induced by the earthquake cycle, is to simulate the system by a fault represented by an infinite planar vertical cut in an elastic half-space. During the interseismic period, the fault is locked to a finite depth. Beneath this locking depth, the fault slides continuously at the rate of the relative plate motion (Figure A.1 a)[Savage and Burford, 1973; Okada, 1985,1992]. Over the recurrence time, the slip at depth loads the locked portion of the fault until it reaches the failure point and it slips an amount equal to the accumulated deficit. These analytical models are easy to implement, fit the existing observed geodetic data reasonably well, and produce long-term rates that are comparable with the geological

Figure A.1 Model geometries, rheologies and boundary conditions. Comparison between the boundary conditions, geometries and rheologies for the three different models described in the Appendix. **a)** Cross section for an Elastic half-space dislocation model [Okada, 1985, 1992]. **b)** Cross section for the analytical solution for an elastic layer over viscoelastic half-space [Savage and Lisowki, 1998]. **c)** Cross section of the finite element numerical model [Malservisi et al, 2001].

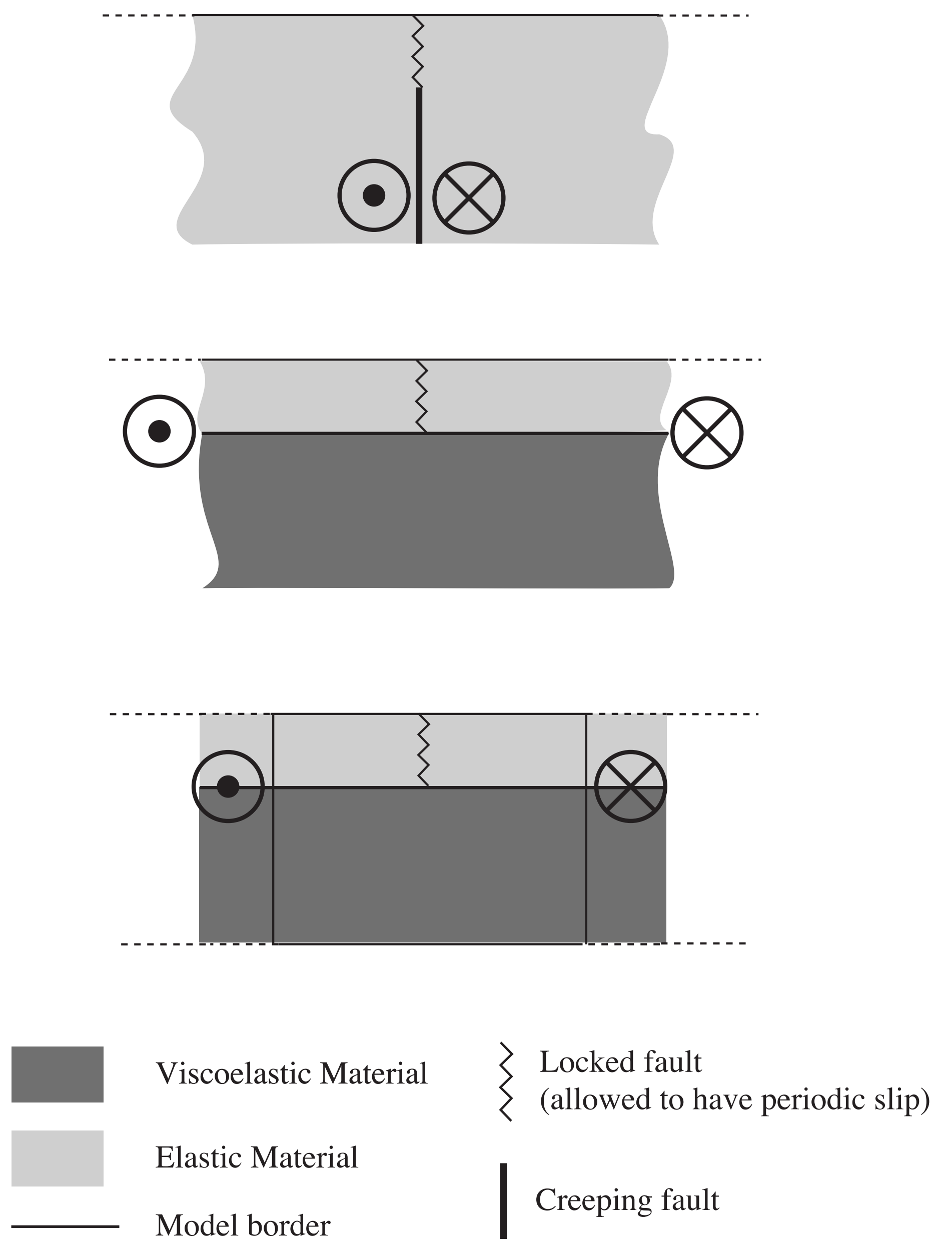

observations. Incidentally, Bürgmann et al. [2000] and Simpson et al. [2001] models used as comparison in chapters 3 and 4, are driven by this kind of elastic dislocation.

In spite of their wide acceptance, the dislocation models present significant problems: the models are not time dependent, the driving forces are localized beneath the fault, and they do not consider that earthquakes rupture only to a finite depth. The limit of the rupture depth of earthquakes as well as rheological and thermal considerations, suggest the existence of a depth where the deformation changes its behavior from brittle (frictional sliding) to ductile (viscous creep). For this reason, a more representative model include,s beneath the seismogenic elastic layer, a viscoelastic layer. The viscoelastic behavior of the lower material introduces a time-dependency into the model, it allows the loading forces beneath the fault to occur in a finite width region, and it incledes the effects of past earthquakes, that can persist long after the last event [e.g. Malservisi et al., 2001; Dixon et al., 2002].

Savage [1990] and Savage and Lisowski [1998] introduced an analytical solution for an elastic layer over a viscoelastic half-space (Figure A.1 b). Here, I compare the results from our numerical simulation of fault deformation including an earthquake (used in chapter 2), with this analytical solution. The Savage and Lisowski [1998] solution involves an elastic layer overlying a viscolelastic half-space and it represents the displacement field from a periodic rupture throughout the entire elastic layer of an infinity-long vertical fault. The displacement is driven by the periodic jump of the locked portion of the fault by the assumption that the long-term slip of the fault is equal to the relative plate velocity at infinity. These boundary conditions are equivalent to a half-space loaded by a far field velocity field applied at infinity.

In this comparison I use the mesh of chapter 2 loaded by velocity boundary conditions applied at the side. Similarly to the Savage and Lisowski model both the elastic and viscoelatic layer are homogeneous. The fault is simulated using the split node method [Melosh and Williams, 1989] that allows differential displacement for specified nodes at specified times. To reproduce the conditions of the analytical model, we define a vertical fault that run through the entire elastic layer oriented parallel to the imposed velocity field. The fault is locked during the interseismic period. The model runs for a time correspondent to the recurrence time of the earthquake cycle (one of the parameters in the analytical model) before the earthquake (fixed slip on the fault). Figure A.2 shows the comparison of the fault-parallel surface velocity field at different time steps predicted by the analytical (black line) and the FEM (gray line and dots) models. The two results are equivalents within typical errors in the geodetic data. For the initial time steps after the earthquake, the FEM solution oscillates slightly around the analytical solution. This oscillation is a consequence of the large deformation induced by the imposed slip and decays with the time. This effect can be reduced by decreasing the time step and/or the mesh size.

Figure A.2: Comparison between the surface velocity field predicted by the numerical model (gray line with circle)[Malservisi et al, 2001] and the analytical solution from Savage and Lisowski [1998] (black line).

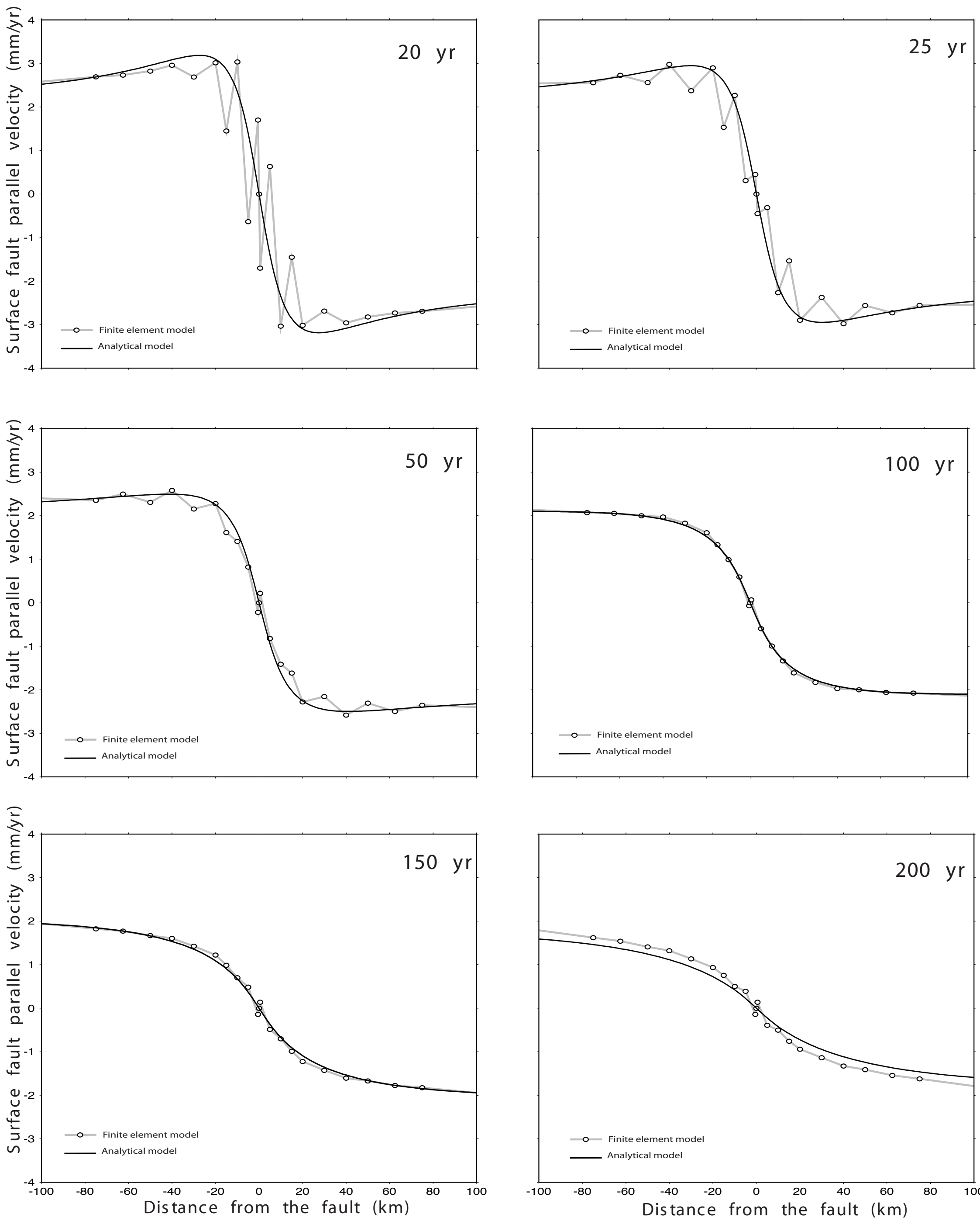

The second difference is at long times, comparable to the recurrence interval. The two models differ in the mechanism that drives the deformations, and this difference is the cause of the divergence of the two models for long times. As stated before, the analytical model imposes a velocity field equal to the relative plate velocity at infinity. This implies that for long times with respect to the recurrence interval, the slope of the “steady state” velocity field at the fault would approach 0. In our model, the boundary conditions are applied at a fixed finite distance from the fault, so the steady state corresponds to a constant simple shear applied to the block. In this way, for long times comparable to the recurrence interval, when the transient effect of the earthquake become negligible, the slope of the steady state approaches a finite value defined by the applied shear. While the two models differ for long times, during the time interval that the transient due to the earthquake is the main signal in the region surrounding the fault, the two models produce virtually the same velocity field. From a tectonics prospective we also think the boundary conditions applied at a finite distance from the fault, better represents the actual conditions at plate boundaries.

The last observation about the width of the shear zone in the viscoelastic layer, has important implication in the analysis of the role that lithospheric plate boundaries play in the observed geodetic data. The classic model of the elastic half-space defines an infinite narrow plate boundary throughout the entire lithosphere. On the contrary, the Savage and Lisowski [1998] model focuses the plate boundary into the elastic lithosphere through the introduction of a fault but implies the absence of a plate boundary in the viscoelastic layer. In the case of an homogeneous viscoelastic layer, the FEM defines the width of the plate boundary by specifying the position where boundary conditions are applied. As seen in chapter 3, the finite element model can introduce a better ways to define the position of the plate boundary, producing strain localization through non-homogeneous or complex rheologies.

A.1 References

Bürgmann, R. Schmidt, D., Nadeau, R.M., d'Alessio, M., Fielding, E., Manaker, D., McEvilly, T.V., and Murray, M.H., Earthquake Potential Along the Northern Hayward Fault, California. *Science,* 289, 1178-1181, 2000.

Dixon, T., J. Decaix, F. Farina, K. Furlong, R. Malservisi, R. Bennett, F. Suarez-Vidal, J. Fletcher, J. Lee, Seismic cycle and rheological effects on estimation of present-day slip rates for the Agua Blanca and San Miguel-Valencitos faults, Northern Baja California, Mexico, *J. Geophys. Res.*, in press.

Malservisi, R., Furlong, K.P., and Dixon, T.H., Influence of the earthquake cycle and lithospheric rheology on the dynamics of the Eastern California shear zone. *Geophys. Res. Lett.,* 28, 2731-2734, 2001.

Okada, Y., Surface deformation due to shear and tensile faults in a half space, *Bull. Seismol. Soc. Am.*, 75, 1135-1154, 1985.

Okada, Y., Internal deformation due to shear and tensile faults in half-space, *Bull. Seismol. Soc. Am.*, 82, 1018-1040, 1992.

Savage, J.C., Equivalent strike-slip earthquake cycles in half-space and lithosphere-asthenosphere Earth models, J. Geophys. Res., 95, 4873-4879, 1990.

Savage, J.C., R.O. Burford, Geodetic determination of relative plate motion in Central California, *J. Geophys. Res.*, 78, 832-845, 1973.

Savage, J.C., M. Lisowski, Viscoelastic coupling model of the San Andreas Fault along the big bend, Southern California, *J. Geophys. Res.*, 103, 7281-7292, 1998.

Simpson, R.W., Lienkaemper, J.J., and Galehouse, J.S., Variations in creep rate along the Hayward Fault, California, interpreted as changes in depth of creep. *Geophys. Res. Lett.,* 28, 2269-2272, 2001.

APPENDIX B

EFFECT OF THE MESH DIMENSION AND BOUNDARY CONDITIONS ON THE CREEPING MODEL

In chapter 3 and 4 I utilize a block 200 km wide, 70 km deep, and 200 km long. The first two dimensions are derived from physical characteristics of the problem we are studying. 200 km is approximately the distance from the stable Sierra Nevada Block to the Farallon Island, considered stable Pacific Plate thus the position where we apply the velocity boundary condition. As stated in chapter 3, these kinds of boundary condition impose the shear strain accommodated by the plate boundary. A narrower or a wider model would imply respectively a higher and lower shear accommodated in the region thus different load on the creeping fault (see also Appendix A). A thickness of 70 km is compatible with that inferred by Zandt and Furlong [1982] who mapped the lithosphere thickness in the San Francisco Bay area using seismic and thermal modeling.

The situation is different at the "northern" and "southern" ends of the model. Here we assume that these surfaces are free to move. In reality, the plates continue beyond this border. To assess the influence of these boundary conditions on the model results I have run different tests changing the overall length of the model while maintaining the length of the creeping zone at 80 km. Figure B.1 shows some results from these tests in the case of the 82 km-long fault free to creep through the entire elastic layer. By definition, the tip

Figure B.1: Models 5a - 5d. Models contain an 82 km fault extending to the bottom of the seismogenic zone (12 km). Model 5a: Creep is only possible on the 82 km fault, extending the entire depth (12 km). For Models 5b - 5d the fault is allowed to creep for the entire model length (200 km) at lower seismogenic zone depths. Model 5b: Creep extends from 4 km to 12 km depth outside the fault. Model 5c: Creep extends from 7 km to 12 km depth outside the fault. Model 5d: Creep zone extent outside the fault decreases from initiating at an upper depth of 4 km to 7 km, extending to the base of the seismogenic zone at 12 km depth. Figure 5e: Surface creeping rate as a function of distance for Models 5a - 5d. Fault properties representation as in Figure 4. Note that the shading scale is different from the one on the other figures.

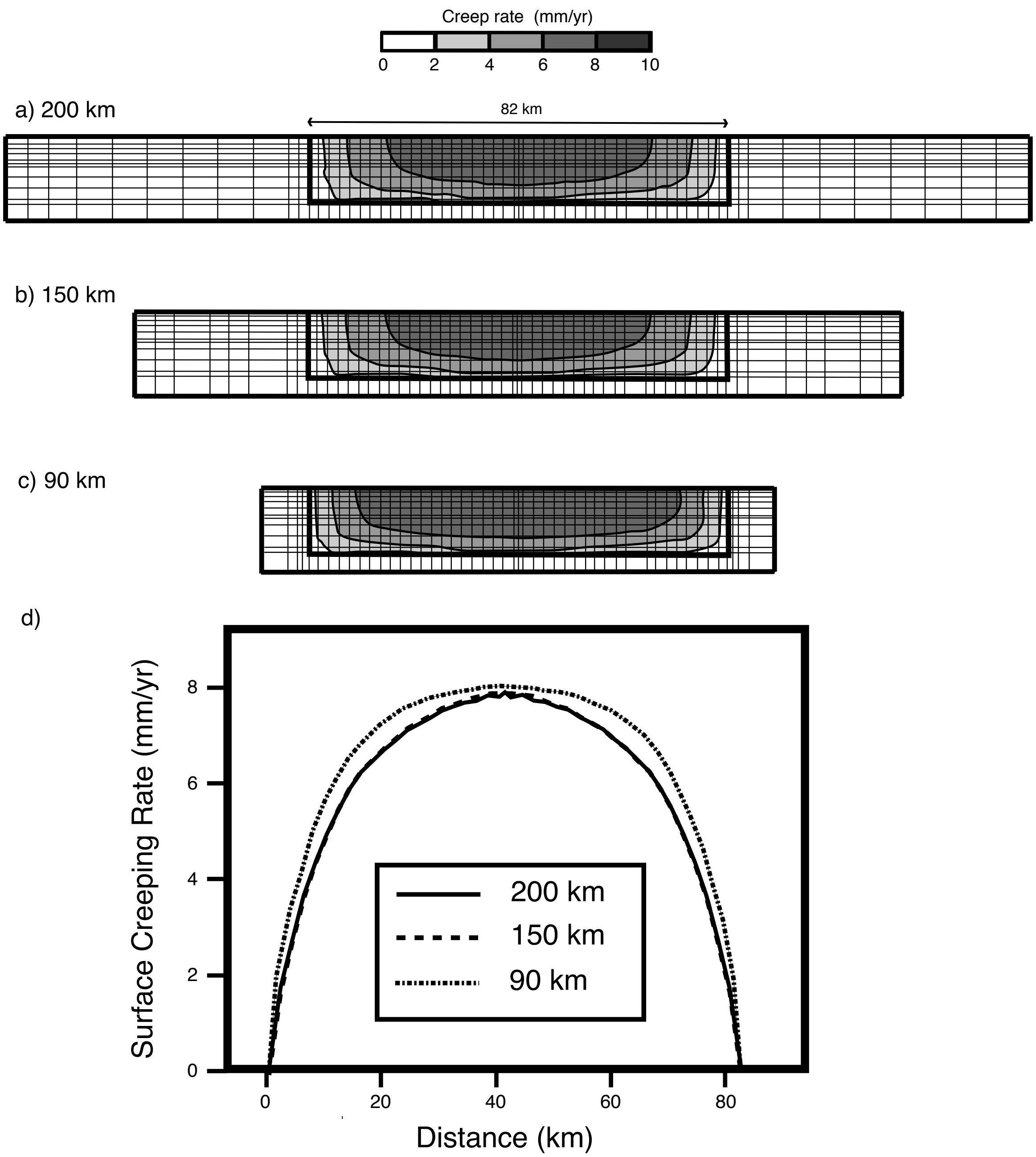

of the fault can not have differential displacement and the creep rate at that point must be zero, thus it can be considered as an area of transition from a creeping to a locked session of the fault. As shown in chapter 3 and 4, at the transition from a locked to a creeping patch the surrounding material is highly strained, leading to a slow creep rate in the surrounding "creepable" regions. If the tip of the fault is close to the model border, however, that strain accumulated at the tip, can be dissipated through the free surface allowing the fault to creep faster. In the case of our models, if there is more than 40 km of model domain beyond the fault tip, the steady state creep on the fault is not influenced by the free surface boundary condition imposed at the northern and southern boundary. In the case of the infinite fault, the absence of the tip and the consequent absence of stress accumulation, is not affected by this boundary condition. Furthermore a model with an infinite fault with similar boundary conditions where the fault is not free to slip but move in periodic seismic events like in Appendix A gives the same result of the analytical solution Savage [1990] and Savage and Lisowski [1998].

B.1 References

Savage, J.C., Equivalent strike-slip earthquake cycles in half-space and lithosphere-asthenosphere Earth models, J. Geophys. Res., 95, 4873-4879, 1990.

Savage, J.C., M. Lisowski, Viscoelastic coupling model of the San Andreas Fault along the big bend, Southern California, *J. Geophys. Res.*, 103, 7281-7292, 1998.

Zandt G., K.P. Furlong, Evolution and thickness of the Lithosphere beneath coastal California, Geology, 10, 376-381, 1982.

VITA ROCCO MALSERVISI

EDUCATION

1996 Laurea in Fisica (Italian degree in Physics) at Università di Bologna, Italy.
Thesis title: Modelli dinamici della Terra per il geoide associato a contrasti di densità interni (Dynamical models of the Earth for the geoid due to internal density contrasts). Grades 110/110.

1997- Ph.D. Candidate at The Pennsylvania State University.

RESEARCH EXPERIENCE

1996-1997 Laureato Frequentatore (Visiting researcher) at Università di Bologna Depart. of Geophysics.

1997- Research Assistant at Penn State University Dept. of Geosciences.

TEACHING EXPERIENCE

Fall 2000 Teaching Assistant at Penn State (fall 2000) GEOS489 Dynamics of the Earth.

Fall 2001 Teaching Assistant at Penn State (fall 2001) GEOS203 Physical Processes in Geology.

Spring 2001 Co-advising Senior Thesis: Christine Gans (Modeling strike-slip faults: numerical study of a transform boundary applied to the Hayward fault, CA and structural study of a rifting margin, Kalya Ridge, Lake Tanganyka, East Africa)

AWARDS

2002 Penn State University Dept. of Geosciences Graduate Student Colloquium, Poster session, 1st place.

2001 Penn State University Dept. of Geosciences Graduate student Colloquium, Oral session, 4th place.

2000 Penn State University Graduate Student Exhibition, 2nd place.

2000 Penn State University Dept. of Geosciences Graduate student Colloquium, Poster Session, 1st place.

PUBLICATIONS

Malservisi R., K.P. Furlong, T. Dixon, , 2001, Dynamics of the Eastern California Shear Zone: influence of the earthquake cycle and lithospheric rheology on the surface velocity field, GRL, 28, 2731-3734.

Furlong, K.P., S.D. Sheaffer, and **R. Malservisi**, 2001, Thermal-Rheological Controls on Deformation within Oceanic Transforms. In . R.E. Holdsworth, R.A. Strachan, J.F. Maglaughlin, and R.J. Knipe (eds), *The Nature and Tectonic Significance of Fault-Zone Weakening*, Geol. Soc., London, Spec. Pub. *186*, 65-83.

Dixon, T., J. Decaix, F. Farina, K.P., Furlong, **R. Malservisi,** R. Bennett, F. Suarez Vidal, J. Fletcher, J. Lee, Present-day slip rate for the Agua Blanca and San Miguel-Vallencitos faults, Northern Baja California, Mexico: influence of rheological model and seismic cycle effects, JGR, in press.

Malservisi R., C. Gans, K.P. Furlong, Numerical modeling of creeping faults and implications for the Hayward fault, California. Submitted to Tectonophysics.

RECENT MEETING PRESENTATIONS (Total 30, most recent first author listed)

Malservisi, R., K.P. Furlong, C. Gans, Creeping faults and seismicity: lessons from the Hayward Fault, California, XXVII EGS General Assembly, Nice (France), 2002.

Malservisi, R., K.P. Furlong, H. Anderson, The role of the Australian plate flexure in Fiordland topography, NSF Workshop on Fiordland, Dunedin (New Zealand), January 2002.

Malservisi, R., K.P. Furlong, C. Gans, Fault Creep on the Hayward Fault, CA: Implications for Fault Properties and Patterns of Moment Release, AGU fall meeting, S.Francisco, CA (USA), December 2001.

Malservisi, R., K.P. Furlong, H. Anderson, R. Govers, The role of the Australian plate flexure on Fiordland, New Zealand, topography, XVI EGS General Assembly, Nice (France) March 2001.

Malservisi, R., K.P. Furlong, T. Dixon, Dynamics of the Eastern California Shear Zone: influence of the earthquake cycle and lithospheric rheology on the surface velocity field, XVI EGS General Assembly, Nice (France) March 2001.

Malservisi, R., K.P. Furlong, T. Dixon, Dynamics of the Eastern California Shear Zone, AGU fall meeting, S.Francisco, CA (USA) December 2000.